Dosimetry at extreme non-charged particle equilibrium conditions using Monte Carlo and specialized dosimeters

by

Eyad Ali Alhakeem

BSc, King Fahd University of Petroleum and Minerals, 2005
MSc, King Fahd University of Petroleum and Minerals, 2007

A dissertation submitted in partial fulfillment of the requirements for the degree of

DOCTOR OF PHILOSOPHY

in the Department of Physics and Astronomy

Dosimetry at extreme non-charged particle equilibrium conditions using Monte Carlo and specialized dosimeters

by

Eyad Ali Alhakeem

BSc, King Fahd University of Petroleum and Minerals, 2005
MSc, King Fahd University of Petroleum and Minerals, 2007

Supervisory Committee

Dr. S. Zavgorodni, Co-supervisor
(Department of Physics and Astronomy)

Dr. A. Jirasek, Co-supervisor
(Department of Physics and Astronomy)

Dr. W. Beckham, Departmental Member
(Department of Physics and Astronomy)

Dr. M. Lefebvre, Departmental Member
(Department of Physics and Astronomy)

Dr. M. Lesperance, Outside Member
(Department of Mathematics and Statistics)

Supervisory committee

Dr. S. Zavgorodni, Co-supervisor
(Department of Physics and Astronomy)

Dr. A. Jirasek, Co-supervisor
(Department of Physics and Astronomy)

Dr. W. Beckham, Departmental Member
(Department of Physics and Astronomy)

Dr. M. Lefebvre, Departmental Member
(Department of Physics and Astronomy)

Dr. M. Lesperance, Outside Member
(Department of Mathematics and Statistics)

ABSTRACT

Radiotherapy is used in clinics to treat cancer with highly energetic ionizing particles. The radiation dose can be measured indirectly by means of radiation detectors or dosimeters. The dose deposited in a detector can be related to dose deposited in a point within the patient. In theory, however, this is only possible under charged particle equilibrium (CPE). The motivation behind the dissertation was driven by the difficult, yet crucial, dosimetry in non-CPE regions. Inaccurate dose assessment performed with standard dosimetry using ionization chambers may significantly impact the outcomes of radiotherapy treatments. Therefore, advanced dosimetry methods tailored specifically to suit non-CPE conditions must be used. This work aims to

improve dosimetry in two types of non-CPE conditions that pose dosimetric challenges: regions near interfaces of tissues with low- and high- density media and in small photon fields.

To achieve the main dissertation objectives, an enhanced film dosimetry protocol with a novel film calibration approach was implemented. This calibration method is based on the percent depth dose (PDD) tables and was shown to be efficient and accurate. As a result, the PDD calibration method was used for the film dosimetry process throughout the dissertation work.

Monte Carlo (MC) calculations for the small field dosimetry were performed using phase-space files (PSFs) provided by Varian for TrueBeam linac. The MC statistical uncertainty in these types of calculations is limited by the number of particles (due to latent variance) in the used PSFs. This study investigated the behaviour of the latent variances (LV) with beam energy, depth in phantom, and calculation resolution (voxel size). LV was evaluated for standard 10x10 cm^2 fields as well as small fields (down to 1.3 mm diameter). The results showed that in order to achieve sub-percent LV in open 10x10 cm^2 field MC simulations a single PSF can be used, whereas for small SRS fields (1.3—10 mm) more PSFs (66—8 PSFs) would have to be summed.

The first study in this dissertation compared the performance of several dosimetric methods in three multi-layer heterogeneous phantoms with water/air, water/lung, and water/steel interfaces irradiated with 6 and 18 MV photon beams. MC calculations were used, along with Acuros XB, anisotropic analytical algorithm (AAA), GafChromic EBT2 film, and MOS*kin* dosimeters. PDDs were calculated and measured in these heterogeneous phantoms. The result of this study showed that Acuros XB, AAA, and MC calculations were within 1% in the regions with CPE. At media interfaces and buildup regions, differences between Acuros XB and MC were in the range of +4.4% to -12.8%. MO*Skin* and EBT2 measurements agreed to MC calculations within ~ 2.5%-4.5%. AAA did not predict the backscatter dose from the high-density heterogeneity. For the third, multilayer lung phantom, 6 MV beam PDDs calculated by all treatment planning system (TPS) algorithms were within 2% of MC. 18 MV PDDs calculated by Acuros XB and AAA differed from MC by up to 3.2 and 6.8%, respectively. MO*Skin* and EBT2 each differed from MC by up to 3%. All dosimetric techniques, except AAA, agreed

within 3% in the regions with particle equilibrium. Differences between the dosimetric techniques were larger for the 18 MV than the 6 MV beam. This study provided a comparative performance evaluation of several advanced dosimeters in heterogeneous phantoms. This combination of experimental and calculation dosimetry techniques was used for the first time to evaluate the dose near these interfaces.

The second study in the dissertation aims to improve dose measurement accuracy in small radiotherapy fields. Field output factors of 6 MV beams from TrueBeam linear accelerator (linac) collimated with 1.27-40 mm diameter cones were calculated and measured using MC and EBT3 films. A set of detector specific correction factors ($k_{Q_{\mathrm{clin}},Q_{\mathrm{msr}}}^{f_{\mathrm{clin}},f_{\mathrm{msr}}}$) for two widely used dosimeters (EFD-3G diode and PTW-60019 microDiamond detectors) were determined based on GafChromic EBT3 film measurements and calculated using MC methods. MC calculations were performed for microDiamond detector in parallel and perpendicular orientations relative to the beam axis. The result of this study showed that the measured *OF*s agreed within 2.4% for fields ≥10 mm. For the cones of 1.27, 2.46, and 3.77 mm diameter maximum differences were 17.9%, 1.8% and 9.0%, respectively. MC calculated *OF* in water agreed with those obtained using EBT3 film within 2.2% for all fields. MC calculated $k_{Q_{\mathrm{clin}},Q_{\mathrm{msr}}}^{f_{\mathrm{clin}},f_{\mathrm{msr}}}$ factors for microDiamond detector in fields ≥10 mm ranged within 0.975-1.020 for perpendicular and parallel orientations. MicroDiamond detector $k_{Q_{\mathrm{clin}},Q_{\mathrm{msr}}}^{f_{\mathrm{clin}},f_{\mathrm{msr}}}$ factors calculated for the 1.27, 2.46 and 3.77 mm fields were 1.974, 1.139 and 0.982 with detector in parallel orientation, and these factors were 1.150, 0.925 and 0.914 in perpendicular orientation. EBT3 and MC obtained $k_{Q_{\mathrm{clin}},Q_{\mathrm{msr}}}^{f_{\mathrm{clin}},f_{\mathrm{msr}}}$ factors agreed within 3.7% for fields of ≥3.77 mm and within 5.9% for smaller cones. This work provided $k_{Q_{\mathrm{clin}},Q_{\mathrm{msr}}}^{f_{\mathrm{clin}},f_{\mathrm{msr}}}$ correction factors for microDiamond and EFD-3G detectors in very small fields of 1.27 – 3.77 mm diameter and demonstrated over and under-response of these detectors in such fields. These correction factors allow improve the accuracy of dose measurements in small photon fields using these detectors.

Contents

List of Tables

List of Figures

LIST OF ACRONYMS

AAA	anisotropic analytical algorithm
AAPM	American Association of Physicists in Medicine
CAX	central axis
CCC	collapsed cone convolution
CDF	cumulative distribution function
CMRP	Centre for Medical Radiation Physics
CPE	charged particle equilibrium
CSDA	continuous slowing down approximation
$\mathbf{d_{max}}$	depth of maximum dose
DTA	distance-to-agreement
ECUT	electron energy cut-off
EGS	electron gamma shower
FFF	flattening filter free
FWHM	full width at half maximum
IAEA	International Atomic Energy Agency
IMRT	intensity modulated radiation therapy
KERMA	kinetic energy released in material
LBTE	linear Boltzmann transport equation
linac	linear accelerator
LV	latent variance
MC	Monte Carlo

MOSFET	Metal Oxide Silicon Field Effect Transistor
NIST	National Institute of Standards and Technology
nOD	net optical density
non-CPE	non-charged particle equilibrium
NTCP	normal tissue complication probability
OD	optical density
OF	output factor
PCUT	photon energy cut-off
PDF	probability density function
PSF	phase-space file
PSF_A	Varian phase-space file
PSF_B	phase-space file scored under secondary collimator
PSF_C	phase-space file scored under stereotactic collimator
PDD	percent depth dose
PRESTA	parameter reduced electron step algorithm
PV	pixel value
RNG	random number generator
SRS	stereotactic radiosurgery
SSD	source to surface distance
TCP	Tumor control probability

TPS	treatment planning system
VIC	Vancouver Island Centre
VIMC	Vancouver Island Monte Carlo
VMAT	volumetric modulated arc therapy
VRT	variance reduction technique

Acknowledgements

To my supervisor, Dr. Sergei Zavgorodni, thank you for your guidance, help, and support during the work of my dissertation. I consider myself very fortunate to be supervised by such a wise, and knowledgeable mentor. Thank you for your patience with me and for always managing your busy schedule to meet and answer my questions, even outside of working hours! I learned a lot from you. I am deeply grateful to you!

To my co-supervisor, Dr. Andrew Jirasek, Thank you for your assistance and constant monitoring of my progress. I am grateful for the time and feedback you provided when writing this dissertation.

Also, I would like to extend my thanks to my supervisory committee, Dr. Wayne Beckham, Dr. Mary Lesperance and Dr. Michel Lefebvre for being part of my supervisory committee and taking the effort and time to meet and monitor my progress. Thank you for all of your help and the constructive critiques and feedback you provided during my work. I am particularly thankful to Dr. Wayne Beckham for his role in facilitating my work in the BC cancer agency.

I am particularly grateful to Dr. Magdalena Bazalova-Carter for her support, valuable time and help while writing the dissertation.

I would also like to thank Mr. Stephen Gray for precision manufacturing of the small collimators used in my work. I am indebted to the physicists in the BC Cancer agency and fellow graduate students for their constructive feedback during my work. I extend my thanks to my friend Mohammad Alkhamis for providing his computational cluster and related technical support to perform some of the Monte Carlo calculations done in my study.

I would like to thank Dr. Anatoly Rosenfeld for providing the MO*Skin* detectors and for the valuable discussion and feedback during the joint project with Wollongong University. I extend my gratitude and thanks to Dr. Sami Alshaikh for providing his expertise and help in the measurements performed with the MO*skin* detector.

To my parents, thank you for raising and teaching me to become the person I am today. My mother, thank you for the infinite love, prayers and endless emotional support. To my brothers and sisters, thank you for the support and encouragement.

To the source of my happiness and the greatest blessing in my life: Hawra, Kawther, Fatima, Narjes, Sokaina, and Ameer. Thank you, my little angels, for filling my life with love and joy. You are my life!

To my wife, Zainab, words can’t describe my gratitude and true feelings towards you! Thank you for your patience, unconditional love, endless support and for being the shining light in the darkest moments during all these years. You were and, I know, you will always be there for me when I rejoice and when I weep. Without you, all of this wouldn’t be possible. I owe you everything!

Finally, I would like to thank the Ministry of Higher Education in Saudi Arabia for providing the generous support and funds to complete my degree.

Chapter 1

Introduction

This dissertation evaluates radiation dose in complex conditions. In this chapter, the concept of radiation dosimetry and the methods of measurement and calculation techniques will be introduced. Section 1.2 introduces dosimetry in external radiotherapy photon fields. Two complex scenarios where dosimetry is difficult to evaluate are summarized in section 1.2. Section 1.3 and 1.4 present the different dosimetric techniques used in the dissertation. Finally, section 1.5 presents the scope of this dissertation and summarizes the contents of each chapter.

1.1. Dosimetry in external radiotherapy photon beams

Radiotherapy is often used in clinics to treat tumors via highly energetic ionizing particles that damage the tumor cells. In any radiotherapy treatment both normal and cancerous cells are affected when exposed to radiation; however, cancerous cells are affected more due to their high proliferation rate. The objective of any radiotherapy treatment is to maximize the dose delivered to the tumor while minimizing it to the patient's normal tissue. The outcome of a radiotherapy treatment is evaluated in terms of two radiobiological parameters: tumor control probability (TCP) and normal tissue complication probability (NTCP). Figure 1.1 shows TCP and NTCP as a function of dose. There is a very narrow window where the right amount of dose must be delivered for a treatment plan to be successful. That is, maximizing TCP in order to kill tumor cells while minimizing NTCP to spare normal tissue cells. In order to achieve the best treatment outcomes, the prescribed radiation dose must be accurately delivered to the tumor. Therefore, in such treatments, it is very important to accurately evaluate and deliver the right radiation dose . (Chang, Lasley, Das, Mendonca, & Dynlacht, 2014; Khan, 2003)

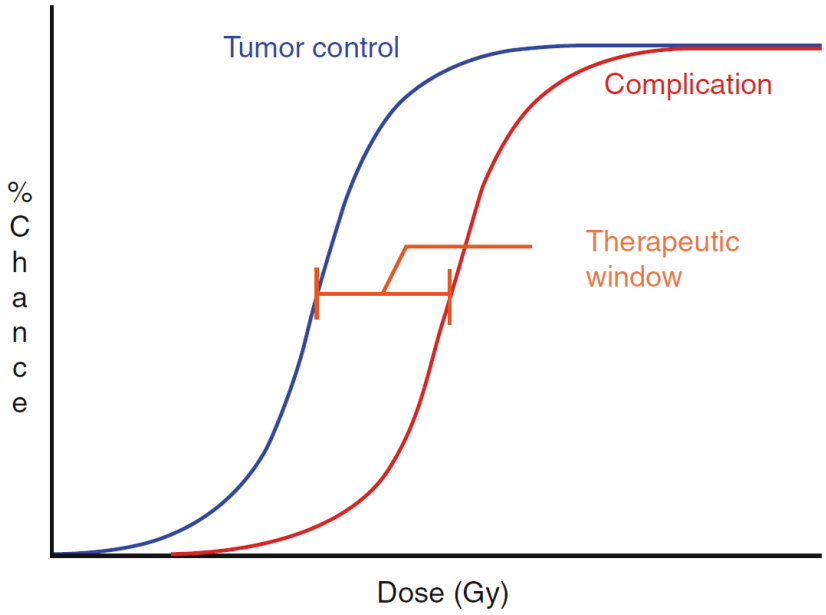

Figure 1.1:The tumor control probability (TCP) and normal tissue complication probability (NTCP) are plotted as a function of dose. The plot shows the therapeutic treatment window. (Chang et al., 2014)

The quantification of radiation dose is crucial in such treatments and hence ought to be prescribed and delivered accurately to the targeted volume in order to achieve the expected treatment outcomes. Dosimetry is the determination of the amount of energy resulting from the interaction of ionizing radiation that is deposited in matter. The dose can be measured indirectly by means of radiation detectors or dosimeters. The dose deposited in a detector's sensitive volume can then be converted to a dose deposited in point within the body. The next section introduces the physics of radiation interaction within matter in order to clarify the concept of dosimetry.

1.1.1. Photon radiation physics

Megavoltage photon beams (1-20 MeV) are typically used in external photon radiotherapy treatments. High energy photons interact with matter via four major interaction processes: coherent scattering, photoelectric effect, Compton scattering and pair production. Secondary electrons are produced by these interactions, except the coherent scattering, and deposit their energy into the medium. The interaction probabilities, also known as cross sections, of these processes vary depending on the photon energy and the material type. Photon cross sections are important parameter in the dose calculation concept.

Coherent Scattering

Coherent scattering, also known as Rayleigh scattering, dominates in low energy domains (<10 keV) and in high-Z materials. In this process, a low energy photon releases all its energy to excite and de-excite an atomic electron, releasing a scatter photon that has the same energy as the incident photon.

Photoelectric effect

When the energy of an incident photon is large enough to break an electron's atomic binding energy, this electron is knocked out and absorbs the rest of the photon's remaining energy as kinetic energy. Unlike coherent scattering, photo electric interaction ionizes the media it passes through. Photoelectric effect dominates in high-Z media and at low energies (below 1 MeV).

Compton scattering

A photon interacts with an atomic electron and transfers part of its energy to the atomic electron as kinetic energy. The photon along with its remaining energy is then scattered at an angle. The knocked-out electron continues to interact with the media and transfers the gained energy through ionization and excitation. The probability of Compton scattering is proportional to the electron density of the material and is almost independent of the medium atomic number Z. It dominates at low to moderate photon energy domain (Chang et al., 2014)

Pair production

A photon with an energy >1.02 MeV might interact with matter through a pair production process. The incident photon interacts with the Columb field of an atomic nucleus to produce an electron-positron pair, each with a rest mass energy of 0.511 MeV. The electron-positron pair is scattered in a forward direction relative to the incident photon, sharing the rest of the incident photons energy (incident photon energy-1.02 MeV). The electron and positron continue their interactions until they fully deposit their energy in the medium. Pair production interactions increase rapidly with energy.

All of the above types of interaction take place in a patient body treated with therapeutic photon beams. Each of these interaction process contributes to the total energy transferred to the patient. The mass energy-transfer coefficient $\frac{\mu_{tr}}{\rho}$ is a useful parameter to evaluate the amount of energy transferred by photons into a medium. The mass energy-transfer coefficient takes into consideration the contribution of each of the above interaction processes. Mass energy transfer coefficients are used to calculate the amount of energy released by photons into a medium. The mass-energy coefficient tables are provided by the National Institute of Standards and Technology (NIST) for several materials and compounds (Suplee, 2009).

1.1.2. Dosimetry

When photons propagate in a medium, part of their energy is transferred to the medium as a result of the interaction processes described earlier. Photons transfer energy to the medium indirectly by ionization and excitation processes. Part of the energy is transferred as kinetic energy to charged particles within the medium. The charged particles transport further in the medium while releasing their kinetic energy. The energy released by the charged particles is known as KERMA, Kinetic Energy Released per unit Mass. Mathematically, KERMA is defined as

$$KERMA = \frac{dE_{tr}}{dm} \qquad (1.1)$$

Where dE_{tr} is the total kinetic energies of all initial charged particles set in motion by photons in mass (m) of a the medium. The liberated charged particles in turn release their energy into the medium through collisions and defined as collision KERMA (K_C). The other part of this transferred kinetic energy is carried away or lost in the form of radiative losses and hence doesn't contribute to the dose and this is known as the radiative KERMA (K_R). Mathematically, total KERMA can be written as

$$K_{tot} = K_R + K_C \qquad (1.2)$$

The absorbed dose is defined as the mean energy ($d\bar{E}$) per unit mass imparted to the media by these charged particles. Mathematically, the absorbed dose can be written as

$$Dose = \frac{d\bar{E}}{dm} \qquad (1.3)$$

The derived SI unit for radiation absorbed dose is gray (Gy), where 1 Gy is equal to 1 joule of energy per kilogram of matter.

When the number of charged particles leaving a volume of interest are replaced by an equal number of charged particles of the same type and energy, Charge Particle Equilibrium (CPE) is said to exist. Under this condition K_C can be related to the dose since most of the damage is caused by the liberated charged particles at a point of interest with infinitesimal volume where radiation loss is carried out (K_R).

The CPE condition is important in order to relate the absorbed dose to a measurable quantity, K_C. In a medium irradiated by high energy photon beams, CPE only occurs beyond the dose build-up region. This region has a dimension similar to the maximum range of the liberated charged particles in the medium. When the photon attenuations in the medium is considered, the equilibrium condition is called Transient Charge Particle Equilibrium (TCPE). Under TCPE conditions, the collision KERMA (K_C) is proportional to the deposited dose beyond the build-up region. Figure 1.2 shows the relationship between K_C and the deposited dose as a function of depth in a medium irradiated with a high energy photon beam.

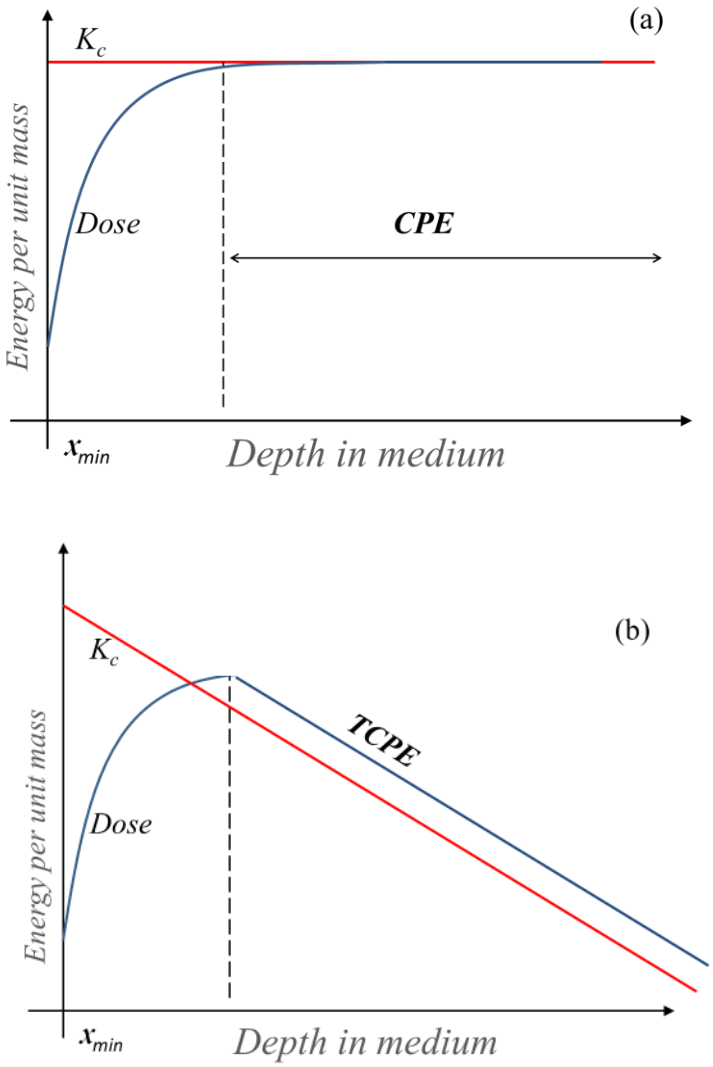

Figure 1.2: Diagram illustrating the relationship between collision KERMA (K_C) and the absorbed dose as a function of depth in a medium irradiated by a high energy photon beam: (a) with no photon attenuation (hypothetical). (b) With photon attenuation

Failure of CPE or TCPE conditions, can lead to inaccuracy of dose measurements at a point of interest in the medium. Attix (1976), in his book, explained some practical situations where CPE conditions fail to exist. One situation is when volume of interest is within radiation source proximity a. In this case, CPE condition fails since the number of secondary charged particles entering the volume from the side closest to the source is larger than the number of that leaving the volume.

CPE also fails to exist near/at boundaries of inhomogeneities within the medium due to the change in medium density that causes a difference in secondary electrons entering and leaving a dosimeter volume. The difference is due to the change in the charged particles productions, range or geometry of their scattering for the different media.

CPE condition also fails when the radiation field size is comparable to the lateral electrons path lengths within the irradiated volume of interest. Therefore, the lateral CPE condition doesn't occur across the volume. Figure 1.3, shows a diagram illustrating the three non-CPE situations introduced above.

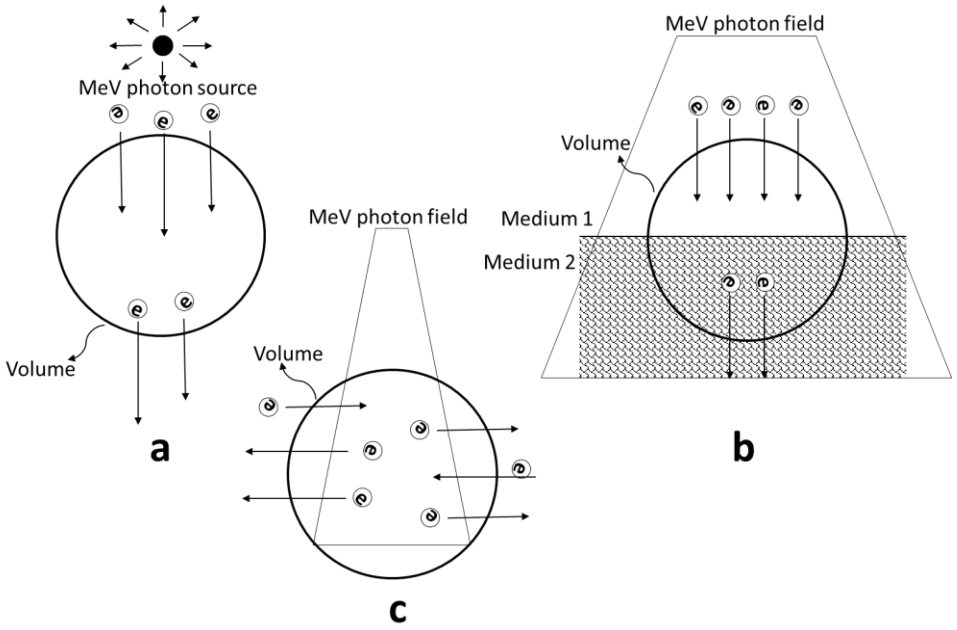

Figure 1.3: Diagram illustrate three situations where charged particle equilibrium (CPE) does not exist. (a) The volume is too close to the radiation source, (b) the volume is within a proximity of a boundary of inhomogeneities and (c) the volume is irradiated with a narrow radiation beam.

Accurate dosimetry in these situations requires specialized dosimetric approaches and techniques. In this work, two of the above non-CPE situations will be investigated. Dosimetry within proximity of inhomogeneity and in small radiation fields will be presented in Chapters 4 and 6.

1.2. Practical non-CPE regions in external radiotherapy

1.2.1. Dosimetry near heterogeneities in radiotherapy

The human body is a heterogeneous medium composed of tissues with different densities. Sometimes treated regions consist of high-density implants such as a hip prosthesis. The dose distribution near heterogeneities is difficult to evaluate accurately due to the lack of CPE condition. Also, the dose gradient near extreme density heterogeneities is steep and therefore requires dosimeters with a very thin detection area. Inaccurate dose assessment in these areas, may result in over or underestimation of the dose delivered to the target and/or the surrounding organs.

1.2.2. Dosimetry in small fields used in radiotherapy

Small photon beams are often used in modern radiotherapy treatments to cure brain tumors, lesions, and functional disorders. These types of treatments need accurate dosimetry which is difficult for field sizes used in these treatments.

Das et al (2008), summarized challenges associated with small field dosimetry. These include lack of lateral charge equilibrium (LCPE), source occlusions, and detector perturbations.

Even though TCPE could exist along the beam axis for high energy photon beams of sizes smaller than the dose detection volume, there is a loss of the charged particle equilibrium from the lateral side of the beam axis as illustrated in Figure 1.3-c

The primary photon source could be partially occluded by the collimation device used to produce the small photon fields. This will lead to an underestimated dose measurement by a detector on the beam axis.

There are two definitions of the field size in external radiotherapy. The geometric field and the dosimetric field size. The geometric field size is the geometrical projection by the source of the collimation device opening on plan perpendicular to the beam axis. Whereas, the dosimetric field size is defined by the dimension of the dose area on a plan perpendicular to the beam axis. More accurately, the dosimetric field size is defined by the lateral profile Full Width at Half Maximum (FWHM). For broad beams, geometric fields and dosimetric fields are considered equal for all practical purposes.

However, for small beams, the geometric and the dosimetric fields are not always equal. This is because the dose on the central axis (maximum dose) is reduced due to the partial occlusion of the primary source. Hence the determined FWHM of the lateral dose profile is now broader due to the reduction of the maximum dose (Palmans, Andreo, Christaki, Huq, & Seuntjens, 2017). The IAEA-AAPM TRS-483 report recommends the use of dosimetric field size to report dosimetric quantities related to small radiotherapy beams (Palmans et al., 2017). It

has been shown that the use of the dosimetric field size is a more accurate approach and removes the ambiguity in reporting and interpreting small field dosimetric data (Gavin Cranmer-Sargison, Charles, Trapp, & Thwaites, 2013).

There are also detector related conditions that could impact the dosimetry in small fields. Some of these conditions are the detector volume averaging effect and the perturbation of the particle fluence caused by its non-water equivalency. Therefore, a detector shape, size, orientation, and the material of its sensitive volume and housing are important factors to consider when performing dosimetry in small photon fields.

The IAEA-AAPM TRS-483 (Palmans et al., 2017) provided guidelines on small field dosimetry. This report defines small fields, provides recommendations on suitable detectors and good working practice for dosimetry in such conditions.

1.3. An overview on advanced surface and small beam dosimeters

Various dosimeters are available on the market, designed to serve particular measurement purposes. These dosimeters have their pros and cons depending on the measurement situation. Therefore, it is important to use a suitable dosimeter for dosimetry at non-CPE conditions and one should be careful about selecting the right dosimeter.

The objective of this dissertation is to evaluate the dose at extreme non-CPE conditions: build-up region, boundaries of heterogeneities and in small photon fields. For the scope of this work, we have selected the dosimeters based on their suitability to the investigated situation. GafChromic EBT2/3 films and MOSFET are good candidates for surface and build up measurements. As mentioned earlier, GafChromic EBT films produce very accurate results when used carefully. For that, extensive effort was made to follow a sophisticated film dosimetry protocol that will be described in Chapter 3.

In the part of this work devoted to small field dosimetry, we used a solid state EFD-3G diode and the PTW-60019 microDiamond detectors as they were specifically designed for this type of use. An overview on advanced surface and small field dosimeters is presented in the following sections.

1.3.1. Radiochromic films

Unlike radiographic films, radiochromic films do not need any chemical processing and they can be handled in room light. When exposed to radiation, radiochromic films are colored in proportion to the amount of dose deposited in their sensitive layers.

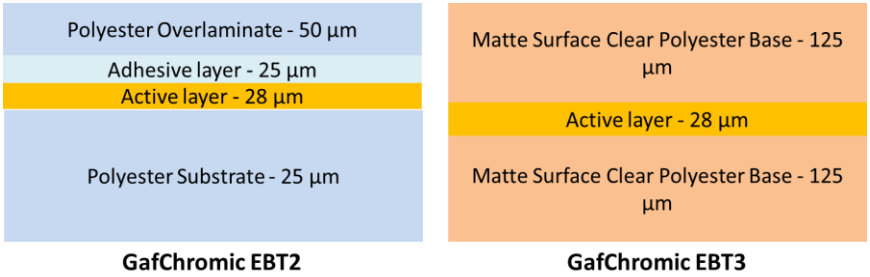

Figure 1.4: A diagram illustrating the structure of the GAFCHROMIC® EBT2 and EBT3 radiochromic films (David Lewis, ISP Technology).

ISP technology developed a new version of radiochromic film called GafChromic EBT3 films (Ashland, Specialty Ingredients, NJ). Both versions are quite similar, except that in EBT3 the structure is symmetric which makes the scanning outcomes of either side to be identical. Otherwise, they both have the same active component and atomic composition. Figure 1.5, shows the structure of both EBT2 and EBT3 film.

GafChromic films have a wide dynamic range of dose (1 cGy-40 Gy) and are near-tissue equivalent. Films are 2D spatial detectors that offer a high spatial resolution with very minimal perturbation. This makes them near perfect dosimeters for small fields and regions of steep dose gradient, such as boundaries of heterogeneities.

1.3.2. MOSFET (MOSkin™) detectors

Metal Oxide Silicon Field Effect Transistor (MOSFET) detector is a semiconductor-based real-time dosimeter. MOSFET detectors are well suited for surface and skin dosimetry due to their very thin detection volume.(Butson et al., 1996) Special design of MOSFET detector known as "MOSkin™" for its dosimetry capabilities at skin surface and interfaces was developed at the Centre for Medical Radiation Physics (CMRP), University of Wollongong (Ian S. Kwan, 2009), Australia and used in this study. MOSkins detectors offer water equivalent effective depth of measurement (WED) of 0.02 or 0.07 mm depending on type. MOSkin chip is embedded into the 0.4 mm thick KAPTON pigtail with a width of 3 mm and length about 35 cm that allow electrical connections to a small 0.6 x 0.8 x 0.35 mm^3 silicon chip and packaging simultaneously with reproducible WED of measurements without using epoxy bubble that make it useful for placement into interfaces or confined spaces in a phantom.

1.3.3. EFD-3G diode detector

EFD-3G diode detector is a silicon-based detector. The silicon chip is embedded in an epoxy-cylindrical housing. The silicon active volume consists of N-doped (electron rich region) side, P-doped side (electron holes rich region) and depletion zone sandwiched between these two layers. In principle, the chip acts as a parallel plate chamber in which the depletion zone mimics the air cavity of an ion chamber. An ionization occurs in this region create electron-hole pairs that generates a current across the p- and n-doped sides. The generated current is proportional to the amount of ionization caused by the incident radiation.

Diode detectors are extremely sensitive due to the high density of its silicon active volume chip. The silicon density (2.3 g/cm^3) is 1800 times denser than that of air and the current produced per unit volume is 18,000 times larger than that produced in ion chamber. Therefore, diode detectors can be manufactured in very small and thin volumes to provide higher dose detection resolution in small radiation beams. This type of dosimeters, however, are energy dependent in photon beams (Chang et al., 2014). For accurate dosimetry, diode detector readings must be corrected for energy dependence (Paolo Francescon, Cora, & Cavedon, 2008; Ralston, Liu, Warrener, McKenzie, & Suchowerska, 2012).

1.3.4. Diamond detector

Diamond material has been long investigated for its application in radiotherapy dosimetry due to its attractive physical properties. Diamond is a nearly tissue equivalent material with an atomic number (Z=6) close to that of water (Z~7.42). It has high radiation detection sensitivity and thus can be constructed in very small sizes to provide higher dose detection resolution in narrow beams.

In principle, diamond detectors work as a solid-state detector. Radiation creates electron-hole pairs within the diamond crystal that are proportional to the amount of radiation. The PTW Riga diamond detector is one of commercially manufactured natural diamond-based detector (ref). PTW Riga diamond detector was investigated intensively (Heydarian, Hoban, Beckham, Borchardt, & Beddoe, 1993; Hoban, Heydarian, Beckham, & Beddoe, 1994) for their use in radiotherapy. There are some limitations that make natural diamond undesirable as investigations showed. Detector-grade quality natural diamonds are rare and expensive. They also suffer from quality degradation with time that affects their measurements stability and reproducibility. The natural diamond detector was shown to demonstrate dose rate dependence that needs to be corrected for. (Almaviva et al., 2008)

Synthetic single crystal diamond detector (SCDD), on the other hand, was shown to be a better alternative to the natural diamond. Better control of the diamond crystal growth and its impurities during the synthesizing process as well as the standardized detector assembling

improved the manufacturing reproducibility and their dosimetric response quality. (Almaviva et al., 2008; Ciancaglioni et al., 2012; Marsolat et al., 2013)

Most recently PTW (PTW-Freiberg, Germany) released a commercial version of a SCDD called microDiamond detector (PTW-60019). In line with the previous studies on prototypes of the SCCD, microDiamond detector proved to be suitable for photon small beam dosimetry (Laub & Crilly, 2014). The PTW-60019 detector consists of a radiation disk-shaped sensitive volume made of synthetic single crystal diamond. The disk has a diameter of 2.2 mm and a 1µm thickness (an active volume of 0.004 mm^3)

1.4. Dose calculation algorithms

Dose calculation algorithms implemented in treatment planning systems are used to calculate the dose to be delivered to a patent. Accurate dose calculation is imperative to deliver the most tailored and accurate treatment for each patent considering all dose constraints.

Clinical dose calculation algorithms are built to be fast to keep up with the clinical load. However, this may compromise their calculations accuracy. Modern radiotherapy treatments techniques are developing rapidly and continuously, opening doors for more complex patient treatments. Such complexity adds challenges to treatment planning (TP) dose calculation algorithms.

Monte Carlo (MC) method calculates the dose using random sampling of the particle state during its transport in a medium. It has been accepted as the "gold standard" in dose calculations (Rogers, 2006) and arguably is comparable to experimental measurements in terms of reliability of its dose estimates (Verhaegen & Seuntjens, 2003). Unlike analytical calculation methods, MC provides a stochastic solution that requires longer time and more computing resources.

The following sections introduce these dose calculation approaches and the basic principles behind each one.

1.4.1. Monte Carlo methods in radiotherapy

Radiation transport through media is governed by the statistical nature of particle interactions. The physics of different radiation interactions with matter and their probability distributions are well understood. Therefore, it is possible to simulate and predict the transport behavior of a particle using Monte Carlo (MC) methods. MC methods implement random number generator algorithms to simulate the particle transport. In other words, MC approach can be used to solve the linear Boltzmann particle transport equation (LBTE) stochastically.

The MC technique, as we know it today, was used at the end of the second world war to accurately calculate neutron transport which was essential for the atomic bomb design. The development of the first electronic computer, ENIAC, allowed Ulam and von Neumann to use MC for stochastic sampling. (Chetty et al., 2007; Seco & Verhaegen, 2013). The basics of MC approaches and its application in medical physics is introduced in this section.

MC basics: random number generators

Random number generators (RNGs) are the core of any Monte Carlo algorithm. MC uses a RNG coded subroutines to solve a problem via the random sampling. More accurately, RNGs are pseudo-random number generators since the outcome of any computer program is predictable. Therefore, the quality of "randomness" in generated numbers must satisfy certain criteria and need to be tested. The produced random number sequence must be long enough to avoid recurrence that causes correlation between the generated numbers. They also must be uniformly distributed within some interval or domain. (Seco & Verhaegen, 2013)

An example of RNG's is Lehmer's multiplicative-linear-congruential generator which is one of the most commonly and simple RNG used. The random number is generated using a modulus "**M**", a multiplayer "**c**" and "**a"** and seed "I_0" through the following recurrence relation:

$$I_{j+1} = \left(a\, I_j + c\right) modulo\ M$$

The above relation generates a sequence of random integers $I_1, I_2, I_3, I_4, \ldots$ each is within the interval $[0, M-1]$. Where **a** and **c** are constants and **M** usually chosen to be $2^{\mathbf{b}}$. **b** is the number of bits representation of the data in a computer.

As an example of the above class-generator implemented for medical physics and used in the old EGS4 Monte Carlo system (Nelson, Hirayama, & Rogers, 1985) is the SLAC RN6 generator

$$I_{j+1} = a\, I_j$$

With,

$$a = 663608941$$

$$c = 0$$

$$M = 2^{32}$$

This generator is "in-line" coded within the EGS program which makes it fast since no subroutine calls are initiated during the simulation. One drawback for this generator is the relatively short sequence it produces which makes it unsuitable for lengthy MC simulations.

Nowadays most of radiotherapy MC software implement more advanced RNG algorithms capable of producing higher quality random numbers. For instance, the RNG's known as RANMAR and RANLUX are implemented in the EGSnrc system (Iwan Kawrakow, 2001). RANMAR is a long-sequence RNG function provided by the CERN program library (https://home.cern). RANMAR has a length of 2^{144}. RANLUX function allows different luxury levels and therefore produce random numbers with higher quality.

As mentioned earlier, random sampling is the fundamental concept of Monte Carlo method. Computer generated RNG's are used to sample particle trajectories and interactions based on known probability density functions (PDF). This can be achieved by using two MC sampling approaches: the acceptance-rejection methods, the direct (or the inverse) sampling method.

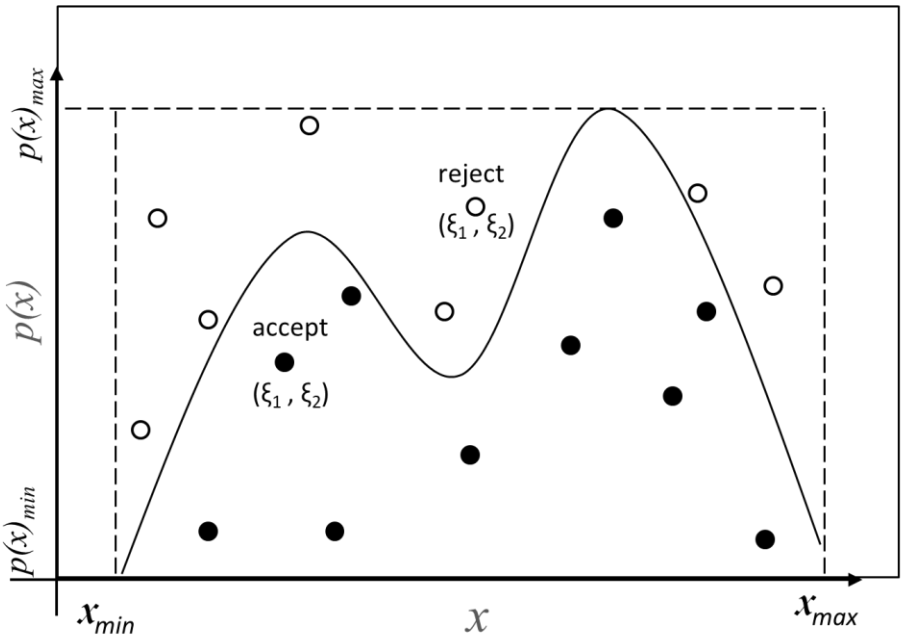

Figure 1.5: A diagram illustrating the MC acceptance-rejection sampling approach to calculate the area under p(x).

To illustrate the acceptance-rejection approach, let us consider the example of PDF *p(x)* shown in figure 1.5. Acceptance rejection approach can be used to calculate the area under *p(x)* as follow. The area under *p(x)* can be completely enclosed by a rectangular sampling envelope. N points are sampled uniformly throughout the rectangular envelope by generating a pair of random numbers ξ_1 and ξ_2, where:

$x_{min} \leq \xi_1 \leq x_{max}$ and

$p(x)_{min} \leq \xi_2 \leq p(x)_{max}$

Each time $x=\xi_1$ is generated, $p(\xi_1)$ is evaluated and compared to ξ_2. When $\xi_2 \leq p(\xi_1)$, ξ_1 is accepted, otherwise it is rejected and another set of (ξ_1, ξ_2) is generated and so on. Therefore, for large number of samples ξ_1 can be regenerated as *p(x)* using two uniform distributions of the random numbers.

The second MC sampling approach is known as inverse or direct sampling. In this approach random numbers are generated from a probability density function *p(x)* by using the inverse of its cumulative distribution function (CDS) P(x). The cumulative distribution function P(x) can be calculated as

$$P(x) = \int_a^b p(x')\, dx', \qquad (1.6)$$

$a \leq x \leq b, P(a) = 0, P(b) = 1$

The values of the probability density function fall within the interval [0, 1] then x can be determined as

$$x = P^{-1}(x) \qquad (1.7)$$

where x is a uniformly continues random variable.

MC modeling of photon transport is a direct application of the inverse sampling approach. For photons transport in an infinitely thick slab of material, the probability in which a photon travels a distance *x* before it interacts is

$$p(x) = \mu e^{-\mu x}, 0 \leq x \leq \infty \qquad (1.8)$$

where μ is the sum of linear attenuation coefficients (cm^{-1}) for all interaction types in material at given energy.

The CDF can be calculated as

$$P(x) = \int_0^x \mu e^{-\mu x'}\, dx' = 1 - e^{-\mu x} \qquad (1.9)$$

Using the inverse approach x can be easily sampled as in equation 1.7

$$x = -\frac{1}{\mu}\ln(1 - P(x)) \text{ for } 0 \leq P(x) < 1 \qquad (1.10)$$

Notice that P(x) is uniform between (0,1), therefore x can be sampled by generating uniformly random numbers ξ=P(x) distributed within [0-1].

This approach is fast and can be easily coded however it only works when CDF can be inverted.

Several MC systems are now available and used for radiotherapy calculations. The EGSnrc (electron gamma shower) is one of those MC computer codes designed specifically to simulate the transport of electron and photon interactions in a media. EGSnrc is an improved version of the EGS4 developed by Nelson et *al*. (1985, p. 4), at the Stanford linear accelerator center. The EGS code calculates a quantity of interest, such as fluences, by averaging over a set of MC simulated events or histories. Modifications introduced to EGS4, by the National Research Council of Canada (NRC), improved its use in radiotherapy modeling. The details and the physics of this code can be found in NRC technical report PIRS-701 by Kawrakow and Rogers (2001).

There are several specialized packages released under the EGSnrc Monte Carlo system. BEAMnrc, DOSXYZnrc and egs_chamber are examples of these specialized user codes and were used extensively throughout the different projects of this dissertation.

BEAMnrc Monte Carlo code is a specialized package that facilitates modeling of a radiotherapy linear accelerators (linac). This code provides the user with the various geometrical components needed to model a full linac such as the primary collimator, mirror, ionization chamber and the jaws. A full linac model or phase-spaces could be used to model the transportation of particles throughout the modeled linac parts to create a virtual radiation beam that reflects the dosimetric characteristics of that generated by a real linac.

DOSXYZnrc MC code is used to calculate the dose in phantoms or patent CT images. Full linac or phase-space files created using BEAMnrc, for instance, are used as input in DOSXYZnrc to simulate the particle transportation in voxelized phantoms in order to calculate the dose.

Egs_chamber (Wulff, Zink, & Kawrakow, 2008a) is an EGSnrc user code developed for modeling radiotherapy dosimeters. This code also uses a source input such as full BEAMnrc linacs or phase-spaces. The egs_chamber user code is used to assess a detector's dose corrections factors. The simulation efficiency is improved for this user code due to implementation of several variance reduction techniques. Specifically, there are three techniques that are implemented: photon cross-section enhancement (XCSE), an intermediate phase-space storage (IPSS) and correlated sampling (CS). For more detail about the implemented VR techniques the user is referred to Wulff *et al* (2008a)

The accuracy of Monte Carlo calculations depends on the number of simulated events or histories. The uncertainty is, in general, proportional to the inverse square root of the number of histories ($\sigma = \frac{1}{\sqrt{N}}$). Therefore, a balance must be found between achieving low statistical uncertainty and maintaining acceptable computing time and power in such simulations. For this

reason, MC system includes variance reduction algorithms such as particle splitting, Russian Roulette, energy cutoffs and many others, that can be used to increase the simulation efficiency while maintaining an acceptable accuracy.

However, even with the implementation of such variance reduction techniques (VRT) to increase the MC dose calculations efficiency, still MC approach consumes excessive amount of time and calculation power. For this reason, MC methods so far found only limited use in clinical implementation where time is an important factor.

1.4.2. Treatment planning dose algorithms: AAA and AcurosXB

The advancement in clinical Treatment Planning (TP) dose calculation algorithms is bounded by the necessity of getting the calculations within an acceptable time window, which may compromise the calculation accuracy.

Convolution/superposition is probably the most commonly used group of algorithms in modern TP dose calculations. Their implementations, such as anisotropic analytical algorithm (AAA), (Sievinen, Ulmer, & Kaissl, 2005; Ulmer & Kaissl, 2003) where the lateral electron/photon scatter component is modeled as a variable in different directions, a considerably improved calculation accuracy compared to previously used pencil beam convolution algorithms.(Gagné & Zavgorodni, 2007; Van Esch et al., 2006)

The Acuros XB dose calculation algorithm, released by Varian Medical System for the Eclipse treatment planning system (Varian Medical Systems, Palo Alto, CA), is the grid-based LBTE solver. It provides a deterministic solution for the LBTE, unlike the MC approach, where the solution is achieved stochastically. Acuros XB was shown to be more accurate than AAA and CCC in calculating the dose in regions with complex geometries and heterogeneities. (K. Bush, Gagne, Zavgorodni, Ansbacher, & Beckham, 2011; Failla, Wareing, Archambault, & Thompson, 2010; Fogliata, Nicolini, Clivio, Vanetti, & Cozzi, 2011; Fogliata, Nicolini, Clivio, Vanetti, Mancosu, et al., 2011; Kan, Leung, So, & Yu, 2013; Kan, Yu, & Leung, 2013; Vassiliev et al., 2010). Bush *et al*. (2011) validated Acuros XB against MC in multi-slab heterogeneous phantoms with low- and high-density heterogeneities. Calculated PDD and lateral profiles demonstrated superiority of Acuros XB over AAA.

1.5. Dissertation objective

Dosimetry at non-CPE regions requires advanced and specialized techniques for accurate dose assessments. These regions, as mentioned earlier, lack CPE condition which complicates the dosimetry process and ultimately could lead to inaccurate dose evaluation. The dissertation consists of two main objectives, each of which address a non-CPE situation and would be

presented separately in two different chapters. The main scope of the thesis is to accurately evaluate the dose in two non-CPE regions: interfaces of heterogeneities as well as small and very small photon beams. To achieve these objectives, the following tools and methods were developed during this work:

(1) Development and validation of a new film calibration approach.
(2) Comparison of dosimetry techniques near low and high density media interfaces.
(3) Commission and benchmark MC model used for the small field calculations.
(4) Deriving output correction factors for microDiamond and EFD-3G detectors to provide accurate dose measurements in small radiotherapy fields.
(5) Evaluation of the latent variances of the Varian phase-space files for small fields calculations.

GafChromic EBT2/3 films are used extensively in most of the thesis work presented here. To achieve high measurement accuracy, a more sophisticated film dosimetry protocol is implemented to minimize, as much as possible, the uncertainties that arise from the different film dosimetry stages. Chapter 3, presents the methods and materials of the implemented film dosimetry protocol. This protocol is tedious and require significant effort and time. Therefore, to increase the efficiency of the film dosimetry, a new film calibration approach is developed and used. In this protocol, the new film dose calibration method is based on PDD tables. The film PDD-calibration approach is benchmarked against a typically used calibration method. The results show that the new PDD film calibration method is faster and more accurate than the benchmark calibration method. This project is presented in Chapter 3.

In Chapter 4, dosimetry at interfaces is presented. This chapter provide dose evaluation near interfaces of heterogeneities. GafChromic EBT2 film and MOSkin detectors, as well as MC calculations, are used to estimate the dose near extreme media heterogeneities irradiated by 6 and 18 MV beams of different sizes. The dose is measured using films and MOSkin detectors near water–air, water–steel, and water–lung interfaces. The measured dose is then compared against MC calculations, as well as to AAA and Acuros XB predictions. This combination of experimental and MC methods will allow for testing accuracy of commercial algorithms. It will also allow evaluation of accuracy and consistency of “benchmarks” —experimental measurements and MC in extreme conditions.

The limitations of using phase-space files (PSF) as a source in the small filed MC dose calculations are investigated in Chapter 5. It is well known that some MC applications are likely to require summing up more PSFs than others depending on the beam energy, field size, and grid resolution of the dose scoring volume. Chapter 5 provides an evaluation of the latent variances from version 2 of the Varian TrueBeam photon PSFs for different beam energies, phantom voxel size and beam field sizes including small fields that are used in stereotactic radiosurgery (SRS)

treatments. Eventually, estimation on the number of phase-space files, or particles, required to achieve sub-percent latent uncertainty is provided.

In Chapter 6, the detector correction factors are obtained to provide accurate dose measurements in small radiotherapy fields. The output factors (OF), for Varian TrueBeam linac with circular cones of 1.3, 2.5, 3.5, 10, 12.5, 15 and 40 mm diameters are measured using GafChromic EBT3 films, microDiamond, and an electron EFD-3G diode detector. They are also calculated with MC using BEAMnrc and DOSXYZnrc codes (Rogers, Walters, & Kawrakow, 2009; B. Walters, Kawrakow, & Rogers, 2005). $k_{Q_{clin},Q_{msr}}^{f_{clin},f_{msr}}$ correction factors, as defined by Alfonso *et al* (Alfonso et al., 2008), have been derived experimentally and using MC for PTW-60019 microDiamond and EFD-3G detectors. $k_{Q_{clin},Q_{msr}}^{f_{clin},f_{msr}}$ correction factors were calculated for several detector orientations relative to the beam central axis (CAX). Impact of the variations in microDiamond detector geometries on calculated $k_{Q_{clin},Q_{msr}}^{f_{clin},f_{msr}}$ correction factors was also investigated.

Chapter 7 presents the final conclusions and summarizes the results of the dissertation. The results of the work presented in this dissertation have been published in the refereed journals.

2. Chapter 2
Background: The dose calculation methods used in this research

This chapter presents the general and common methods and materials implemented for the MC calculations performed in the thesis. Section 2.1 summarizes the EGSnrc system and the implemented physics to simulate the particle transportation in the medium. Sections 2.1.1, 2.1.2 and 2.1.4 summarize the different specialized EGSnrc MC codes as well as the common simulation parameters implemented in each of them. In section 2.1.3, the latent variance of a phase-space file and its estimation techniques are introduced. Finally, the TPS dose calculation algorithms used in the thesis (AAA and Acuros XB) are summarized in section 2.2.

2.1. EGSnrc Monte Carlo system: BEAMnrc, DOSXYZnrc and *egs_chamber* codes

EGSnrc Monte Carlo system (Iwan Kawrakow, 2001) models the photon and electron transport in a medium based on the known physics of their interactions within matter as described earlier in Chapter 1. Photons undergo fewer interaction events compared to electrons due to the differences in their physical properties. The transport of photons in EGSnrc is simulated based on event-by-event modeling which is simple and requires less computation power. Electrons, on the other hand, undergo hundreds of thousands of interactions within the matter. Thus, modeling their transport using the event-by-event simulation approach is not feasible as it requires a tremendous amount of computation power. To overcome this problem, condensed history (CH) and multiple scattering approaches are implemented in EGSnrc to simulate electron transport. In the CH approach, large number of subsequent transport interaction processes are condensed into a larger single step with a scattering angle sampled from known multiple scattering (MS) distributions. This approach drastically reduces the computation load and increases the simulation efficiency.

In EGSnrc, electron transport for both elastic and inelastic collisions are simulated explicitly above certain energy threshold. The above threshold interactions are referred to as “catastrophic” collisions and only sub-threshold events are subject to grouping into a single CH step. For the sub-threshold interactions, the particles transport is modeled using a continuous

slowing down approximation (CSDA). To overcome such a drawback, EGSnrc implemented different boundary crossing algorithms (BCA) that handle transportation of electrons differently at boundaries as explained below.

In CH approach, an artificial parameter known as a step-size is introduced to control the sampled step length. The sampling step length must be carefully selected in the CH approach as it could result in inaccuracies in the calculations near interfaces of heterogeneities. Bielajew *et al.* (1986) developed an electron transport algorithm that was implemented in EGS4 MC system. The developed Parameter Reduced Electron-Step Transport Algorithm (PRESTA) automatically selects the optimum electron-step length. PRESTA (known as PRESTA-I) significantly reduced the computation time as compared to previous electron-step algorithm implemented in the early EGS MC code (Bielajew & Rogers, 1986). The PRESTA-I CH transport algorithm was found to produce singularities at boundaries caused by the algorithm forcing MS sampling at interfaces (I. Kawrakow, 2000). Previously EGS4/PRESTA implemented Molière's multiple scattering theory to sample the scattering angle for a CH step. This theory was shown to breakdown at short pathlengths simulations (Pedro Andreo, Medin, & Bielajew, 1998) and large scattering angles. The new EGSnrc PRESTA-II electron transport algorithm is a refined version of the PRESTA-I transport algorithm that implemented a more accurate MS theory. The exact Goudsmit–Saunderson (GS) formulation along with the screened Rutherford single elastic scattering cross sections are implemented. EGSnrc uses MS models for larger steps but in the vicinity of interfaces converts to single scattering simulation for shorter sampling steps to avoid artifacts created in the EGS4 calculations. This is achieved by selecting the transport algorithm with the "EXACT" boundary crossing algorithm (BCA). EXACT BCA enforces single scattering mode near the boundaries to remove artifacts in the calculations by allowing more accurate sampling of particle interaction position.

In this work, MC calculations were performed using different specialized EGSnrc codes: BEAMnrc, DOSXYZnrc and *egs_chamber*. Doses were calculated in phantoms of complex geometries and heterogeneous structures. Thus, the default PRESTA-II EXACT boundary crossing algorithm was used in DOSXYZnrc for calculations within the phantoms (Chapter 4) and in *egs_chamber* for dose calculations in the detectors models (Chapter 6). Some transport parameters will be further specified in the relevant chapters, however, a summary of the most common EGSnrc transport parameters used in the study are presented in Table 2.1.

Table 2.1: A summary of the EGSnrc transport parameters used in DOSXYZnrc and BEAMnrc simulations.

Simulation Parameter	EGSnrc Values

	DOSXYZnrc	BEAMnrc
Global PCUT (MeV)	0.01	0.01
Global ECUT (MeV)	0.512	0.7
Global SMAX (cm)	1e10	5
ESTEP (%)	0.25	0.25
XIMAX	0.5	0.5
Boundary crossing algorithm	EXACT	PRESTA-I
Skin depth for BCA (mean free paths)	3	0 (default)
Electron-step algorithm	PRESTA-II	PRESTA-II
Spin effects	On	On
Brems angular sampling	Simple	KM
Brems cross sections	BH	BH
Bound Compton scattering	Off	Off
Pair angular sampling	Simple	Simple
Photoelectron angular sampling	Off	Off
Rayleigh scattering	Off	Off
Atomic relaxations	Off	Off

Table 2.1 present the input values of the simulation parameters used in the EGSnrc MC codes. These parameters can be controlled within DOSXYZnrc and BEAMnrc input files. Global PCUT and ECUT determine the cutoff energies (in MeV) at which the simulation of photon and electron are terminated and their energy is deposited locally. Global SMAX parameter defines the maximum electron-step length in centimeters. There is no restriction on the step length when EXACT BCA is implemented and by default it is set to a very large number (1E10). However, a reasonable value of SMAX must be selected when PRESTA-I BCA is used to ensure proper electron transport in low-density material (such as air) as per the BEAMnrc manual. In BEAMnrc simulation, PRESTA-I is the used BCA and thus a value of 5 cm was assigned to SAMX as recommended by BEAMnrc manual (Rogers et al., 2009). The parameter ESTEP defines the maximum fractional energy loss per electron step. In this work, a value of 0.25 (25% energy loss per step) was assigned to ESTEP as per BEAMnrc/DOSXYZnrc manual recommendation (Rogers et al., 2009; B. Walters et al., 2005). XIMAX is the maximum first multiple elastic moment per electron step and is assigned a value of 0.5 which is deemed to be sufficient for most applications. The electron spin is turned on in both BEAMnrc and DOSXYZnrc calculations of elastic scattering cross-sections that are used in electron transport. These cross-sections take into account the relativistic spin effect that is necessary for accurate backscatter calculations such as those performed in Chapter 4 (B. Walters et al., 2005).

The rest of the parameters, shown in Table 2.1, are assigned default values. The differential cross-sections for Compton scattering is determined using the Klein-Nishina formula (Bound Compton scattering = off). Brems, Pair and Photoelectron angular sampling input parameter determine the type of angular sampling scheme used in

the bremsstrahlung, pair production and photoelectron interaction events, respectively. `Brems angular sampling` is set to `KM` and thus the polar angle of the emitted bremsstrahlung photon with respect to the initial electron direction is sampled using a modified 2BS equation from Koch and Motz (Koch & Motz, 1959). For this interaction process, the Bethe-Heitler (BH) cross-sections are used by assigning "`BH`" to the parameter `Brems cross sections`. `Pair angular sampling` is set to `Simple` (the default) and therefore only the first term of the 3D-2003 equation from Motz *et al.* (1969) is used to determine the positron/electron emission angles. The input `Photoelectron angular sampling` is turned Off, therefore, photoelectrons inherit the direction of the incident photon. Both Rayleigh scattering and atomic relaxations events were not simulated in any calculations performed in this work.

2.1.1. BEAMnrc: Photon source simulation

BEAMnrc is a specialized EGSnrc MC code designed to facilitate the modeling of a radiation source such as linac head. Linac head can be simulated using a library of existing codes (called Component Modules (CMs)) that model various geometrical shapes. All relevant linac CMs available in the BEAMnrc software are modeled based on the geometric details and material specifications provided by the linac manufacturer. The generated photon fluence from modeled linac head should produce beam output characteristics similar to those of a real linac.

In this work, BEAMnrc is used to simulate a radiation beam by simulating transport of the particles throughout linac components. The linac head model contained a target, primary collimator, flatting filter, mirror, ionization chamber and secondary collimators (jaws). Figure 2.1 shows a diagram illustrating this model. In this model electrons hit the target to produce the photons and BEAMnrc simulates their propagation throughout the linac head. The simulation in BEAMnrc is often carried out in two steps. First, simulated particles are transported through components that are fixed and don't vary with different radiotherapy beams. As these particles cross a certain plane, that is usually set above the secondary collimators, the particles are stored in a phase-space file (PSF). These PSFs contain essential parameters of the stored particles such as their positions, energies, weights, and directions. In the second stage, these PSFs are used as a particle source to continue the transport of the stored particles through a required collimation system(s) and further into a phantom.

In Chapter 4, BEAMnrc was used to model photon radiation beams. A previously commissioned Varian 21EX linac head model available at Vancouver Island MC (VIMC) web server (S. Zavgorodni, Bushz, Locke, & Beckham, 2007) was used to model the 6 and 18 MeV photon beams. These models have been previously established and benchmarked (K. Bush et al., 2011; Karl Bush, Zavgorodni, & Beckham, 2009; Gagné & Zavgorodni, 2007; S. Zavgorodni, Locke, Bush, & Beckham, 2005). The model of the linac head was then compiled as a shared

library to be used as a complete accelerator "source" along with DOSXYZnrc code. In such approach, histories are simulated starting from electron beam hitting the target and down through the accelerator head until it deposits its energy in the phantom.

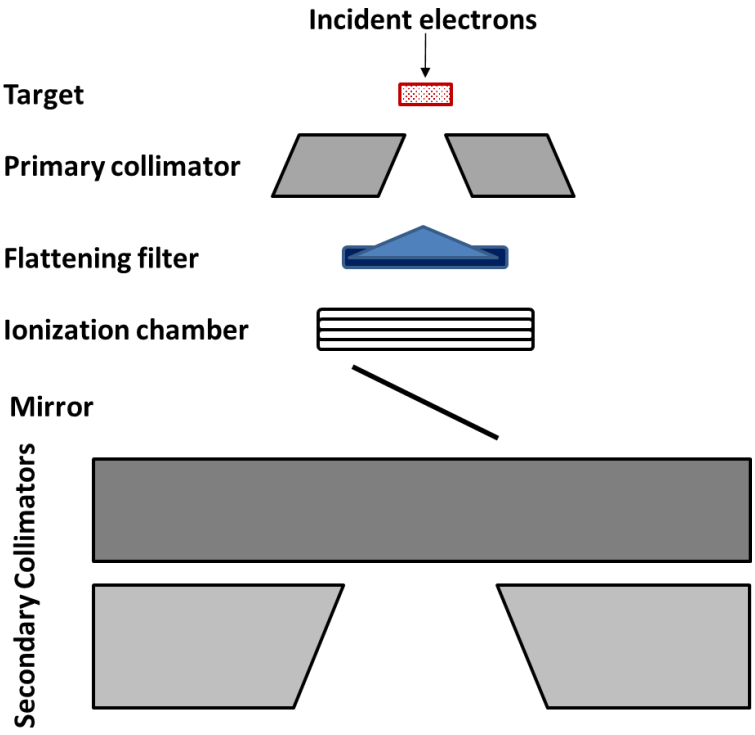

Figure 2.1: A diagram illustrating the main modeled parts for the 21EX linac head.

In Chapter 5 and 6, Truebeam PSFs, provided by Varian, were used as a source in BEAMnrc. These phase-spaces were also scored above the collimators.

2.1.2. DOSXYZnrc: dose calculation in phantoms

DOSXYZnrc is an EGSnrc user-code that enables dose calculations in phantoms. The transport of photons and electrons is simulated in 3-D Cartesian geometry and their energy depositions are scored in small rectangular volumes (voxels). Conventionally, co-ordinate system of the volume has x-y plane on the page, where the x-axis is to the right and the z-axis into the page. The material and density of each voxel can be set independently by the user.

DOSXYZnrc allows various particle source configurations including monoenergetic diverging and parallel beams as well as phase-space data generated by BEAMnrc simulations. The code also allows using a full linac BEAMnrc model as a source that generates the particles. Throughout the thesis, the code was used with two source configurations: full linac beam and phase-spaces source configurations.

In Chapter 4, full BEAMnrc treatment head was used as a source in DOSXYZnrc to calculate the doses near interfaces. In this chapter, Varian 21EX Clinac model described in section 2.1 was used as a shared library source within DOSXYZnrc MC code. DOSXYZnrc then transported particles through a 20×20×20 cm^3 water phantom to calculate the lateral dose profiles and percent depth doses (PDDs). In Chapters 5 and 6, we used full phase-space file as a source in DOSXYZnrc for latent variance estimations (Chapter 5) and output factors and dose profiles calculations (Chapter 6).

The statistics on the scored doses in DOSXYZnrc are determined by grouping the scored quantities based on the history-by-history approach (B. R. B. Walters, Kawrakow, & Rogers, 2002). For most sources, quantities are traced back to the original incident particle. When a phase-space file is used as an input source, particles are grouped by a primary history. A primary history is defined in EGSnrc as a MC trajectory, that originates from the initial electron entering the linac head; it includes all secondary generated particles, and all its occurrences created due to recycling or other variance reduction technique (notice that this definition of "primary" is different to primary and secondary particles as defined in radiotherapy physics). This is described in detail in the paper published by Walters *et al.* (2002). The history by history statistical uncertainty approach takes into account the latent variance of the phase-space when used as an input source.

2.1.3. Latent variance of Phase-space files

In EGSnrc system, there are various VRTs that could improve the simulation efficiency and the statistics in a calculated quantity. These reduction techniques, such as the particle splitting and recycling, are used to artificially increase the density of particle interactions within the volume of interest and hence reduce the variance. However, Sempau *et al* (2001) showed that regardless of VRT used in the phase-space particles' transport through a phantom, the variance of a calculated quantity cannot be reduced below a certain limit. This smallest possible value of the variance was named as the latent variance (LV) (Sempau et al., 2001).

As mentioned earlier, the linac manufacturer only released a limited number of PSFs per beam energy for MC calculation purposes. PSF provides a limited number of particles when used

as a source compared to much larger number of particles that can be simulated from the full linac head model. The achievable accuracy in MC dose calculations that use PSFs as a particle source are limited by the phase-space LV. Therefore, larger PSFs have to be used to improve the calculation statistics. In Chapter 6, PSFs from small collimators were used to calculate the doses in very small volumes. Such calculations require large number of particles to achieve acceptable statistical uncertainties in the calculated doses. Thus, it was important to provide an assessment of LV for these PSF before performing any MC calculations.

Sempau *et al* (2001) proposed a technique to evaluate latent variance of PSF. The latent variance in a calculated quantity $\sigma_K^2(\bar{q})$, such as dose deposited in a voxel, can be expressed as

$$\sigma_K^2(\bar{q}) = \frac{1}{N}(A + B \cdot K^{-1}) \qquad (2.1)$$

where N is the number of primary histories contributing to the scored quantity (q) directly or through its secondaries. A and B in Equation (2.1) are two terms calculated from the contributions of the particles simulated from a phase-space file. According to the above expression, the second term in the equation can be virtually reduced to near-zero when a very large K-factor is used in VRT downstream the scoring plan. In this case, the minimum achievable variance, i.e. the latent variance, is A/N.

Numerically, the latent variance can be estimated by running a few simulations transporting particles from the PSF into a phantom with increasing particle splitting factors K. The variance of the scored quantity is then plotted against K^{-1} and from the linear relation between the two, latent variance σ_K can be obtained from the linear-fit intercept at $K^{-1}=0$ as shown in Figure 2.2.

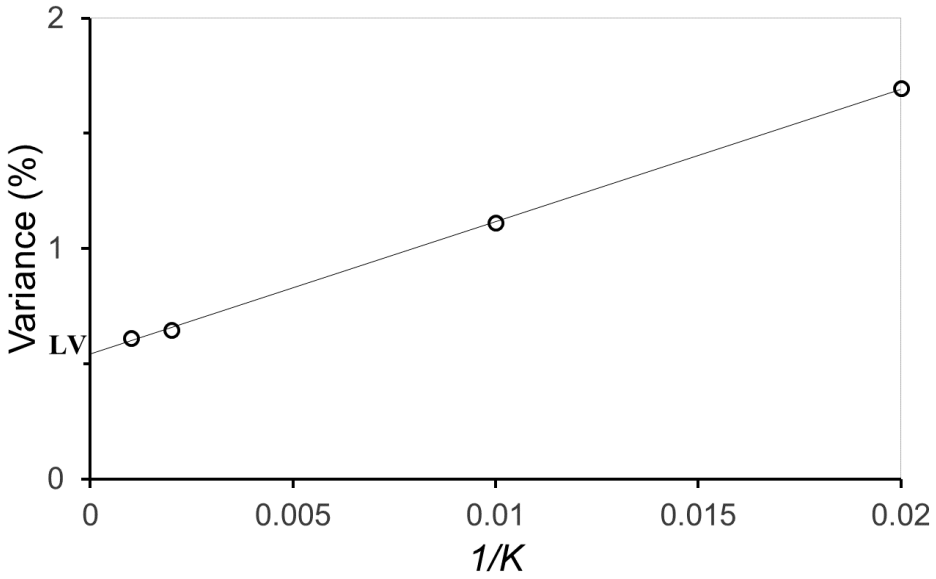

Figure 2.2: A plot showing the method of evaluating PSF latent variance (LV) as described by Sempau *et al*. MC variances are plotted against the inverse of particle splitting factors (K^{-1}) and fitted to a straight-line function. LV is obtained from the intercept of this line with the Variance axis (at K^{-1}=0).

2.1.4. The egs_chamber MC code: dose calculations in a detector model

The *egs_chamber* is an advanced EGSnrc C++ application developed specifically to calculate the dose to small detector volumes as well as dose ratios of two correlated geometries to obtain detector perturbation factors (Wulff, Zink, & Kawrakow, 2008b). The high efficiency of this application has been obtained by implementing three major VR techniques: photon cross section enhancement (XCSE), intermediate phase-space storage (IPSS) of the properties of particles entering user defined regions and correlated sampling (CS).

The IPSS and CS techniques are used in *egs_chamber* to avoid unnecessary repetitive simulations (full simulation) when only a small fraction of the overall geometrical model is altered. These two techniques therefore reduce the computation time and enhance the simulation efficiency. The IPSS method is very useful in dose profile (PDD or lateral) calculations using a real detector model in the phantom. In this method, transported particles are stored within an artificial volume that surrounds all possible detector locations required for the dose profile calculations. All single dose calculations for the different detector positions in the phantom are performed using the stored PSF as a source. In a similar approach, detector perturbation factors can be calculated using CS technique. Particles are transported only once through the phantom

rather than performing two (or more) full simulations for each detector model only differed by material compositions. In this method, stored particles, as in the IPSS, are transported twice for each of the detector models. In the XCSE, the photon interactions can be selected on a region-by-region basis to increase the particles interaction density by a certain factor. Wulff *et. al.* (2008b) showed that the XCSE technique has improved the calculation efficiency in a Farmer ion chamber type cavity by up to 350 times.

The *egs_chamber* also allows the use of different types of source configuration including PSF. In Chapter 6, PSFs from small collimators were used as a source within *egs_chamber* to calculate the dose ratios in the detectors' active volumes and to derive output correction factors for EFD-3G diode and microDiamond detectors.

2.2. TPS dose calculation algorithms: AAA and Acuros XB

AAA is an advanced superposition-convolution based algorithms implemented in the Eclipse (Varian Medical Systems, Palo Alto, CA) Integrated Treatment Planning System. AAA uses MC generated phases-spaces. The particle fluence and energy spectrum of these phase-spaces are tuned to match beam characteristic of a clinical treatment unit. The constructed broad beam source (phase-spaces) is divided into smaller pencil beams (beamlet). The energy fluence (Φ_β) within every single beamlet (β) is originated from three components: primary photon source, extra-focal photon source, and electron contamination source. This algorithm calculates the dose analytically in a voxel by convolving each of the beamlet energy fluence and energy deposition density function $I_\beta(z,\rho)$ with scatter kernels (K_β) that is also pre-calculated by MC method as

$$D_\beta(x,y,z) = \Phi_\beta \times I_\beta(z,\rho) \times \iint_\beta K_\beta(x'-x, y'-y, z, \rho)\, dx'\, dy' \qquad (2.2)$$

where $D_\beta(x,y,z)$ is the dose contribution from a single beamlet β to an arbitrary point in the patient.

The contribution from each of the three modeled source components is calculated separately and then combined in superposition. The total dose $D(x,y,z)$ deposited at a point in the patient is obtained by summing up the dose contributions from all individual beamlets in a final global superposition. During the 3D dose calculations, the pre-calculated kernels are scaled to the actual tissue densities obtained from the computed tomography (CT) images.

Acuros XB is an advanced dose calculation algorithm implemented in Eclipse TPS. Acuros XB directly solves the LBTE and was shown to be more efficient and more accurate than AAA (Eyad A. Alhakeem, AlShaikh, Rosenfeld, & Zavgorodni, 2015; K. Bush et al., 2011;

Fogliata, Nicolini, Clivio, Vanetti, & Cozzi, 2011). The three-dimensional time-independent coupled Boltzmann particle transport equations in a volume of matter are given by

$$\hat{\Omega} \cdot \vec{\nabla}\Phi^{\gamma} + \sigma_t^{\gamma}\Phi^{\gamma} = q^{\gamma\gamma} + q^{\gamma} \tag{2.3}$$

$$\hat{\Omega} \cdot \vec{\nabla}\Phi^{e} + \sigma_t^{e}\Phi^{e} - \frac{\partial}{\partial E}S_R\Phi^{e} = q^{ee} + q^{\gamma e} + q^{e} \tag{2.4}$$

where Equation (2.3) describes the photon transport and Equation (2.4) describes the electron transport. Here Φ^{γ} and Φ^{e} are the photon and electrons angular fluences, $\sigma_t^{\gamma}$and σ_t^{e} are the macroscopic photon and electron total cross sections. S_R is the restricted collisional plus radiative stopping power and the term $(-\frac{\partial}{\partial E}S_R\Phi^{e})$ represents the continuous slowing down operator which accounts for the soft electron collisions (Coulomb collisions). q^{γ} and q^{e} represent all photons and electrons coming from the machine source model (treatment head). $q^{\gamma\gamma}$ represent the photon-to-photon scattering source, q^{ee} electron-to-electron scattering source and $q^{\gamma e}$ represent the photon-to-electron source. In short, both equations 2.3 and 2.4 describe energy balance in the volume of interest due to photons (Equation 2.3) and electrons (Equation 2.4). The terms on the left-hand side of Equations 2.3 and 2.4 represent the energy carried away from a volume of interest by photons $(\hat{\Omega} \cdot \vec{\nabla}\Phi^{\gamma} + \sigma_t^{\gamma}\Phi^{\gamma})$ and electrons $(\hat{\Omega} \cdot \vec{\nabla}\Phi^{e} + \sigma_t^{e}\Phi^{e} - \frac{\partial}{\partial E}S_R\Phi^{e})$. Whereas, the terms on the right-hand side of the equations represents the energy carried in by photons and electrons coming from linac head ($q^{\gamma}$and q^{e}) and coming from scattering sources ($q^{\gamma\gamma}$, q^{ee} and $q^{\gamma e}$).

Acuros XB solves Equation 2.3 and 2.4 iteratively for the electron angular fluence by discretizing space, angle, and energy. Space is discretized using the linear discontinues finite-element method which provides a linear solution variation in each of the Cartesian space element. The multigroup and discontinues finite-element methods are used in the discretization of energy. There are 25 photon energy groups and 49 electron energy groups in Acurous XB cross section library. Lastly, discrete ordinate method is used to discretize in angle for the scattering source. Depending on the energy, this method discretizes the angle into 32-512 discrete angles.

Once the electron fluence is obtained the dose at an arbitrary point in the phantom is calculated as

$$D = \int_0^{\infty} dE \int_{4\pi} d\hat{\Omega} \frac{\sigma_{dep}^{e}(\vec{r},E)}{\rho(\vec{r})} \Phi^{e}(\vec{r},E,\hat{\Omega}) \tag{2.5}$$

where σ_{dep}^{e} is the macroscopic electron energy deposition cross section and $\rho(\vec{r})$ is the material density. The dose in Acuros XB can be reported as either dose-to-water (D_W) or dose-to-medium (D_M). The dose-to-medium calculations are obtained using σ_{dep}^{e} and ρ in Equation (2.5) of the output grid voxel. When dose-to-water is selected, σ_{dep}^{e} and ρ are based on water properties.

In Eclipse™ TPS, both Acuros XB and AAA algorithms share the same "multiple-source model" of the photon beam. It consists of primary photon source, extra-focal photon source, electron contamination source and photons scattered from wedges. Even though Acuros XB and AAA share the same multiple-source model, the model parameters may be different due to the differences in their dose calculation approaches (Fogliata, Nicolini, Clivio, Vanetti, Mancosu, et al., 2011; Tillikainen, Siljamäki, Helminen, Alakuijala, & Pyyry, 2007). Both algorithms require a set of open-field data measurements during the configurations.

3. Chapter 3
Materials and Methods: GafChromic EBT2/3 film dosimetry

GafChromic® EBT2/EBT3 films are used extensively throughout the thesis, owing to the advantages mentioned earlier in section 1.3.1. This Chapter presents the general methodology of the film dosimetry performed in Chapters 4 and 6. Section 3.1 summarizes some of the film dosimetry artifacts that could limit the measurements accuracy. In this study, an efficient film calibration approach using PDD tables is implemented and shown to be more efficient than the typical calibration method. Section 3.1.1 describes a "benchmark" calibration method that is based on film manufacturer recommendations. In Section 3.1.2, the new PDD film calibration method is described. The film scanning and handling process are presented in Section 3.1.3. Section 3.2 presents the methods and results of validating the new calibration method against the benchmark method.

3.1. GafChromic EBT2/3 film dosimetry protocol and dosimetric uncertainties

GafChromic film design and dosimetry are still under active development, aiming to improve the accuracy of the measured dose and the efficiency of the whole process. In recent years, flat-bed document scanners are being used as a two-dimensional densitometer in the film dosimetry. GafChromic film measurements with a flat-bed scanner are subject to various artifacts that could significantly limit the dose accuracy. These artifacts have been intensively investigated and can be eliminated or reduced using certain corrective measures (Arjomandy et al., 2010; Bilge, Cakir, Okutan, & Acar, 2009; Cheung, Butson, & Yu, 2006; S. Devic et al., 2006; Slobodan Devic et al., 2010, 2004, 2005; Ferreira, Lopes, & Capela, 2009; Lynch et al., 2006; Martišíková, Ackermann, & Jäkel, 2008; Richley, John, Coomber, & Fletcher, 2010; Saur & Frengen, 2008; Wilcox & Daskalov, 2007).

Based on these studies, extra steps and countermeasures are essential in order to mitigate the dosimetric uncertainties originating from different stages of a film dosimetry process. To shed some light on these artifacts, a typical film dosimetry process with flat-bed document scanner is summarized below.

The film dosimetry process consists of three main stages: calibration, scanning, and image dose readout. In the first stage, a film sheet is cut into 8—12 film pieces each with a size of about 5x5 cm^2. Films are then irradiated to known doses (in the range of 0 to 6 Gy). In the second stage, the irradiated films are scanned (digitized) using a flat-bed document scanner and images are saved as 48-bit red-green-blue (RGB) (16-bit per color) tagged image file format (TIFF). In the third stage, these images are processed using an image processing software to extract the pixel values (PVs) from an area located at the center of the irradiated film images. The PVs are then converted into optical densities (OD) within the irradiated area. Film ODs are related to the radiation doses through a calibration curve.

Dosimetric uncertainties mainly arise from two sources: artifacts due to film-inherent properties, and artifacts due to the scanning process. There are several artifacts that limit the measurement accuracy when a flat-bed scanner is used in the film dosimetry process. The films orientation dependency artifact, lateral film position on scanner artifact (lateral scan artifact (LAR)) and temperature of the scanner. Other artifacts are due to inherent characteristics of films, such as the non-uniform film thickness and post-irradiation darkening effect (Lynch et al., 2006; Saur & Frengen, 2008).

Film scanning orientation artifacts occur when the light source (scanner lamp) and the film are both linearly polarized. Therefore, variations in the measured OD density are expected when the film is rotated, causing a difference in the amount of light transmitted through the films. The LAR is caused by the non-uniform response of the scanner in the direction perpendicular to the direction of the lamp movement, which causes a variation in the measured PVs. Films scanned away (on either lateral sides of the scanner) appear to have smaller PVs (larger ODs) compared to when they are scanned at the center. This will result in a higher calculated dose. Also, it has been shown that the increase of the scanner lamp temperature due to multiple scanning in a measurement session results in an increase in the measured ODs (Lynch et al., 2006).

The thickness of the film is not perfectly the same through its area, and hence, there are variations in the transmitted light intensity through the film causing a difference in the measured responses. Darkening effect occurs due to the continuation of the polymerization process of the film after irradiation causing a noticeable increase in the OD. This will reach a plateau after a certain time. During scanning, EBT2 films also suffer from the formation of Newton's rings artifact when films are placed on the glass bed of the scanner. Destructive/constrictive light interference bands are formed in the gap between the film and the glass of scanner bed surfaces. This artifact has been reduced in the recently developed EBT3 film due to its improved structure and surface composition.

For these reasons, specific handling procedure is followed to reduce the influence of these artifacts on dose measurements and will be described in detail in the following sections.

The calibration process is laborious and time-consuming and that was the motivation behind the development of a simpler calibration approach. The new calibration approach incorporates the use of percent depth dose (PDD) tables. Section 3.1.2 summarizes the PDD calibration approach.

GafChromic EBT2 and EBT3 (Ashland ISP Advanced Material, NJ) are used throughout this study. The EBT2/3 film manufacturer provided handling and scanning recommendations based on previous publications on EBT and EBT2 film dosimetry. These recommendations provide some measures to reduce some of the mentioned artifacts. This protocol is commonly used across the literature that uses film dosimetry and will be described in the following sections. Finally, in Section 3.2 the new PDD calibration approach is validated against the benchmark calibration method that is described in Section 3.1.1.

3.1.1. Benchmark calibration

In the benchmark calibration, a sheet of GafChromic film is cut into 13 pieces each with a size of 5×5 cm^2. The orientation of the small film pieces relative to the original sheet is tracked and consistently scanned on the same orientation throughout the dosimetry process. This is to eliminate the film orientation artifact. A linac is used to irradiate the films while placed at a depth of 1.5 cm in a 30×30×30 cm^3 Solid Water "RMI-457" (Gammex RMI, Middleton, WI) (mass density ρ = 1.046 g/cm3) with 6 MV photon beam collimated by a 10x10 cm^2 jaws opening at 100 cm SSD. Each film piece is exposed to a known amount of radiation dose, ranging from 0 to 6 Gy, established during routine quality assurance measurement on the linac. After at least twenty-four hours, the irradiated films are scanned as per the description in Section 3.1.3. Then, the net optical densities (netOD) are obtained from the images as described in section 3.1.3. A calibration curve between netOD and the radiation dose (D) is generated and fitted using the analytical form as outlined in Devic *et al*. (2005):

$$D_{fit} = a \cdot netOD + b \cdot netOD^n \qquad (3.1)$$

where a, b and n are the curve fitting parameters. An example of a calibration curve is shown in Figure 3.4 (left).

3.1.2. PDD calibration approach

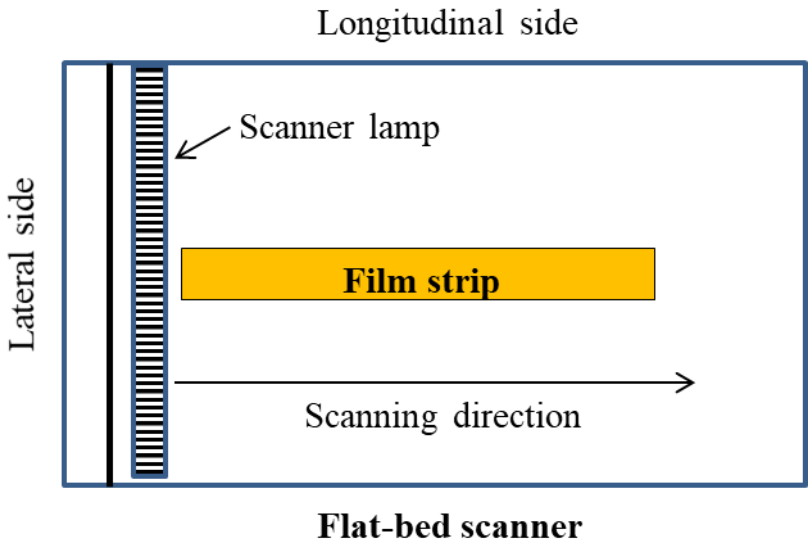

Figure 3.1: Diagram illustrating the flat-bed scanner and the scanning direction of the film strip on the scanner bed.

In the developed PDD calibration approach, a sheet of film is cut into 5 × 25.5 cm^2 strips. Three film strips are used to build the calibration curve. The film orientation is always marked and preserved during the cutting. The scanning direction of these strips is illustrated in Figure 3.1. A linac is used to irradiate the films while placed along the beam axis direction and sandwiched in the middle of a 30×30×30 cm^3 Solid Water "RMI-457". Linac gantry is rotated to 90^o angle to irradiate the films that are sandwiched between solid water slabs from the side with a typical PDD configuration, 10x10 cm^2 jaws opening at 100 cm SSD as illustrated in Figure 3.2. A dose of 6, 2 and 0.7 Gy to the depth of maximum dose (1.5 cm) is delivered to the three films. As a result of the dose attenuation in phantom with depth, the three film strips are exposed to a dose range from 0 to 6 Gy. After at least twenty-four hours, the films are scanned and processed as described in the following section. The netODs as a function of depth in water phantom are extracted from the film images. The calibration curve between PDD and netOD at corresponding depth in the water phantom is generated and is fitted using Equation 3.1. Only PDD values beyond the depth of maximum dose (d_{max}) are used in generating the calibration curve. This is to avoid any dose inaccuracies that may emerge from the non-equilibrium region.

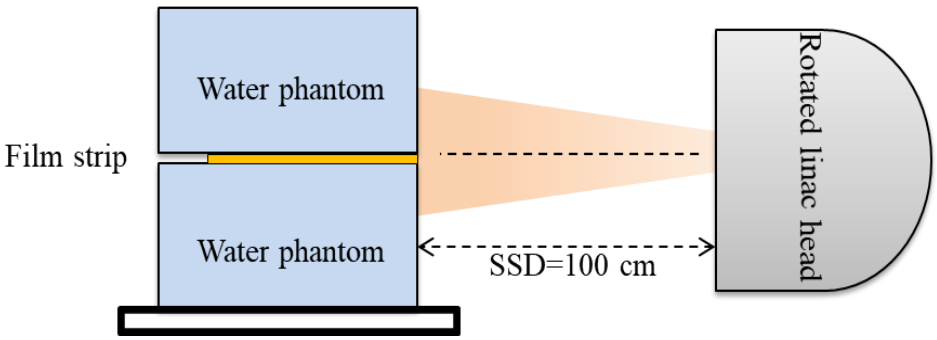

Figure 3.2: Diagram illustrating the beam and phantom setup for irradiating the film strips used in the PDD calibration approach.

3.1.3. Film scanning and image processing

An Epson 10000XL (Epson America, Inc., Long Beach, CA) flatbed document scanner is used to scan the films, as per the film manufacturer scanning protocol and recommendations (Ashland ISP Advanced Material). Before any scanning session, the scanner is warmed up for about ~15 minutes by performing consecutive "preview scans". This is to allow the scanner (lamp) temperature to stabilize during scanning. All films used for calibration (or measurements) are scanned three times before (pre-irradiation) and after (post-irradiation) irradiation. Also, to minimize scanner lateral positioning dependency, a plastic mask is used to reproduce film positioning after the exposure and to prevent them from touching the scanner glass surface, thereby avoiding Newtonian's rings (Saur & Frengen, 2008). Films are scanned at least twenty-four hours after exposure. Epson scanning software is used to scan the films in the transmission mode, with a resolution of 75-500 dpi and all image enhancements being turned off. The scanned films are saved as 48-bit TIFF images for further analysis.

The film images are processed using an in-house MATLAB (MathWorks, Natick, MA) code that filters (5×5 or 7×7 Wiener filter) and averages the three scanned images of each film to minimize scanning noise (Slobodan Devic et al., 2005; Saur & Frengen, 2008). ImageJ software (National Institute of Health, Bethseda, MD) is used to extract the pixel values (PV) from the red channel which provides maximum readout sensitivity (Ferreira et al., 2009). The netODs are then calculated as:

$$netOD = \log\left(\frac{PV_{pre}^{i}}{PV_{post}^{i}}\right) \tag{3.2}$$

where PV_{pre}^{i} is the pixel value reading of the averaged and filtered *i-th* piece pre- irradiation and PV_{post}^{i} is the pixel value reading of the averaged and filtered *i-th* piece post- irradiation. The dose reading is then derived from the calibration curve established according to either one of the calibration approaches described above.

During the measurement, films are prepared and handled as described above. However, it is typical to perform film measurements on a different date other than the date of calibration. The time gap between the calibration and measurement day could results in some uncertainties in dose readings. This is partly due to the gradual film darkening effect with time. Hence, film's fog base level (background) at measurement day is larger than that at calibration day. Also, the scanner readouts might vary from time to time due to variations in the intensity of the scanner light source between measurement and calibration day.

Therefore, to correct/eliminate these artifacts a piece of unexposed film from the calibration day is retained and kept in the same environment with the whole film batch. This piece is scanned at every dose measurement readout session in order to recalibrate the scanned films used for measurements to the scanning conditions and film's fog base level (background) at calibration day as follows:

- $$PV_{Measurement}^{Recal} = PV_{Measurement} \times \frac{PV_{Unexposed}^{M}}{PV_{Unexposed}^{Cal}} \quad (3.3)$$

where $PV_{Measurement}^{Recal}$ is recalibrated PV of an exposed film used on measurement day,

$PV_{Measurement}$ is the PV of the film exposed on the measurement day and scanned at time different than the calibration day.

$PV_{Unexposed}^{M}$ is the PV of retained unexposed piece of film scanned on measurement day.

$PV_{Unexposed}^{Cal}$ is the PV of retained unexposed piece of film scanned on calibration day.

In other words, the factor $\frac{PV_{Unexposed}^{M}}{PV_{Unexposed}^{Cal}}$ corrects for difference in the scanning output between calibration and measurement day. The net optical density for a measurement film ($netOD_M$) is calculated as

$$netOD = \log\left(\frac{PV_{Unexposed}^{M}}{PV_{Measurement}^{Recal}}\right) \quad (3.4)$$

The dose is then calculated using Equation (3.1). The total relative dose uncertainty (σ_D), including contribution due to calibration curve fit, is given by

$$\sigma_D(\%) = \frac{\sqrt{netOD^2 \cdot \sigma_a^2 + netOD^{2n} \cdot \sigma_b^2 + (a + n \cdot b \cdot netOD^{n-1})^2 \cdot \sigma_{netOD}^2}}{D_{fit}} \times 100 \quad (3.5)$$

where σ_a, σ_b are the uncertainties in the curve fitting parameters in Equation 2.1. σ_{netOD} is the uncertainty in the calculated *netOD* (Devic *et al* 2005). Film-based measurements of the dose, reported in our work, have a maximum uncertainty of ± 2.5% following the estimation approach by Devic *et al*. (2005), unless mentioned otherwise.

The implemented film dosimetry protocol is summarized in figure 3.3. Films were used to measure doses at build-up, interfaces, and to measure the output factors and lateral profiles for small collimators. Therefore, some of the above scanning and image processing details might vary depending on the application and will be specified within the relevant chapters accordingly.

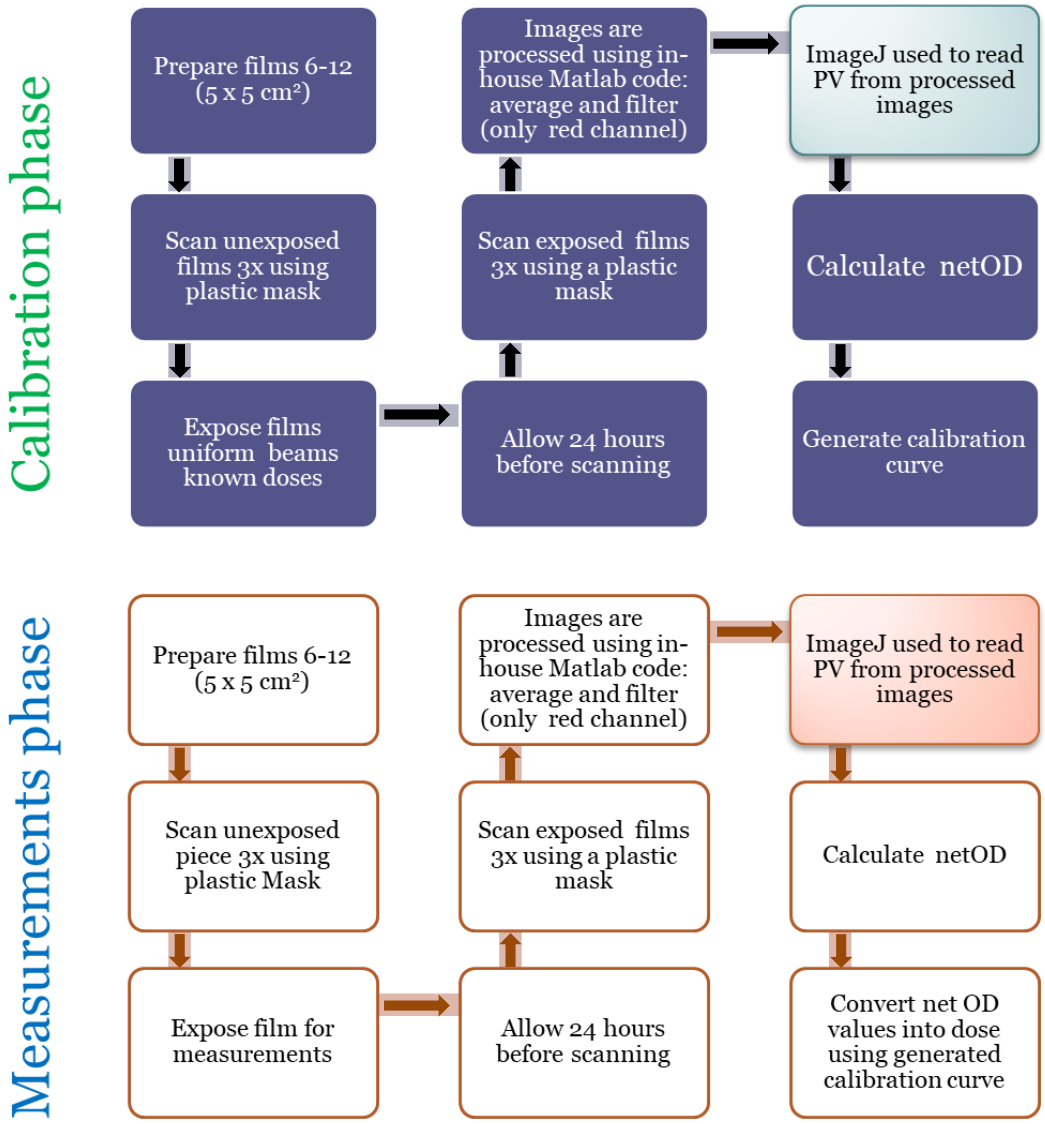

Figure 3.3: A chart summarizing the calibration and measurement steps.

3.2. Benchmarking the PDD calibration approach: Method and Results

The PDD calibration approach was compared against a benchmark calibration method in terms of its accuracy and efficiency. The film preparation, handling and scanning were performed as described earlier in Section 3.1.1 and 3.1.2. Both calibration curves were generated

using Equation 3.4 and are shown in Figure 3.4. The dose was measured from a set of seven films previously exposed to known doses ranging from 25 to 400 cGy. Dose readings were obtained from the exposed films using both calibration curves. The relative difference between the measured dose, using either of the calibration curves, and the known given dose was calculated.

3.2.1. Results

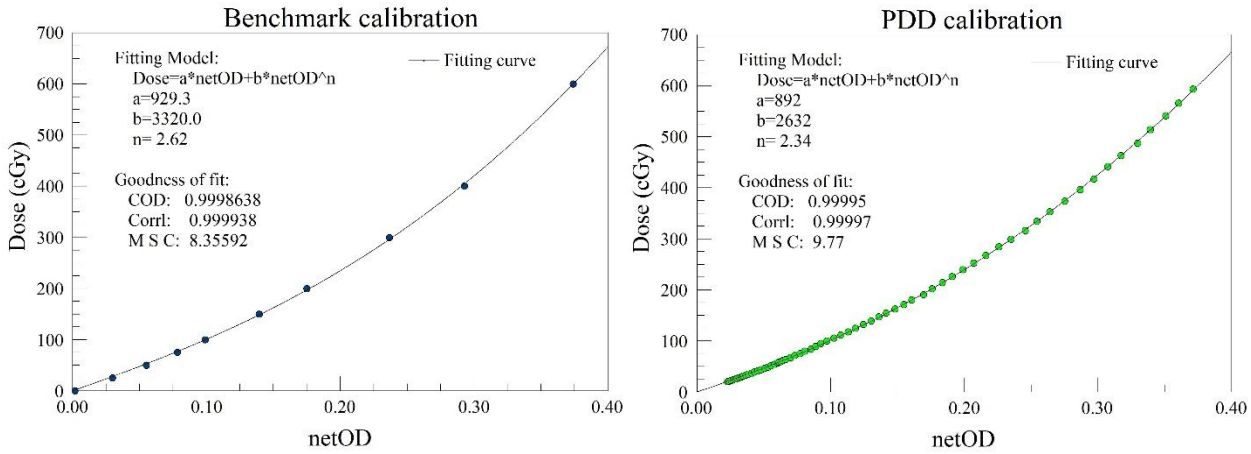

Figure 3.4: The film calibration curves generated using the benchmark calibration method (left) and the PDD calibration method (right) are shown. The uncertainty in dose (experimental only) were estimated from the standard deviation in the mean ODs that are extracted from a region of interest within the film. The estimated uncertainties are within ±1% for doses above 50 cGy.

Figure 3.4 shows two calibration curves generated by the PDD and the benchmark calibration methods. The PDD calibration approach provides noticeably more data points for generating the fitting curve using only three pieces of film.

Table 3.1: Film measurements of known radiation doses (25-400 cGy), determined from the PDD-based and the benchmark calibration mehtods are presented. The percent relative differences between known and measured radiation doses are shown. The total relative dose uncertainty (σ_D), including contribution due to calibration curve fit, in the reported dose measurements are within ±2% for doses above 50 cGy.

	PDD approach		**Benchmark approach**	
Given dose (cGy)	*Measured dose*	*% diff*	*Measured dose*	*% diff*

25	25.7	3.0	26.2	4.7
50	51.0	2.0	51.0	2.0
75	75.8	1.0	75.2	0.3
100	99.58	-0.5	98.4	-1.6
150	150.1	0.1	148.0	-1.3
200	200.1	0.0	197.5	-1.2
300	300.0	0.0	297.7	-0.8
400	408.1	2.0	407.3	1.8
	Mean difference	1.1 %		1.7 %
	SD	±1.2 %		±2.2 %
	Max difference	3.0 %		4.7 %

Table 3.1 presents the results of film measurements determined using the PDD and the benchmark calibration methods. This study showed that using the PDD calibration approach is much easier, faster and predicts the dose more reproducibly and accurately than the typically implemented benchmark calibration method.

The developed PDD calibration approach is implemented for our film measurements throughout the dissertation work, since it is efficient and accurate.

Chapter 4

The targeted tumor, in a radiotherapy treatment, is often surrounded by organs or tissues with different densities. Dosimetry near extreme density interfaces is difficult due to radiation disequilibrium condition as described in Chapter 1. Accurate dose calculations in TPS are essential for successful radiotherapy treatments. Therefore, the aim of this chapter is to provide an accurate dosimetry in one of the situations where CPE does not exist and to test the accuracy of Acuros XB —an advanced TP dose calculation algorithm. The content of this chapter was published in the *Journal of Applied Clinical Medical Physics* (Eyad A. Alhakeem et al., 2015)

AUTHOR'S CONTRIBUTION TO THE PUBLISHED PAPER

Contribution to the paper in this Chapter are:

Eyad A. Alhakeem, (Candidate)

Wrote the first draft of the manuscript and contributed to subsequent revisions. Also, contributed to the experiment design and performed most experimental work (film measurements, MC and TP dose calculations). Analyzed and interpreted the data.

Sami AlShaikh

Performed MO*Skin* measurements and analyzed the results.

Anatoly B. Rosenfeld

Contributed to the experimental design and editing manuscript.

Sergei F. Zavgorodni

Contributed to manuscript, the study design, and the data interpretation.

4. Dosimetry near low- and high-density heterogeneities

Modern radiotherapy treatment techniques are developing rapidly and continuously, opening the doors for more complex patient treatments. Such complexity adds challenges on treatment planning (TP) dose calculation algorithms. Historically, dose calculation algorithms improved significantly from simple dose correction-based methods to advanced convolution/superposition calculations and, further, to linear Boltzmann transport equation (LBTE) solutions. Developments in TP algorithms are always limited by the necessity of completing the calculations within an acceptable time window, which may compromise the calculation accuracy.

Monte Carlo (MC) method calculates the dose using random sampling of the particle state during its transport in a medium. It has been accepted as a "gold standard" in dose calculations (Chetty et al., 2007; Rogers, 2006) and arguably is comparable to experimental measurements in terms of reliability of its dose estimates (Verhaegen & Seuntjens, 2003).

Convolution/superposition is probably the most commonly used group of algorithms in modern TP dose calculations. Their implementations, such as anisotropic analytical algorithm (AAA) (Sievinen et al., 2005; Ulmer & Kaissl, 2003; Ulmer, Pyyry, & Kaissl, 2005) where the lateral electron/photon scatter component is modeled as a variable in different directions, considerably improved calculation accuracy compared to previously used pencil beam convolution algorithms (Gagné & Zavgorodni, 2007; Van Esch et al., 2006). However, AAA is still not able to accurately calculate doses at extreme density interfaces. Aarup et al. (2009) reported that discrepancies between AAA and BEAMnrc/DOSXYZnrc dose calculations increased as lung density decreased from 0.4 g/cm^3 to 0.01 g/cm^3. The differences for the lowest clinically meaningful lung density of 0.1 g/cm^3 were up to 5.9% and 8.9% when using 6 and 18 MV beams, respectively. The differences exceeded 10% and 30% for 0.01 g/cm^3 lung density for the 6 and 18 MV energies, respectively. Chow *et al.* (2011) evaluated AAA and collapsed cone convolution (CCC) algorithm against MC for oblique tangential photon beams and showed, in some cases, differences of up to 18.0% ± 1.3% and 8.3% ± 1.8% for AAA and CCC, respectively.

The Acuros XB dose calculation algorithm, released by Varian Medical System for the Eclipse treatment planning system (Varian Medical Systems, Palo Alto, CA), is the grid-based LBTE solver that models particles fluence transport in a medium. It provides a deterministic solution for the Boltzmann equation, unlike the MC approach, where the solution is achieved

stochastically. Acuros XB was shown to be more accurate than AAA and CCC in calculating the dose in regions with complex geometries and heterogeneities (K. Bush et al., 2011; Fogliata, Nicolini, Clivio, Vanetti, Mancosu, et al., 2011; Han et al., 2013; Han, Mikell, Salehpour, & Mourtada, 2011; Hoffmann, Jørgensen, Muren, & Petersen, 2012; Kan, Leung, et al., 2013; Kan, Leung, & Yu, 2012; Kroon, Hol, & Essers, 2013; Lloyd & Ansbacher, 2013; Rana, 2014; Rana & Rogers, 2013; Stathakis, 2012). Bush et al (2011) validated Acuros XB against MC in multi-slab heterogeneous phantoms with low- and high-density heterogeneities. Calculated PDD and lateral profiles demonstrated superiority of Acuros XB over AAA. In this study, a maximum discrepancy of 4.5% compared to MC was observed near the air cavity interface. However, for most calculations, Acuros XB was within 2.9% of MC compared to 17.5% difference when using AAA.

A number of experimental dose measurements have been conducted in heterogeneous structures to validate modern TP dose algorithms (K. Bush et al., 2011; Han et al., 2013, 2011; Kan, Leung, et al., 2013; Kan et al., 2012; Kroon et al., 2013; Lloyd & Ansbacher, 2013; Rana & Rogers, 2013, 2013; Stathakis, 2012). The size of detectors and, especially, the thickness of its sensitive layer must be as small as possible, due to the steep dose gradient at the media interface. GafChromic films,(Bilge et al., 2009; Cheung et al., 2006) Metal Oxide Silicon Field Effect Transistor (MOSFET) and, partially, thermoluminescent dosimeters (TLD) detectors satisfy these criteria. Hoffmann et al. (2012) used Gafchromic films (EBT) in heterogeneous media (CIRS IMRT Thorax Phantom) and compared the measured doses with Acuros XB and AAA calculations. In that study, 22 different treatment plans were measured and calculated. The mean values of the percentage passing rate (3% / 3 mm criteria) were found to be 98.2% ± 1.1% and 99.5% ± 0.3% for Acuros XB using 6 and 15 MV energy beams, respectively, while a passing rate of 94.1% ± 7.0% and 96.1% ± 3.3% for the 6 and 15 MV energies, respectively, were observed for AAA. Kan *et al.*(2012) investigated the accuracy of Acuros XB near air/tissue interfaces using small fields (2 x 2–5 x 5 cm^2). PDDs calculated for the 2 x 2 cm^2 field were overestimated when compared to TLD measurements at the air/tissue interface by 41% and 6% for AAA and Acuros XB, respectively. In another paper, Kan *et al.*(2013) used Gafchromic EBT3 films and TLD to compare Acuros XB and AAA calculations against EBT3 and TLD measurements adjacent to air and bone inserts in a rectangular tissue phantom. The average dose difference (calculated data - measured data) for all the tested cases in this study were 4.3%. Another study by Carrasco et al.(2007) involved comparing five TP dose calculation algorithms against MC simulation, MOSFET and TLD measurements in multilayer slab phantom with cortical bone used as high-density heterogeneity. In that study, TLD measurements underestimated MC calculations by 5.7% ± 1.1% near the exit interface. Ding *et al*.(2007) found that AAA calculations near water–lung interfaces agree with MC calculation and MOSFET measurements for 6 and 18 MV photon beams within experimental and statistical uncertainties (1%–3%).

Kwan *et al*.(2008) validated a special design of MOSFET detector, known as MOS*kin* (CMRP, Wollongong, Australia), for surface measurements and found them to be within 2% compared to the Attix parallel plate ionization chamber. Qi *et al* (2009) used MOS*kin* to evaluate commercial TPS (Corvus 6.2) in calculating superficial dose and found that calculated dose overestimated MOS*kin* measurements by an average of 7.8%.

In this study, Gafchromic EBT2 film (Ashland, Specialty Ingredients, Wayne, NJ) and MOS*kin* detectors, as well as MC calculations, were used to estimate the dose near extreme media heterogeneities irradiated by 6 and 18 MV beams of different sizes. Water–air, water–steel, and water–lung interfaces were used, and the measured dose was compared to the MC calculations, as well as to the AAA and the Acuros XB predictions. This combination of experimental and MC methods allowed for testing accuracy of commercial algorithms and the evaluation of accuracy and consistency of "benchmarks" —experimental measurements and MC in extreme conditions.

4.1. Materials and Methods

4.1.1. Experimental setup

Three different phantoms with high/low density heterogeneities, as shown in Figure 4.1, were made (virtually and experimentally) to compare the performance of the five dosimetric techniques used in this study. The first phantom was a 30×30×30 cm^3 Solid Water slab that had an air cavity of 20×2.5×2.35 cm^3. This was created to imitate the water–air heterogeneity encountered in clinical situations, such as head and neck treatments. The second phantom had exactly the same geometry with a steel rod (ρ =7.8 g/cm^3) of 20×2.5×2.35 cm^3 size inserted to fill the air cavity. This phantom was used to measure the dose near a high-density heterogeneity and evaluate performance of the dose calculations. The third phantom was made with two 30×30×5 cm^3 slabs of solid water, two 30×30×5 cm^3 slabs of lung, and one 30×30×1 cm^3 slab of solid water stack, as shown Figure 4.1-c. This phantom was designed to simulate a lung tumor. For simplicity, those phantoms will be referred as water–air, water–steel, and water– lung phantoms, respectively. Phantom slabs used in this study were "Solid Water" RMI-457 (mass density ρ = 1.046 g/cm^3) and "Lung" LN300 RMI-455 (ρ = 0.3 g/cm^3).

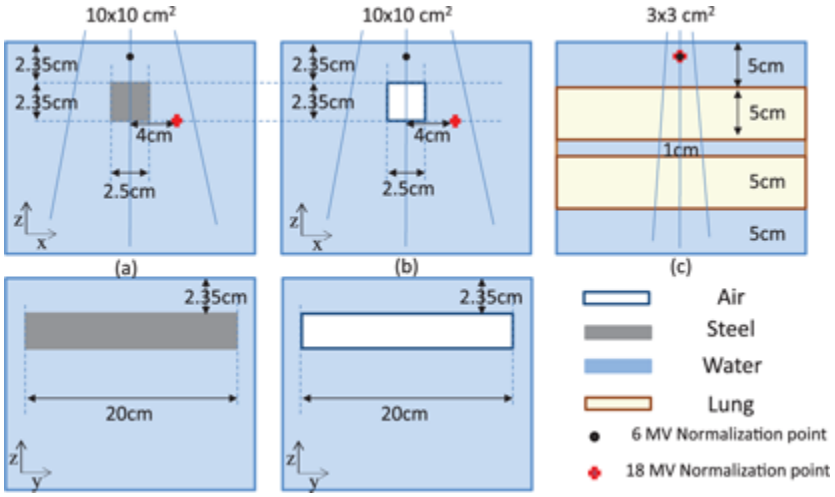

Figure 4.1: Diagrams of the three phantoms created to measure dose profiles: (a) shows geometry of the phantom with water-steel-water interface; (b) shows geometry of the phantom with water-air-water interface; and (c) shows geometry of the phantom with water-lung-water interface. Field sizes used for irradiating each phantom are also shown. Varian 21EX 6 and 18 MV were used in these measurements and calculations. Measured and calculated percent depth doses were normalized at the points shown in the diagram.

A Varian 21EX linac was used to expose the phantoms to 6 and 18 MV photons. The water–air and water–steel phantoms were irradiated by 10×10 cm^2 field beams at 100 cm SSD and the lung–water phantom was irradiated by a 3×3 cm^2 field at 89.5 cm SSD with the beam isocenter located at the center of a 1 cm water slab. Percent depth-dose (PDD) measurements were taken along the beam central axis using EBT2 films and the MOS*kin* detector with computerized reader was used to measure the dose at the water side of the interfaces. This will be described in detail in the following sections. The PDD was normalized at depth of maximum dose (d_{max}) for the 6 MV beam and at an off-axis point located 4 cm off the beam central axis and depth of 4.7 cm for the 18 MV beam. This point was chosen in a uniform dose region to avoid charged particle disequilibrium conditions. Normalization points are shown in Figure 4.1. Figure 4.2 shows labeling of the interfaces between different media in the three phantoms.

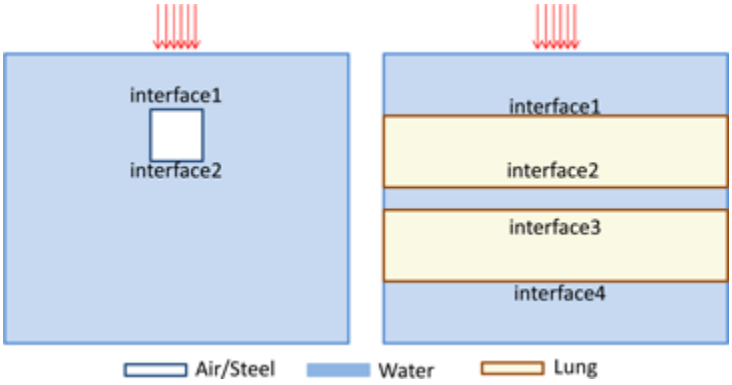

Figure 4.2: Diagram labeling the interfaces between the different mediums in (left) water–steel/air and (right) water–lung phantoms.

4.1.2. Monte Carlo calculations

Monte Carlo simulations were performed using the Vancouver Island Monte Carlo (VIMC) system (S. Zavgorodni, Bush, Locke, & Beckham, 2008; S. Zavgorodni et al., 2007). VIMC is a web-based platform that facilitates the use of BEAMnrc/DOSXYZnrc MC codes to simulate transport of photon or electron beams through a patient or phantom geometry. The 6 and 18 MV photon beams from Varian 21EX Clinac were used in this study. The accelerators were modelled according to the manufacturer specifications of the geometries. Photon (PCUT) and electron (ECUT) cutoff energies of 0.01 MeV and 0.700 MeV, respectively, were selected for all calculations. Pre-target electron source with monoenergetic electron energy of 6.0 MeV and 18.5 MeV were configured for the 6 MV and the 18 MV models, respectively. Incident electrons were defined as a symmetric Gaussian intensity distribution with full width half maximum (FWHM) of 0.75 and 1.3 mm energy for the 6 and 18 MeV respectively. The BEAMnrc models for 6 and 18 MV 21EX beams used in this work have been previously established and benchmarked (K. Bush et al., 2011; Karl Bush et al., 2009; Gagné & Zavgorodni, 2007; S. Zavgorodni et al., 2005; Sergei Zavgorodni, 2013). Statistical uncertainties for all calculations were less than 1% in all but the air-filled regions.

Customized phantoms were built through VIMC graphical user interface that is similar to DOSXYZnrc GUI. This interface allows building phantoms with exact geometrical boundaries avoiding voxelization artefacts commonly present in CT-based phantoms. The material densities for steel, air, water, and lung were matched to those used for AcurosXB in the Eclipse^{TM} TPS. Central axis PDDs, as well as lateral profiles were scored in 0.1 cm voxels. PDD scoring resolution was increased to 0.05 cm for the first three voxels directly above and immediately below each interface of the modelled phantoms.

4.1.3. AcurosXB and AAA calculations

AcurosXB, and AAA share the same multiple-source photon beam source model. It consists of primary photon source, extra-focal photon source, electron contamination source and photons scattered from wedges. Even though AcurosXB and AAA share the same multiple-source model, the model parameters are different due to the differences in the dose calculation (Fogliata, Nicolini, Clivio, Vanetti, Mancosu, et al., 2011; Tillikainen et al., 2007).

Open-field beam data, required in the configuration process, were acquired using an IC-15 (IBA dosimetry, Bartlett, TN) ionization chamber in a Wellhofer 48.0×48.0×48.0 cm^3 water tank. These measurements were taken during a departmental commissioning process for 21EX Varian linear accelerator (K. Bush et al., 2011).

In this study AAA version 10.0.28 was used. AcurosXB calculations were performed using two versions of this software 11.0.02 and 11.0.31, which will be referred to below as AXB1102 and AXB1131, respectively. New AcurosXB version (11.0.31) had several updates (Han et al., 2012). Amongst them were: reduced electron cutoff energies (from 500 KeV to 200 KeV); improved photon ray tracing and electron contaminant source; "transport correction" implemented to improve accuracy; re-sampling to the calculation grid was improved for the voxels that cross structure boundaries.

Three multi-slab heterogeneous phantoms described in previous sections and shown in Figure 4.1, have been created within Eclipse™ planning software, using contouring tools. The phantoms were created with the exact dimensions of the real phantoms. Material densities, matching those used in DOSXYZnrc, were assigned to the phantom structures manually. Densities of 0.0012 g/cm^3, 7.8 g/cm^3 and 0.3 g/cm^3 were assigned to air, steel, and lung structures, respectively. The calculations were scored in a 0.1 cm grid voxel size with the heterogeneity correction option turned on for all used algorithms (AAA, AXB1102, and AXB1131). PDDs were extracted throughout the beam central axis (CAX) using Eclipse™ tools. Lateral dose profiles were extracted from water-air and steel-water phantoms. These profiles run through the CAX in x-axis direction at the depth of 3.5 cm (through water-air and steel-water heterogeneities). AXB calculations, both versions, were reported in the dose to medium (D_m) mode. AAA calculations were performed and reported in the dose to water (D_w) mode– the only option available for this algorithm in Eclipse TPS. Dose within steel has not been discussed in this work, as it is irrelevant in clinical practice and AAA was not designed to calculate the dose in steel (unlike MC and AcurosXB).

4.1.4. GafChromic EBT2 film measurements

GafChromic EBT2 film was used in this study for its advantages when measuring doses at high-gradient regions, such as boundaries of heterogeneities where detector perturbation is a problem.

Film strips of 2 cm width were used to score the depth doses before and after the interfaces, by being placed vertically (Figure 4.3) along the beam axis. This way, PDD through the media interface is scored using either one piece of film strip in the case of the water-air phantom or two pieces of strips in the case of the water-steel phantom. In the water–lung phantom, four pieces were used: one strip before and after each interface. Effect of air gap at each side of the film strip is ignored in our measurements, and this was validated by comparing PDD measured using 2 cm strip of EBT2 stack between two water slabs against Eclipse (AAA) calculations. The differences between EBT2 and Eclipse beyond the d_{max} were within ±1%.

The dose measured within the air cavity has been converted to dose-to-medium by applying stopping power ratio factor, as proposed by Siebers *et al*. (2000). For the 18 MV beam, another piece of film was used at 4.0 cm of the central beam axis and at 4.7 cm depth, as illustrated in Figure 4.3.

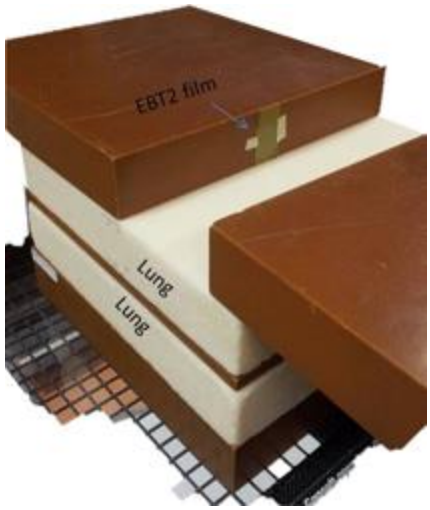

Figure 4.3: A photograph of the phantom used to measure PDD using Gafchromic EBT2 strips. A piece of film attached to the solid water slab along the beam central axis is shown.

The implemented film dosimetry protocol was as described in Chapter 3. The films were calibrated using the PDD calibration approach.

4.1.5. MOSkin™ measurements

The MO*Skin* detector, introduced in Chapter 1, was used in this study for its dosimetry capabilities at skin surface and interfaces (Hardcastle et al., 2010; Hardcastle, Soisson, Metcalfe, Rosenfeld, & Tomé, 2008; Kelly et al., 2011; Ian S. Kwan, 2009; I.S. Kwan et al., 2008; Qi et al., 2012, 2011, 2009; Quinn et al., 2011).

The MOS*kin* was placed in a 2 mm slab of solid water, which has been grooved specifically to accommodate the detector. The MOS*kin* was carefully leveled with slab surface when installed. All the measurements were done while the MOS*kin* sensitive layer was facing the beam ("face on" configuration). To account for sensitivity variation, before and during measurement sessions, the dosimeters were periodically calibrated against the reference field (Luo, Qi, Deng, & Rosenfeld, 2014). Each measurement point with MOS*kin* detector was repeated three times and results were averaged.

Near the interfaces, MOS*kin* PDD measurements were acquired in submillimeter depth increments using combinations of 100–400 μm thick sheets of water-equivalent plastic and 1 mm thick plastic water.

4.1.6. Relative performance of different dosimetry methods and difference calculations

The experimental and calculation methods, used in this study, are different and each of them has some strengths and weaknesses. Therefore, we do not claim one of the methods as the "gold standard".

MC method simulates particle transport through the medium by randomly sampling their interaction probabilities with medium within well-known physics principles. Thus, MC calculations are very reliable and accurate as long as used appropriately and the beam models are validated. In the literature, it has been used extensively as a dosimetric benchmark compared to alternative calculation algorithms and even against experimental measurements.

MOS*kin*, with its special packaging design, provides a very thin effective depth of measurement of 0.02 mm. It is a real-time dosimeter and has good characteristics linearity and decent reproducibility.(Hardcastle et al., 2010; Ian S. Kwan, 2009) MOS*kin* detector has always been used in its linear dose range by using current annealing technique (Alshaikh et al., 2014; Luo et al., 2014) for recovery of its initial threshold values after about 30 Gy accumulated dose that warrants its linearity. However, care needs to be taken to minimize measurement uncertainties, such as voltage creep-up effect that could introduce up to 2% error in a typical clinical dose of 2 Gy (Ramani, Russell, & O'Brien, 1997). Like many semiconductors, MOS*kin* exhibits temperature, energy, and angular response. The MOS*kin* temperature and creep-up effects were minimized by taking frequent reference measurements, and by keeping the time interval between irradiation and readout small and consistent.

Gafchromic EBT2 films are near tissue-equivalent with a very thin active layer of 0.03 mm. EBT2 film is 0.285 mm thick and has an effective measurement depth of 0.095–0.195 mm (depending on the film orientation relative to incoming beam). EBT2 was shown to have minimal energy and angular response (Arjomandy et al., 2010; Kairn et al., 2011). However,

they are not real-time dosimeters and it could take more than a day until readings are accessible. The film dosimetry protocol contains several stages where errors and uncertainties may originate. Therefore, a well-developed and consistent protocol needs to be used to minimize the errors.

Acuros XB and AAA are dose calculation algorithms optimized for fast dose calculations. Dose accuracy is, therefore, competing against short calculation time that is essential in clinical use. They share the linac head model with approximations that can impact the accuracy of dose calculations. AAA calculates the dose through convolution of photon fluence and energy deposition density function with scatter kernel that defines the lateral scattering in the phantom.(Gagné & Zavgorodni, 2007) AXB is based on solving LBTE and has been shown to produce accurate dose calculations, even in complex phantoms (K. Bush et al., 2011; Fogliata, Nicolini, Clivio, Vanetti, Mancosu, et al., 2011).

In this study, we have chosen MC calculations as a reference for the purpose of data presentation. All measurements were compared to MC, and the local differences were calculated by subtracting MC calculations from the other measurements/calculations:

$$\%\Delta_{D-MC} = (Dose_D - Dose_{MC}) \quad (4.1)$$

D stands for AAA, AXB, MO*Skin* or EBT2.

4.2. Results

4.2.1. PDDs and profiles in water-air phantom

The PDDs measured and calculated in the water-air phantom are shown in Figure 4.4 for 6 and 18 MV. Note that no MO*Skin* measurements were done in the build-up region, as these point-by point measurements were performed only near in-phantom interfaces.

For 6 MV photon energy, at the water-air interface AXB1102 dose calculations were in good agreement with MC, except in front of the water/air interface where AXB1102 predicted non-physical dose build-up of 4.4%. AXB1131 removed this build-up and agreed with MC calculations within 0.7%. EBT2, MO*Skin*, and AAA were all within 2% of MC calculations. At the secondary build-up, AXB1102 under-predicted the dose by over 10%, EBT2 measurements agreed with MC within 3.6%, and all other techniques were within 2-3% of MC. Beyond 0.2 cm from the air/water interface, the PDDs from both versions of AXB agreed with MC calculations within 1%. The average dose differences, $\%\Delta_{AXB-MC}$, in this region were 0.3% and 0.7% for AXB1131 and AXB1102, respectively.

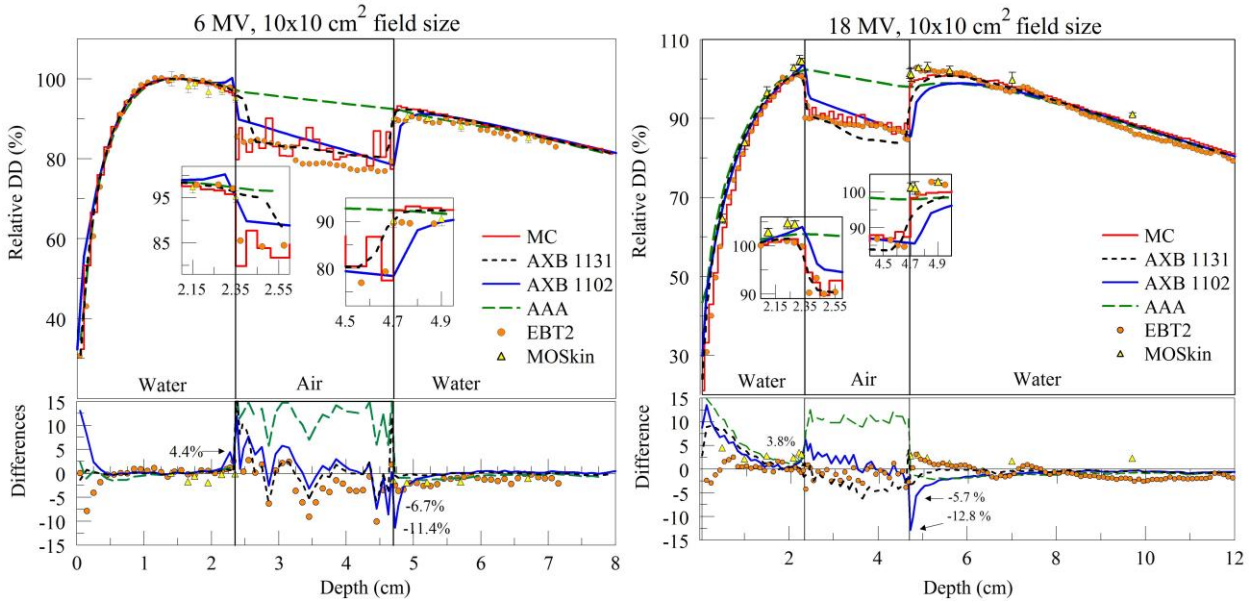

Figure 4.4: PDDs in the water-air phantom 6 MV (left) and the 18 MV (right) photon beams. Notice that inset plots have different vertical scaling.

For 18 MV photon energy, AXB1131, AXB1102, and AAA over-predicted MC dose in the first centimeter of the build-up region by up to 9.1%, 13.5%, and 22.3%, respectively (Figure 4.4, right). Meanwhile, MO*Skin* and EBT2 measurements were in agreement with MC calculations within 3.5 - 4.5% and -2.9 - 2.6%, respectively. In the second build-up region, AXB1131 and AXB1102 calculations differed from Monte Carlo by up to ~3.6% and 12.8%, respectively. However, beyond 2 mm from the distal interface, differences lowered to 1.2% and 4.4% for AXB1131 and AXB1102, respectively; MO*Skin* and EBT2 measurements agreed with MC within ~3.0%.

Figure. 4.5 presents calculated lateral profiles taken through the centre of the air gap. For both beam energies, the dose values predicted in water by AAA, AXB1102, and AXB1131 were in good agreement with MC calculations everywhere, except penumbra and interfaces.

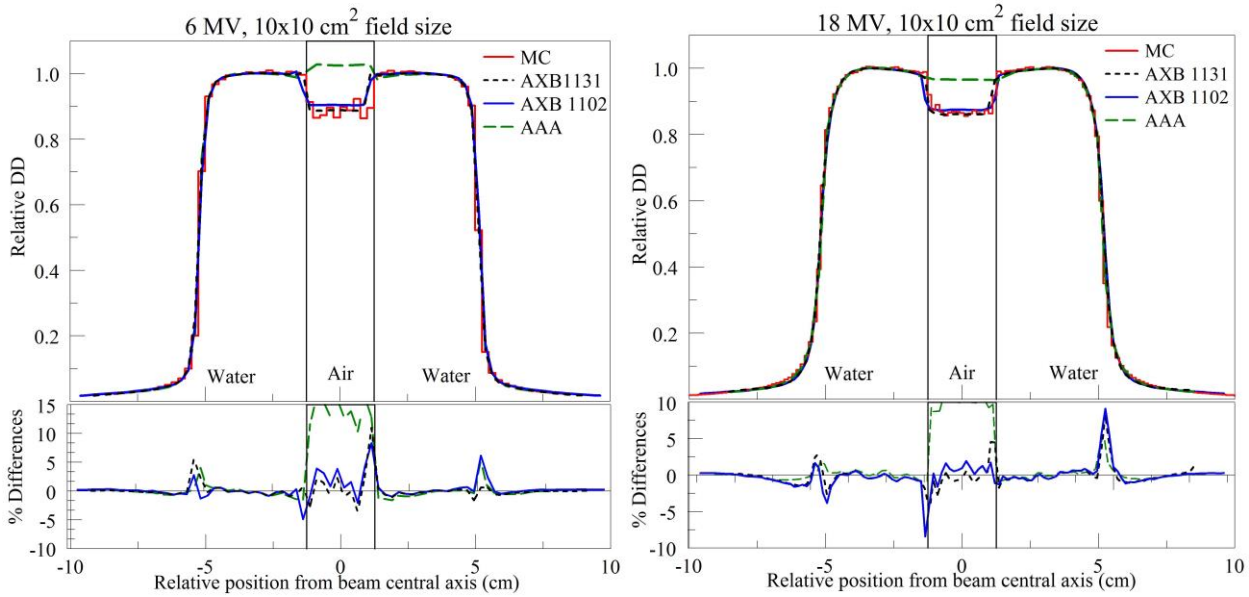

Figure 4.5: Lateral profiles through the center of the rectangular air cavity for 6 MV (left) and 18 MV (right) beams.

4.2.2. PDDs and profiles in water-steel phantom

The relative depth doses measured and calculated in the water-steel phantom for 6 and 18 MV beam energies are presented in Figure 4.6.

For the 6 MV beam, all calculations and measurements were in good agreement, except AAA, which failed to predict the back scatter from the high-density heterogeneity and underestimated the dose by 25.5% compared to MC, in front of the steel/water interface. Notice in the voxel adjacent to the water/steel interface, differences of up to -15.9 % and -17.3% were observed for AXB1131 and AXB1102, respectively. Meanwhile, MO*Skin* and EBT2 differed from MC calculations by up to -4.4% and -3.8%, respectively. At the distal (steel/water) interface, AXB1131, AXB1102, and AAA calculations differed to MC by up to 2.8%, 1.8%, and 6.2 %, respectively. Beyond 0.2 cm from the distal interface, AXB1131 and AAA calculations agreed with MC within ~1.5%, and AXB1102 agreed within ~2.5%. At the same interface, MO*Skin* differed from MC by up to -3.9% directly on interface, whereas the EBT2 measurement agreed with the MC calculation within 1.7%.

For the 18 MV beam, in the build-up region of the water-steel phantom, agreement of measured and calculated doses was under 5% for the most part, with slightly higher differences in the first centimeter from the surface. Good agreement, within 2.0% between measurements and calculations, was found in the proximity of water/steel interface, with the exception of AAA calculations that again did not accurately model backscatter from steel and underestimated the

dose by 28.9% in the immediate proximity of the interface. The dose calculated by AXB1131 and AXB1102 in the voxels immediately adjacent to the interface differed from MC by -11.2% and -6.8%, respectively. In the same region, EBT2 measurement was within ~ 2.0% and MO*Skin* differed from MC by 4.8%. Immediately beyond to the steel/water interface, AXB1131, AXB1102, and AAA underestimated MC calculated doses by 4.6%, 4.0%, and 3.5%, respectively, and their doses in the PDD tail region differed from MC by -1.2%, -2.5%, and 5%, respectively. MO*Skin* and EBT2 measurements at the interface and in the PDD tail region were within 0.5 - 3.3% and 1.5 - 3.0%, respectively, compared to MC calculations.

Figure 4.7 shows the lateral profiles extracted through the centre of the steel insert along the x-axis (see Figure 4.1-a) for MC, AXB(1102 and 1131), and AAA. Lateral dose enhancement was predicted by MC and both versions of AXB near the interfaces. Both versions of AXB calculations were in agreement with MC calculations within ~2.0%, except penumbra regions. AAA, however, underestimated the dose near the interfaces by 4.5 - 12.4% and 5.5 - 19.0%, respectively, for the 6 MV and 18 MV beams.

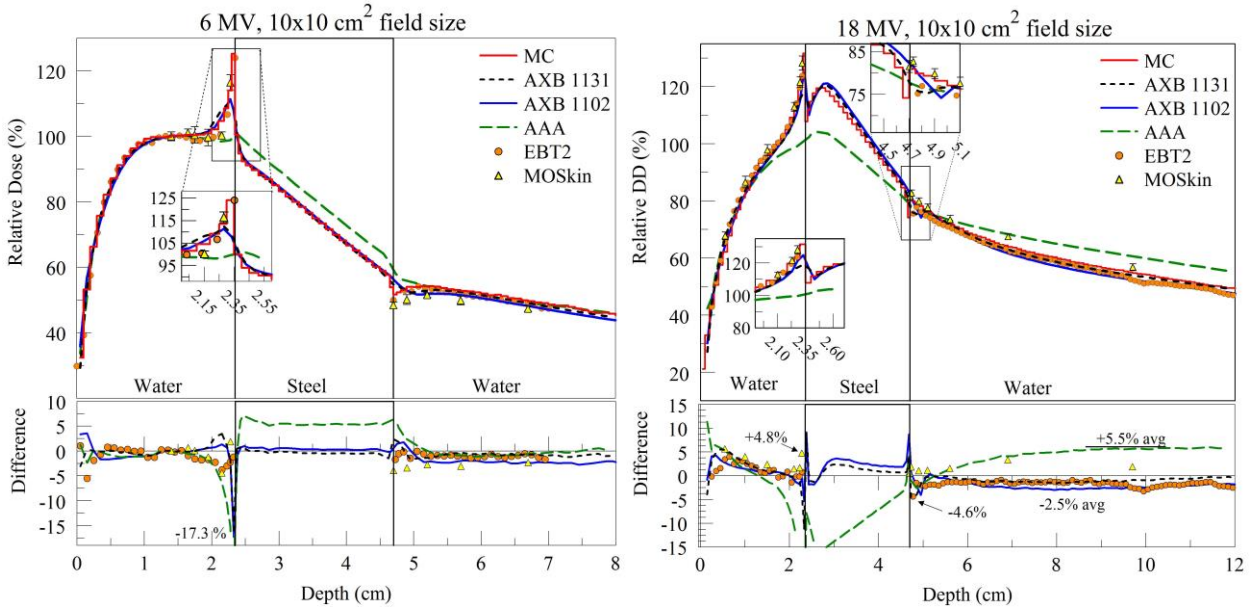

Figure 4.6: PDDs in the water-steel phantom using 6 MV photon beam (left) and the 18 MV photon beam(right). Notice that inset plots have different vertical scaling.

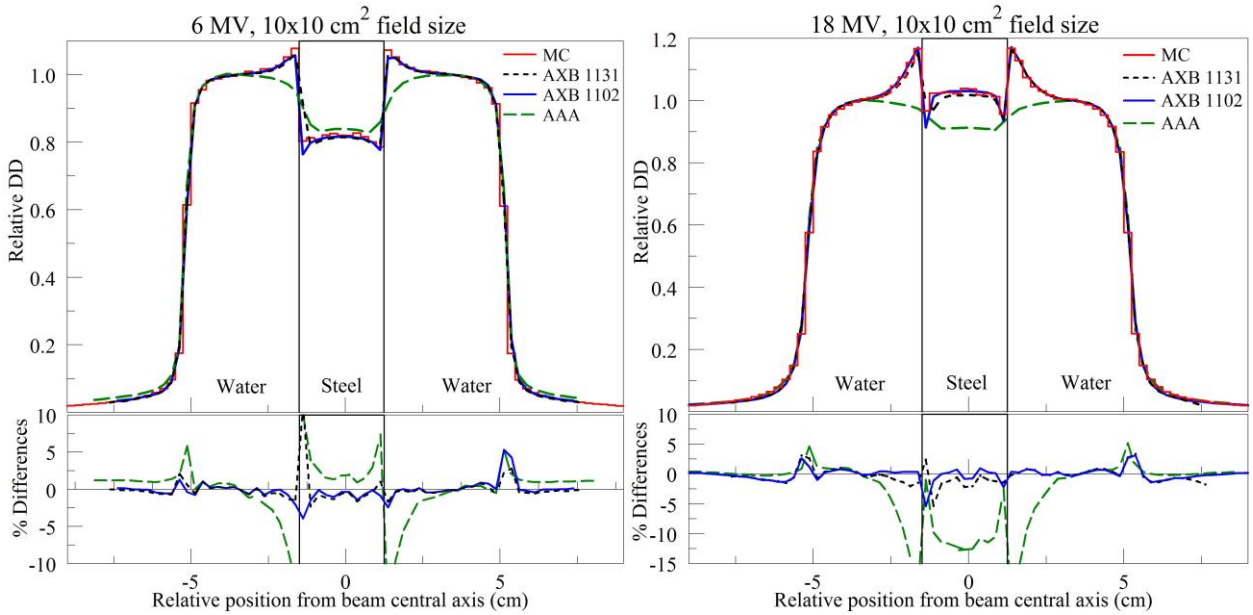

Figure 4.7: Lateral profiles through the center of the rectangular steel insert for 6 MV (left) and the 18 MV(right) beams.

4.2.3. PDDs in Lung-water phantom

PDDs for the 6 MV beam are shown in Figure 4.8 (left) in the water–lung phantom. Except for the first half centimeter of the buildup region, all calculations and measurements were in agreement within 3%. All TPS algorithms were in agreement with MC within 2%. Maximum differences of 2.5% between EBT2 measurements and MC were observed in both lung–water secondary buildup regions. MO*Skin* measurements in these regions were up to 2.9% lower than MC, with the greatest differences being right at the interface. Given MC statistical uncertainty of 1% and experimental uncertainties of over 1.5% (± 1.5% for EBT2 and ± 2.5% for MO*Skin*), MC and measurements agreed within their combined uncertainties. Lower values of MO*Skin* directly on secondary buildup interfaces (interface 2 and 4) are partially due to much higher spatial resolution of the MO*Skin* (sensitive volume thickness is less than 1 micron and close to the interface as close as 0.02 mm) in comparison to Monte Carlo simulations (voxel size is 0.05–0.1 cm) and water-equivalent depth of measurements 0.02 mm for used MO*Skin*. The same tendency for MO*Skin* measurements can be seen on water–lung interfaces in the build-down region, where, like on the lung–water interface, dose gradient is very steep.

PDDs for the 18 MV beam are shown in Figure 4.8 (right). For the most part, MO*Skin*, EBT2 measurements, and MC calculations agreed within ~ 2%. An exception was MO*Skin* measurement versus MC calculation points that were right at the lung–water interfaces. The maximum difference relative to MC was -3.1%, which is explained above. There were also few

EBT2 dose points (at the depth of ~ 2 cm) where the difference exceeded 2%. However, these differences can be attributed to “noise” due to film/scanner non-uniformities that remained in the data, despite the film processing described in Chapter 3.

Differences between TPS calculation algorithms and MC were larger for 18 MV compared to 6 MV. Maximum differences were observed in the buildup region, as well as lung slabs. In the upper-lung slab, AAA, AXB1102, and AXB1131 overestimated MC dose by up to 6.8%, 3.2%, and 2.8%, respectively. In the second lung slab, both AXB versions were within 2% from MC, whereas AAA overestimated MC dose by 3%. At the second lung–water interface, agreement between all dosimetric techniques, except AXB1102, was within less than 2%. AXB1102 showed a discrepancy of -2.8% within the first half-centimeter of the secondary buildup.

Tables 4.1 and 4.2 show a summary of relative doses measured by EBT2 and MO*Skin* near interfaces. In general, differences between the two dosimeters were within ± 4%, except at the water–steel interfaces in 18 MV beam, where difference of -4.6% and -7.1% were measured.

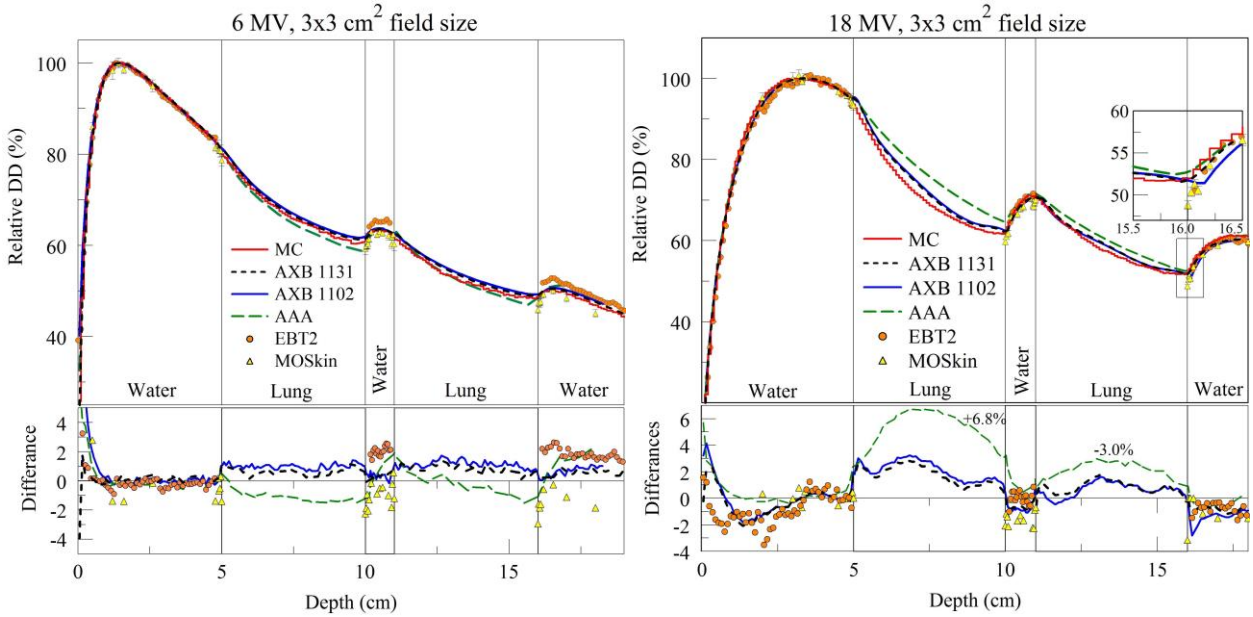

Figure 4. 8: PDDs in the lung-water phantom using 6 MV (left) and the 18 MV (right) photon beams. Notice that inset plots have different vertical scaling.

These differences are attributed to the different depths of effective measurement point, combined with experimental uncertainties for the two dosimeters

Table 4.1: PDD dose-point comparisons between EBT2 and MOS*kin* at the interfaces of water–air, water–steel, and water–lung phantoms for the 6 MV case.

		EBT2	**MOS*kin***	$\%\Delta_{EBT2-MOSkin}$
Water–air	Interface 1	97.8%	95.3%	2.5%
	Interface 2	89.9%	90.3%	-0.4%
Water–steel	Interface 1	112.7%	116.4%	-3.7%
	Interface 2	50.0%	48.4%	1.6%
Water–lung	Interface 1	84.7%	82.1%	2.6%
	Interface 2	64.3%	62.9%	1.4%
	Interface 3	65.2%	62.1%	3.1%
	Interface 4	51.8%	49.2%	2.6%

Table 4.2: PDD dose-point comparisons between EBT2 and MOS*kin* at the interfaces of water–air, water–steel, and water–lung phantoms for the 18 MV case.

		EBT2	**MOS*kin***	$\%\Delta_{EBT2-MOSkin}$
Water–air	Interface 1	100.7%	104.5%	-3.8%
	Interface 2	99.5%	101.2%	-1.7%
Water–steel	Interface 1	123.7%	128.3%	-4.6%
	Interface 2	75.6%	82.7%	-7.1%
Water–lung	Interface 1	93.6%	94.2%	-0.6%
	Interface 2	63.5%	61.8%	1.7%
	Interface 3	65.2%	62.1%	3.1%
	Interface 4	71.7%	68.5%	3.2%

4.3. Discussion

In this chapter, five dosimetric techniques that include EBT2 and MOS*kin* detectors, as well as MC and Eclipse TPS (AAA and two versions of AcurosXB) calculations have been used to measure and calculate dose profiles in three multi-layer heterogeneous phantoms with water/air, water/lung, and water/steel interfaces. This combination of experimental and calculation dosimetry techniques has been used for the first time to evaluate the dose near these interfaces. The study assessed the dose from different dosimeters in non-equilibrium regions near low- and

high- density heterogeneities. Larger differences were found among all the dosimeters at the interfaces and the build-up regions. This is where the differences in properties of the dosimeters are highlighted by the steep dose gradients. In the following sections, results of each phantom are discussed separately.

4.3.1. Water-air phantom

In this study, we found that at water/air and air/water interfaces MC and AXB1131 calculations were closer to experimental measurements (EBT2 and MO*Skin*) than AAA and AXB1121 for both energies. For both energies, maximum differences between all dosimetric techniques and MC calculations were observed in the secondary build-up region where AXB1102 underestimated MC calculations by 5.7 to 12.8%, while AXB1131 only underestimated it by 3.6%. Other studies (K. Bush et al., 2011; Kan et al., 2012; Stathakis, 2012) observed similar differences at interfaces between older AXB releases and a benchmark. Bush *et. al* (2011) observed a difference up to 4.5%, just beyond 10 cm air-gap, between AXB (10.0.02) and MC for a 6 MV beam. This study excluded the first voxel after the air gap where the differences were higher. Kan *et. al* (2012) reported the difference of 7.3% between AXB (10.0.28) and TLD measurement at the distal air/water interface, for a 5×5 cm^2 6 MV beam. Stathkis *et. al* (2012) reported differences of 3%-15% between AXB (10.0) and MC in PDD after air heterogeneity using 6 MV beam. However, all the mentioned studies used older versions than the then current version used in this study, which has been confirmed to be an improvement. For the first time in this study, a comparison involves an earlier version of AXB (11.0.21) with an updated clinical release (11.0.31).

4.3.2. Water-steel phantom

For the water-steel phantom, our results showed that all methods were in reasonable agreement as compared to MC calculations, except close to the steel insert. Lloyd *et al* (2013) done similar work using AXB (11.0.02), but did not provide film measurement before/after the high density insert of the 6 MV beam. Another study by Ojala *et al* (2014) involved comparison of AXB (10.0.28), MC, IBA SFD, farmer IC, and EBT3. However, this study did not include 18 MV beam energy, and experimental measurements were only taken after the high-Z insert in their study.

Our findings were consistent with previous investigations that included AAA and AXB comparison in high- density heterogeneities, such as bone, stainless steel, and titanium alloy, in which AXB proved to be superior than AAA (K. Bush et al., 2011; Han et al., 2011; Lloyd & Ansbacher, 2013; Ojala et al., 2014). Our results showed that AAA differed to MC by an average of ~5.5 %, after the rectangular steel insert. This is due to inaccurate modeling of beam attenuation in the high-density heterogeneity within the water-steel phantom. This is consistent

to Lloyd *et. al* (2013) study, where similar overestimation by AAA was observed after rectangular steel insert.

Our transverse dose profiles and PDDs for the water-steel phantom showed that AAA was not accurate in predicting lateral and back scatter radiation from high density heterogeneities. This is comparable to the findings by Lloyd *et. al* (2013) where similar underestimation of calculated dose by AAA was observed near (steel/water) interface. AXB (1131 and 1102), on the other hand, predicted the backscatter behavior and its calculations were in a good agreement with MC and EBT2 measurement at the water/steel interfaces. However, unlike Lloyd *et. al* (2013), our results showed differences (excluding voxels adjacent to the interfaces) of -1.6% to -5.5%, between AXB and MC at the water/steel interfaces. This might be attributed to the location of the steel-insert being within the 18 MV build-up regions, at 2.35-4.7 cm depth, which makes calculations more challenging. Differences were even higher in the voxels directly adjacent to the interfaces (-6.8% to -17.3%). This could be attributed to the Eclipse™ built-in intra-voxel interpolation feature and phantom voxelization. Interpolated points within voxels bordering different materials provide inaccurate "interpolated" dose. Vassiliev *et al*. (2010) compared calculated dose distribution from AcurosXB and MC on a point-to-point basis making sure that the matrices coincide in the spatial domain. In this study, we were interested to test AXB and AAA within the TPS package, using tools available to evaluate and compare dose profiles.

Our results showed that EBT2 and MO*Skin* measurements were in good agreement with MC calculations at the water/steel interfaces for both sets of energy. Maximum difference of ~4.8% between experimental measurement and MC can be seen within 0.2 cm of both water/steel and steel/water interfaces. The disagreement between MC and the experimental detectors could be attributed to volume averaging, due to MC scoring voxel size as compared to the smaller detection volume in MO*Skin* and EBT2.

4.3.3. Water-lung phantom

Results for the PDD of the 6 and 18 MV beams in water-lung phantom, Figure 4.8, showed that all experimental and calculation dosimetric methods, except AAA, were within ~3% everywhere, except in the build-up and interfaces regions.

Our results, in Figure 4.8, showed that AXB (1131 and 1102) were in a better agreement with MC calculation than AAA, within 2.8-3.2% throughout the phantom for both energies. This is comparable to previous studies (K. Bush et al., 2011; Vassiliev et al., 2010). Vassiliev *et al*. (2010) reported 2.3% maximum difference between AXB and MC within lung in multilayer phantom (water-bone-lung-water) using 2.5×2.5 cm^2 18 MV field. Bush *et al*.(2011) found that

AXB was in agreement with BEAM/DOSXYZnrc to within ± 3.0% of the maximum dose within lung (0.24 g/cm^3) using 18 MV 4×4 cm^2 beam incident on water-lung-water phantom.

AAA calculations differed to MC by up to 6.8% within the lung for the 18 MV beam. Such large differences of AAA, compared to benchmark, were also reported in previous studies. Han *et al.* (2011) reported 17.6% as maximum relative difference between AAA and EGSnrc when using a 2.5×2.5 cm^2 18 MV field in lung-slab of a multi-layer slab phantom (tissue-bone-lung-tissue). Bush *et al*.(2011) reported that AAA underestimated BEAM/DOSXYZnrc by 8% within lung (0.24 g cm^{-1}) using 18 MV 4 x 4 cm^2 beam incident on water-lung-water phantom. Ding *et al* (2007) reported a 6.0% difference between MC and AAA in lung using a (3×3 cm^2, 10 MV) single beam. The variations in differences between our findings and the aforementioned studies originate from the different lung density (0.3 g/cm^3), phantom structure and beam configuration used in our study.

For the 6 MV, MO*Skin* measurements were up to 2.3% lower than MC at the upper water-lung interface (interface 2) and 2.9% lower at the last lung-water interface (interface 3). This is still an acceptable agreement considering MC statistical uncertainty (~1%) and MO*Skin* measurement uncertainty (~2.5%). Similar agreements of MOS*kin* with EBT2 film and MC were observed for 18 MV beam as well. This is consistent with the results reported by Ding *et al* (2007) who used MOSFET along with MC (BEAMnrc/DOSXYZnrc) to validate AAA dose in water/lung phantom.

For both energies, EBT2 measurements were in agreement with MC calculations to within 3.0%, which support our MC model to produce accurate calculations in the tested phantoms.

4.4. Conclusions

Our study showed that all dosimetric techniques, except AAA, were in good agreement (~3%) for both photon fields used in the three phantoms for this study, except in the build-up regions and interfaces where differences were more pronounced. Also, relatively large differences (3% - 6.8%) between AAA and AXB or MC in lung were observed when using higher energy (18 MV) and that is due to the differences in their dose reporting modes.

Dose differences among the dosimetric techniques were larger for the 18 MV as compared to the 6 MV photon beam. The location of the air-gap and the steel insert, within the build-up region of the 18 MV beam, introduced extra dosimetric challenge, resulting in greater differences at 0.2 – 1 cm depth.

The latest version of AXB (11.0.31) showed improved agreement with MC and measurements compared to the previous version (11.0.02). Maximum differences between TP

algorithms and MC were found near air/steel air/water interfaces. Differences between phantom voxelization methods used by AXB (Eclipse) and MC calculations highlighted the discrepancies near interfaces. While phantoms used in MC were produced with exact boundaries between the interfaces, Eclipse phantom voxelization process introduced an artifact between low-/high-density heterogeneities, which reduced the accuracy of TP dose calculations.

MO*Skin* and EBT2 measurements were in good agreement with MC calculations, except at the interfaces with steep dose gradient, where differences were larger. This was due to the fact that both detectors have small detection thickness and could measure the dose very close to an interface. Dosimeter type and thickness of dosimetric sensitive volume are critical in those regions, in which very thin and tissue equivalent dosimeters provide more accurate dose assessment.

AAA did not predict the backscatter dose in front of the high-density heterogeneity (steel), which resulted in a significant underestimation of the calculated dose in this region. AAA was shown to produce incorrect calculations downstream of the high-density heterogeneity (steel), due to the inaccurate modeling of the attenuation within the steel insert.

Chapter 5

The work of this chapter was published as a technical note in the *Physics in Medicine & Biology* (Alhakeem and Zavgorodni 2018).

AUTHOR'S CONTRIBUTION TO THE PUBLISHED PAPER

Contribution to the paper in this Chapter are:

Eyad A. Alhakeem, (Candidate)

Wrote the first draft of the manuscript and contributed to subsequent revisions, contributed in the study design, and performed the calculation work. Analyzed and contributed in the data interpretation.

Sergei F. Zavgorodni

Contributed to manuscript, the study design, and the data interpretation.

5. Evaluation of latent variances in Monte Carlo dose calculations with Varian TrueBeam photon phase-spaces used as a particle source

Monte Carlo simulation of a radiotherapy beam is often carried out as a two-stage process. The first stage involves modeling the invariable, plan-independent upper part of a radiotherapy linear accelerator (linac) head. Particles simulated at this stage are then scored into a phase-space located at a pre-defined surface in the head model. The phase-space file (PSF) contains particle fluence information (coordinates, directional cosines, energy, type of particle) of the modeled

beam. At the second stage, the PSF is used as a particle source and MC transport code(s) propagate the particles through plan-dependent part of the linac head into a phantom.

In order for a PSF to allow accurate dose calculations in the phantom, it has to reflect particle fluence of the real radiation beam. This can be achieved by thoroughly modeling parameters of the initial electron beam that hits the target as well as beam-shaping components of the linac head. In the past, Varian allowed access to schematics of their linacs to facilitate modeling of particle transport for the dose calculations. This provided a gateway for modeling the linac head and generating phase spaces with as many particles as required. For the TrueBeam linac, Varian did not release the treatment head schematics; instead they provided PSFs, containing about 50×10^6 particles each, to be used in Monte Carlo calculations. These version 1 PSFs were scored on a curved surface above the jaws and contained 2–4 GB of data. Varian later released version 2 of the TrueBeam PSFs. Version 2 phase-spaces were further tuned to obtain better agreement with representative set of 'golden beam data' measurements, and they were scored on a flat surface. The version 2 library contains fifty files of ~1 GB size per photon energy. It has been long established that variance in the MC calculated dose is inversely proportional to the particle density in the fluence incident on a phantom (Mackie 1996). This is because the variance of a scored quantity is inversely proportional to the number of contributions to this quantity from particle interactions. Through use of variance reduction techniques, such as particle recycling or splitting downstream from the phase-space, the number of contributions can be artificially increased to reduce the variance (Walters et al 2002). However, Sempau et al (2001) showed that regardless of variance reduction techniques used in the PSF particles' transport through a phantom the variance of a calculated quantity cannot be reduced below a certain limit. This smallest possible value of the variance was named the latent variance (LV). Sempau et al (2001) also proposed a technique for determining the value of LV. LV therefore limits the accuracy achievable in MC dose calculations that use PSFs as a particle source, and in order to reduce LV larger PSFs have to be used to increase particle density. Still, very large PSFs are awkward to use as they take large amounts of storage space and prone to errors when transported through networks. On the other hand, if the LV of these phase-spaces has not been quantified, there is no guide on how many of the PSFs need to be used to achieve required accuracy. In fact, some applications are likely to require summing up more PSFs than others. This would depend on the energy of the beam, field size, and the required dose grid resolution. Cronholm and Behrens (2013) in a conference abstract reported evaluation of latent uncertainties for version 1 Varian TrueBeam 6 MV-FFF, 6 MV, 10 MV-FFF and 10 MV PSFs and 10×10 cm^2 fields. However, this abstract did not provide the details of their study nor explore the effect of depth, field size and voxel size on latent uncertainties in the calculated dose.

This chapter provides an evaluation of the latent variances for version 2 of Varian TrueBeam photon PSFs. Latent variances were evaluated at different depths in a phantom for various beam

energies and phantom grid resolution. Standard 10 × 10 cm^2 fields as well as small and very small fields (down to 0.13 cm diameter) were included. In addition, estimation of the number of 6 MV PSFs, or particles, required to achieve sub-percent latent uncertainty is provided for various field sizes.

5.1. Methods and Materials

5.1.1. Phase-space files for the Varian TrueBeam linacs

The Varian research team generated TrueBeam PSFs by modeling particle transport through the linac treatment head (Constantin et al 2011) with Monte Carlo GEANT4 (Agostinelli et al 2003) code. They used computer aided design schematics of the linac head and integrated these schematics into GEANT4 geometry modules. Simulated particles were scored between the primary collimator and the upper jaws in an International Atomic Energy Agency (IAEA) PSF format (Capote et al 2006). Fifty PSFs per beam energy were generated for the version 2 phase-space library and each PSF contains about 50 million particles producing a binary file of about 1 GB size. This required the numbers of electrons incident on the target (*Ni*) to be in the range of 3×10^8–9×10^8 (as shown in Table 5.1) depending on the beam energy.

5.1.2. Evaluation of latent variance

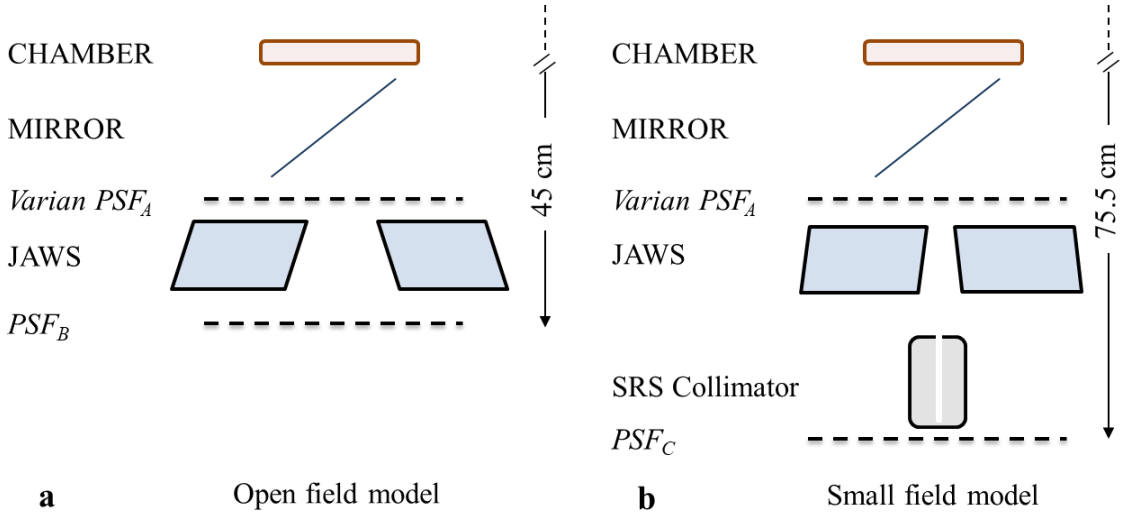

Figure 5.1**:** Diagram illustrating BEAMnrc models used in this study. Shown are Varian PSF (PSF_A), and a) the PSF_B scored under secondary collimator; b) the PSF_C scored under the SRS collimator.

BEAMnrc code was used to model open 10×10 cm^2 fields and fields collimated by BrainLab

(BrainLAB AG, Feldkirchen, Germany) circular stereotactic collimator (1 cm) as well as three smaller in-house customized collimators (0.13, 0.25 and 0.35 cm) as shown in Figure 5.1. For these fields latent variances of Varian TrueBeam PSFs were evaluated using technique similar to that proposed by Sempau *et al* (2001).

Sempau *et al* (2001) evaluated latent uncertainty of a small PSF by using the following technique. They ran a few simulations transporting particles from the PSF into a phantom with various particle splitting factors K and then plotted the variance of the scored quantity against 1/K. From the linear relation between the variance and K^{-1}, latent variance σ_k^2 was obtained as the linear-fit intercept at $K^{-1}=0$. To obtain the latent variance of a typical PSF, σ_k^2 was scaled down by the ratio of particles in the small and typical PSFs.

In our study one of Varian PSFs (PSF_A) was transported through the collimators and additional PSFs (PSF_B and PSF_C) were scored as shown in Figure 5.1. These ancillary phase-spaces contained a small number of particles and required a short simulation time. We therefore initially evaluated latent variances of PSF_B and PSF_C using the technique by Sempau *et al* (2001) and then scaled these variances to obtain the LV of PSF_A as detailed below. The number of particles in PSF_B and PSF_C varied depending on the field size and are shown in Table 5.1. Procedures for evaluating PSF_B and PSF_C are identical, therefore only that for PSF_B is described.

Table 5.1: A summary of the information for Varian PSFs investigated in this work. Where, N_i^A is the number of electrons incident on the target to create PSF_A, N_{PSA} is total number of particles in one full PSF_A, N_i^B(or N_i^C) is the number of electrons incident on the target to create PSF_B (or PSFc); and N_{PSF_B} (orN_{PSF_C}) is the total number of particles in PSF_B (or PSFc).

	Beam energy/Field size	N_i^A	N_{PSF_A}	N_i^B, N_i^C	N_{PSF_B}, N_{PSF_C}
Open fields	6 MV/10x10 cm^2	9.0×10^8	~ 46×10^6	9.7×10^7	255,298
	6 MV-FFF/10x10 cm^2	6.5×10^8	~ 47×10^6	3.2×10^7	202,433
	10 MV/10x10 cm^2	5.2×10^8	~ 49×10^6	4.69×10^7	210,159
	10 MV-FFF/10x10 cm^2	3.24×10^8	~ 45×10^6	1.62×10^7	240,340
	15 MV/10x10 cm^2	6.0×10^8	~ 48×10^6	5.53×10^7	224,274
Small SRS fields	6 MV/Cone 1.0 cm	9.0×10^8	~ 46×10^6	9.0×10^8	17,639
	6 MV/Cone 0.35 cm	9.0×10^8	~ 46×10^6	9.0×10^8	5,338
	6 MV/Cone 0.25 cm	9.0×10^8	~ 46×10^6	9.0×10^8	6,751
	6 MV/Cone 0.13 cm	9.0×10^8	~ 46×10^6	9.0×10^8	3,780

DOSXYZnrc code was used to transport PSF_B into a phantom and score the dose and its variance. MC simulations were then repeated with an increased number of particle recycling (N_{recycl}). The value of dose variance in a voxel located at the beam Central Axis (CAX) was calculated from each simulation, and latent variance (LV_B) was obtained by extrapolating the variances to an infinite recycling number (*1/N_{recycl}* equal to zero) as seen in LV evaluation plots (Figure 5.2).

The LV of a PSF is inversely proportional to the number of particles it contains as $LV\ \alpha\ 1/N_{PSF}$. Therefore, in order to evaluate the latent variance LV_A of a full PSF_A, the latent variance values, LV_B were scaled to the number of electrons incident on the target (shown in Table 5.1), that have been used to generate a single PSF_A as:

$$LV_A = \frac{N_i^B}{N_i^A} \times LV_B \qquad (5.1)$$

Where N_i^A: the number of electrons incident on the target to create a full Varian PSF_A

N_i^B : the number of electrons incident on the target to create PSF_B

LV_B: calculated latent variance of PSF_B.

Using equation (5.1) and the calculated latent variances of Varian PSFs (LV_A) for different beam energies, expressed in percent, total number of particles in a phase-space to achieve latent variance of 1% ($N_{PSF}^{1\%}$) can be calculated as:

$$N_{PSF}^{1\%} = N_{PSF_A} \times \frac{LV_A}{1\%} \qquad (5.2)$$

Then the number of phase-spaces M required to be summed to achieve a 1% latent variance can be written as $\frac{N_{PSF}^{1\%}}{N_{PSF_A}}$, and from equation 5.2:

$$M = LV_A(\%) \qquad (5.3)$$

Therefore, the number of phase spaces that needs to be summed to produce a single phase-space with *LV*=1% is simply equal to the value of LV_A, expressed in percent.

In all considered cases, latent variances were evaluated in voxels at the beam CAX. For 10x10 cm^2 6 MV-FFF, 6 MV, 10 MV-FFF, 10 MV and 15 MV beams LVs were evaluated at depths ranging from 0.25 cm to 15 cm in water phantom with 0.5x0.5x0.5 cm^3 voxels. For small 0.13 cm, 0.25 cm, 0.35 cm, and 1.0 cm diameter 6 MV beams latent variances were evaluated in 0.1x0.1x0.5 cm^3 voxels. In addition, latent variances in voxels of 0.02x0.02x0.5 cm^3, 0.05x0.05x0.5 cm^3 and 0.1x0.1x0.5 cm^3 were evaluated for the 0.25 cm diameter SRS cone. Latent variances in this case were determined at 1.5 cm depth for all voxel sizes, as for small

SRS fields LV was found to be minimal at this depth. Voxel sizes were chosen to provide sufficient resolution for calculation of the beam profiles and output factors in each considered case.

Evaluation of uncertainties in this study only includes statistical uncertainty (known as type-A uncertainty (BIPM, IFCC, ISO, & IUPAP, 2008)) in the calculated dose. Other possible uncertainties that arise from inaccuracies in linac model geometry, approximations built into MC particle interaction models, and cross sections known as type B (BIPM et al., 2008) uncertainties were not considered in this work (P Andreo & Fransson, 1989).

5.2. Results

The LV evaluation plots for different energies are shown in Figure 5.2, and the LV values as determined at different depths in a water phantom are shown in Table 5.2.

Such LV behaviour with beam energy, phantom depth as well as calculation voxel size is due to the density of primary MC particles travelling through phantom voxels. In detail this is considered in Discussion section.

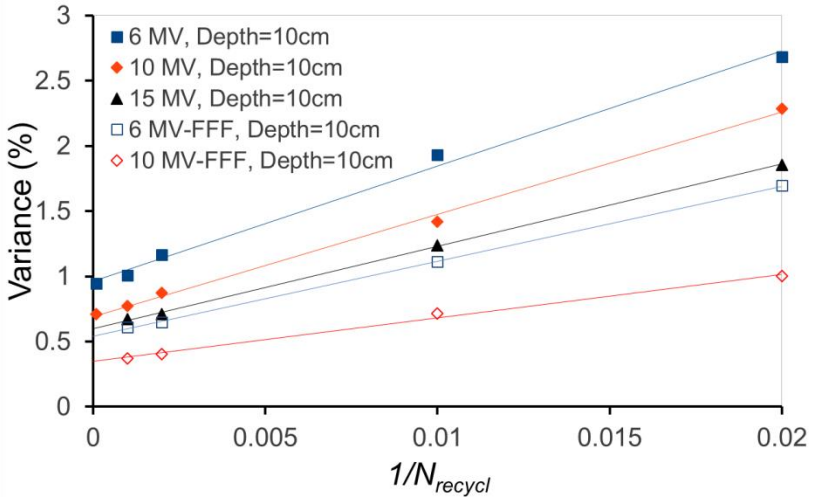

Figure 5. 2: Latent variance (LV_B) evaluation plots (dose variance vs $1/N_{recyl}$) for 6 MV-FFF, 6 MV, 10 MV-FFF, 10 MV and 15 MV 10x10 cm^2 open fields. Variances were scored at 10 cm depth in a water phantom with 0.5x0.5x0.5 cm^3 voxels. The uncertainty in the calculated variances is less than 0.14 %.

Table 5.2: Calculated latent variance values for 6 MV-FFF, 6 MV, 10 MV-FFF, 10 MV and 15 MV 10x10 cm^2 open fields, in 0.5x0.5x0.5 cm^3 voxels at different depths in water.

	Latent variance (%)				
	Energies (MV)				
Depth, cm	6	10	15	6 MV-FFF	10 MV-FFF
0.25	1.39	1.41	1.32	0.73	0.56
1.5	1.05	0.92	0.82	0.61	0.36
10	0.96	0.69	0.57	0.47	0.35

As seen from Table 5.2, at 10 cm depth, latent variances are minimal and decrease as the beam energy increases; the latent variances for FFF beams are nearly half those for flattened beams.

Latent variances, calculated for a 6 MV 10x10 cm^2 open field at different phantom depths are shown in Figure 5.3. Calculated latent variances were found to be the highest at the surface, and decreased with depth until plateauing at about 5 cm.

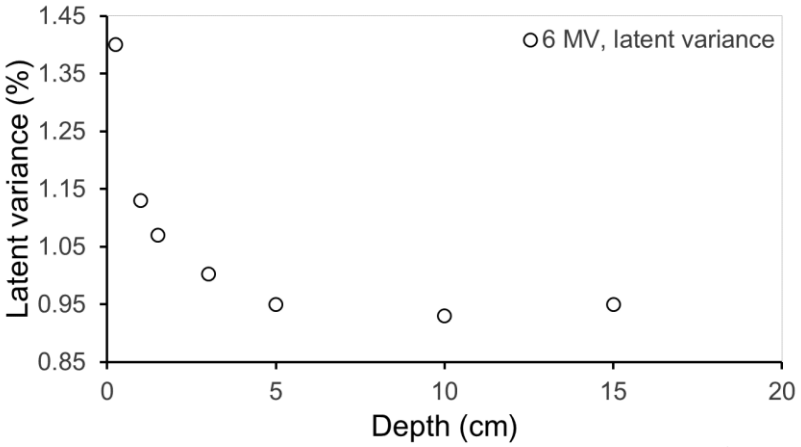

Figure 5. 3**:** Latent variance (LV_B), calculated for 6MV open 10x10 cm^2 field as a function of depth in a water phantom with 0.5x0.5x0.5 cm^3 voxels.

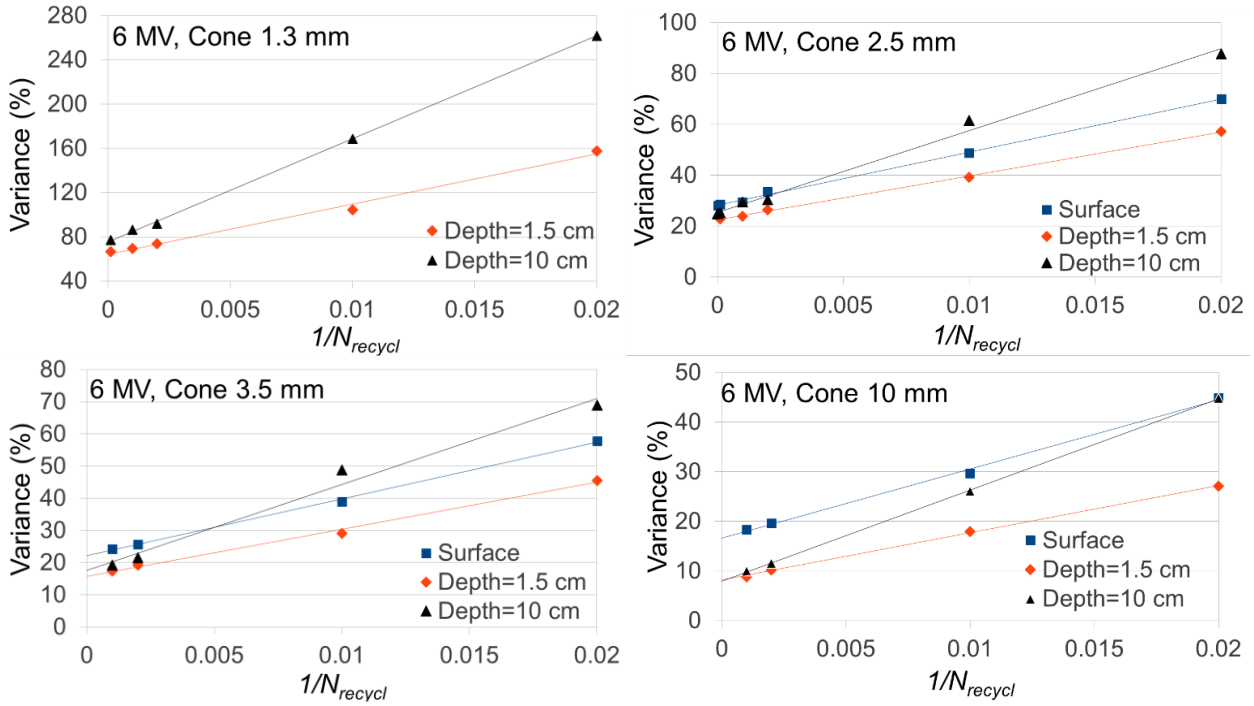

Figure 5.4**:** Latent variance evaluation plots (dose variance vs $\frac{1}{N_{recyl}}$) for 0.13 cm, 0.25 cm, 0.35 cm and 1.0 cm 6MV SRS fields. Variances were scored in a 0.1x0.1x0.5 cm^2 located at the central axis of the beam. The uncertainty in the calculated variances is less than 1 %.

Figure 5.4 presents the latent variance evaluation plots for 6 MV circular fields. Latent variance values at 0.25 cm, 1.5 cm, and 10 cm depths are shown in Table 5.3. In general, evaluated latent variances increased as the cone size decreased. Unlike open 10x10 cm^2 field, latent variances were minimal at the depth of 1.5cm.

Table 5.3: Latent variance values for 6 MV SRS small fields evaluated at different depths in the phantom, in 0.1x0.1x0.5 cm^3 voxels.

	Latent variance %			
	Small SRS fields			
Depth, cm	Cone 0.13 cm	Cone 0.25 cm	Cone 0.35 cm	Cone 1.0 cm
0.25	268.2	28.3	22.1	16.7
1.5	66.0	22.5	15.8	8.2
10	75.6	25.4	17.6	8.0

Latent variance values for the small fields at 0.25 cm, 1.5 cm, and 10 cm depths are shown in Table 5.3. The evaluated latent variances increased as the cone size decreased, but unlike open 10x10 cm^2 field, latent variances were minimal at the depth of 1.5 cm.

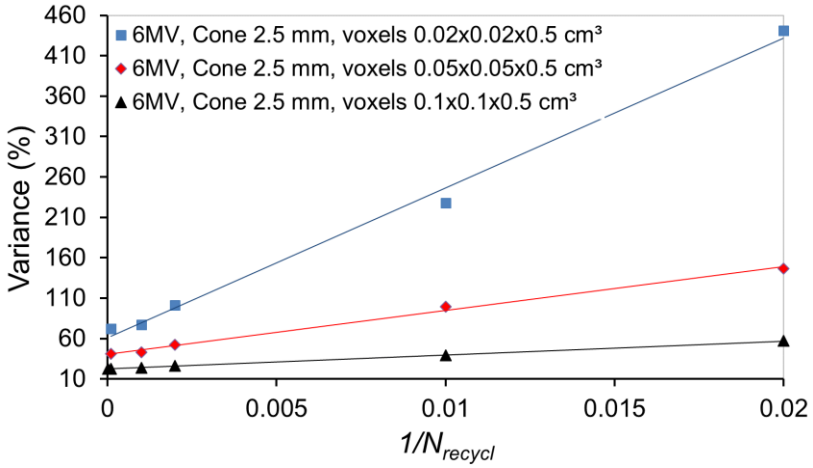

Figure 5.5**:** Latent variance evaluation plots (dose variance vs $1/N_{recyl}$) for 6 MV, 0.25 cm field. Variances were scored in voxels of 0.02x0.02x0.5 cm^3, 0.05x0.05x0.5 cm^3 and 0.1x0.1x0.5 cm^3 size, at 1.5 cm depth. The uncertainty in the calculated variances is less than 1%.

LV evaluation plots for 0.25 cm cone-collimated 6 MV beams, with variance scored in different voxel sizes at 1.5 cm depth, are shown in Figure 5.5. The LV values were found to be 61.2%, 40.7% and 22.5% for voxels of 0.02x0.02x0.5 cm^3, 0.05x0.05x0.5 cm^3 and 0.1x0.1x0.5 cm^3 size, respectively.

Table 5.4 shows an estimated number of Varian 6 MV PSFs needed to achieve latent variances of 1% at 1.5 cm depth for the various cones investigated in this work, as well as for 10x10 cm^2 open field. As shown in the Methods the number of PSFs that needs to be summed up is equal to the value of LV expressed in percent.

Table 5.4: Estimated number of 6 MV Varian TrueBeam PSFs needed to achieve the latent variance of 1.0% at 1.5 cm depth. The variance was scored in 0.5x0.5x0.5 cm^3 voxels for 10x10 cm^2 open field and in 0.1x0.1x0.5 cm^3 voxels for the small cones.

	LV of a full TrueBeam PSF	**Number of single PSFs required to achieve 1.0% LV**
10x10 cm^2 (6 MV)	1.05%	~ 1
Cone 1.0 cm	8.2%	~ 8
Cone 0.35 cm	15.8%	~ 16

Cone 0.25 cm	22.5%	~ 23
Cone 0.13 cm	66.0%	~ 66

5.3. Discussion

To the best of our knowledge this is the first study evaluating the LV in the MC calculated dose for small and very small fields. The impact of field size and phantom voxel size on the LV was also evaluated. For standard 10x10 cm^2 fields LV was evaluated for different energies and depths in the phantom.

Our results for small fields demonstrate a dramatic impact of LV on MC calculations for small field dosimetry. They show that even by summing up all fifty PSFs, currently available for TrueBeam linac, it would be impossible to reduce the LV below 1% for calculations with very small (smaller than about 0.15 cm) fields and 0.1x0.1x0.5 cm^3 voxels. For calculations that require higher resolution the problem is even more exacerbated and accurate calculations are only achievable through using LV reduction techniques.

LV reduction techniques that utilize circular symmetry of the phase space above secondary collimators have been previously proposed and investigated (Brualla & Sauerwein, 2010; K Bush, Zavgorodni, & Beckham, 2007; Fix, Keall, Dawson, & Siebers, 2004). These techniques have shown the capability to reduce the LV by more than a factor of 20 (Bush *et al* 2007) for calculations with particle transport in a Cartesian coordinate system. However, the reduction in PSF LV was shown to be proportional to the radial distance (measured in voxel sizes) from the beam central axis. Thus, such variance reduction techniques would not be efficient for modelling applications that require high accuracy in voxels at the CAX, and summing up of many PSF's would be required.

Walters et al. (2002) investigated the effect of recycling on uncertainty in the "history by history" method of uncertainty estimation. For an 18 MeV electron beam (20x20 cm^2, SSD=100 cm) they found that when the recycling number was largest (twenty seven), the uncertainty was high at the surface and decreased with depth until reaching the minimum at a depth of about 5 cm. Uncertainty increased gradually beyond that depth. The increase of uncertainty at the surface was attributed to the fact that scored quantities were grouped by contributions from primary histories. A primary history was defined as a MC trajectory (that includes all secondary generated particles) initiated from the initial electron entering the linac head and all occurrences of this particle created due to recycling. The number of contributions from primary histories that determines uncertainty in a surface voxel was smaller than that at 5 cm depth because more primary particles reached the voxel and interacted due to their scatter from a wider area. Similar

to the results by Walters *et al.* (2002), latent variances in our study were largest at the surface, and this behaviour, as well as the behaviour of LV with field size, voxel size and beam energy can be explained through the number of primary particles contributing to the dose in a voxel. The number of contributions will indeed increase with field or voxel size, and it will increase with beam energy due to more forward directed particle fluence. Likewise, un-flattened beams are also more forward directed producing more interactions in a voxel at the central axis and subsequently lower LV.

Our results show that for 10x10 cm^2 open field simulations with different beam energies, sub-percent LV can be achieved with a single PSF as the evaluated latent variances range from 0.35% to 1%. This is consistent with the findings by Cronholm and Behrens (2013). They evaluated latent uncertainties of Varian TrueBeam version 1 phase-spaces for 10x10 cm^2 field and 0.25x0.25x0.25 cm^3 voxels located near the beam isocenter, and found them to be 0.85%, 1.02%, 0.41% and 0.74% for the 6 MV-FFF, 6 MV, 10 MV-FFF and 10 MV photon beams, respectively. These results were published in a conference abstract that did not contain substantial details of the calculations.

Our estimated number of phase-spaces in Table 5.4, shows that small field calculations require phase-spaces with a high density of "primary" particles to maintain an acceptable statistical uncertainty in the end result. Currently, most studies that use phase spaces as a particle source in MC calculations do not explicitly evaluate latent variance in their calculations (Hamza Benmakhlouf, Sempau, & Andreo, 2014a; Gete et al., 2013; Teke et al., 2015). Some authors (Teke et al (2015)) state the number of PSFs combined to obtain required statistical uncertainty, whereas many other authors do not. In either case these studies use rather "intuitive" and approximate estimates on the number of PSFs required to achieve reported uncertainties. Our work helps to make these estimates more quantitative and allows establishing a baseline of LV values to be expected in MC dosimetry calculations.

5.4. Conclusions

The number of PSFs that needs to be summed up was evaluated and provided in this study and shown to be about equal numerically to the value of latent variance evaluated for the conditions of the simulation.

A single phase-space (Varian version 2, ~1 GB in size) should be sufficient to achieve sub-percent latent variance for 10x10 cm^2 fields in 0.5x0.5x0.5 cm^3 voxels when using Varian TrueBeam PSFs. However, many PSFs would have to be summed up for accurate small field MC calculations.

Chapter 6

6. Dosimetry in small and very small fields

Small photon beams are often used in modern radiotherapy to treat brain tumors and functional disorders. For example, trigeminal neuralgia is a brain nerve disorder where treated volume can be as small as 2 mm and is typically irradiated with a single high dose fraction of radiation in the order of 80 Gy (Lettmaier, 2014). Also, in IMRT and VMAT delivery of stereotactic radiotherapy treatments of small tumors apertures of the size of 2 mm and less are not uncommon. Therefore, establishing accurate dosimetry in 1-3 mm diameter fields becomes important for quality assurance protocols and safe delivery of such treatments. This chapter present a study towards achieving the second objective of the thesis: accurate dosimetry in small radiation fields. The study in this chapter was published as a paper in the *Physics in Medicine & Biology* (E. Alhakeem & Zavgorodni, 2018).

AUTHOR'S CONTRIBUTION TO THE PUBLISHED PAPER

Contribution to the paper in this Chapter are:

Eyad A. Alhakeem, (Candidate)

Wrote the first draft of the manuscript and contributed to subsequent revisions, developed the study design, and performed the experimental and calculation work (film, diamond, diode measurements and MC calculations). Analyzed and interpreted the data.

Sergei F. Zavgorodni

Contributed to manuscript, the study design, and the data interpretation.

6.1. Introduction

Das *et al* (2008), summarized the challenges associated with small fields dosimetry. These challenges were described in Chapter 1 and include lack of lateral charge equilibrium, source occlusions, and detector perturbations. In order to minimize possible dosimetric errors, the IAEA-AAPM TRS-483 (Palmans et al., 2017) provided guidelines on small field dosimetry. This report defines small fields, provides recommendations on suitable detectors and good working practice for dosimetry in such conditions.

Scott *et al* (2008), investigated dosimetric properties of 5x5 mm^2-100×100 mm^2 photon fields. Output factors (*OF*) measured by all dosimeters were in agreement to within 1% for fields greater than 20×20 mm^2, and within 2.8% for the 15×15 mm^2 field. However, for the 5×5 mm^2 field, the maximum difference in measured *OF* was 8.5%.

Marsolat *et al* (2013), compared *OF* measurements made with a single crystal diamond dosimeter (SCDDo) against other small field detectors for 6 MV and 18 MV beams. BrainLab micromultileaf m3 collimators were used to generate 6×6 mm^2 to 100×100 mm^2 fields. A maximum variation of 11.7% was found in measured *OF*'s for the 6×6 mm^2 field size. Such variations in obtained *OF*'s indicate significant impact of dosimeter material, geometry and shape on *OF* measurements when the field sizes are comparable to the detector size.

To address the problems associated with small field dosimetry Alfonso *et al* (2008) proposed a formalism introducing a small field output correction factor ($k_{Q_{\mathrm{clin}},Q_{\mathrm{msr}}}^{f_{\mathrm{clin}},f_{\mathrm{msr}}}$), since k_Q factors (Almond et al., 1999) that were previously defined in the external beam radiotherapy code of practice are not sufficient to correct for detector response in small photon fields.

Current literature shows that deriving $k_{Q_{\mathrm{clin}},Q_{\mathrm{msr}}}^{f_{\mathrm{clin}},f_{\mathrm{msr}}}$ factors has been a considerable challenge for fields less than 10 mm diameter, and published results are rather contradictory (H Benmakhlouf, Johansson, Paddick, & Andreo, 2015; Hamza Benmakhlouf, Sempau, & Andreo, 2014b; G Cranmer-Sargison, Weston, Evans, Sidhu, & Thwaites, 2012; Dieterich & Sherouse, 2011; Ralston et al., 2012; Ralston, Tyler, Liu, McKenzie, & Suchowerska, 2014; Tyler et al., 2013). Bassinet *et al* (2013) measured the *OF* of small photon beams using several detectors and determined their $k_{Q_{\mathrm{clin}},Q_{\mathrm{msr}}}^{f_{\mathrm{clin}},f_{\mathrm{msr}}}$ factors. They found that EBT2 and microcubes have a close to unity correction factors. Ralston *et al* (2014) used EBT2 film to derive $k_{Q_{\mathrm{clin}},Q_{\mathrm{msr}}}^{f_{\mathrm{clin}},f_{\mathrm{msr}}}$ for the PTW (T60019) microDiamond detector and reported it over-responded by 4-5% in a 4-mm field. Underwood *et al* (2015) measured correction factors for microDiamond detector in 5 mm 6 MV field and reported an over-response of 4-5%. This agrees with recent IAEA-AAPM report on small field dosimetry (Palmans et al., 2017). Other studies on the PTW microDiamond detector (Chalkley & Heyes, 2014; José Manuel Lárraga-Gutiérrez, Ballesteros-Zebadúa, Rodríguez-Ponce, García-Garduño, & de la Cruz, 2015; Morales, Crowe, Hill, Freeman, & Trapp, 2014;

Pedro Andreo, Palmans, Marteinsdóttir, Benmakhlouf, & Carlsson-Tedgren, 2016) contradict these results and concluded that microDiamond was almost equivalent to water for 6 MV fields as small as 5 mm diameter.

MC calculations of $k_{Q_{\mathrm{clin}},Q_{\mathrm{msr}}}^{f_{\mathrm{clin}},f_{\mathrm{msr}}}$ factors for very small (smaller than 4 mm diameter) fields are also not straightforward. In addition to the challenges associated with statistical uncertainties in dose calculations for very small volumes, there is also an ongoing debate in the literature (Pedro Andreo & Palmans, 2016; Marinelli, Prestopino, Verona, & Verona-Rinati, 2016a, 2016b) on whether the lack of accurate design specifications for the microDiamond detector could be the source of inconsistency between experimental and MC derived $k_{Q_{\mathrm{clin}},Q_{\mathrm{msr}}}^{f_{\mathrm{clin}},f_{\mathrm{msr}}}$ factors. On one hand the size and shape of active volume is well established and its variations from detector to detector are very small (Marinelli et al., 2016a). On the other hand, some metallic components within detector geometry that are seen in x-ray images, are not included in the diagrams provided by the manufacturer. This could potentially lead to discrepancies between experiment and MC results as indicated by Andreo *et al* (2016).

In this Chapter, $k_{Q_{\mathrm{clin}},Q_{\mathrm{msr}}}^{f_{\mathrm{clin}},f_{\mathrm{msr}}}$ factors for microDiamond and unshielded EFD-3G detectors were derived experimentally (using GafChromic EBT3 films) and calculated using MC for a range of Varian TrueBeam 6 MV fields from 1.27 to 40 mm in diameter. $k_{Q_{\mathrm{clin}},Q_{\mathrm{msr}}}^{f_{\mathrm{clin}},f_{\mathrm{msr}}}$ factors were calculated for several detector orientations relative to the beam central axis (CAX). The impact of the possible variations in microDiamond detector inner schematics on the calculated $k_{Q_{\mathrm{clin}},Q_{\mathrm{msr}}}^{f_{\mathrm{clin}},f_{\mathrm{msr}}}$ correction factors was also investigated. This is the first report that investigates $k_{Q_{\mathrm{clin}},Q_{\mathrm{msr}}}^{f_{\mathrm{clin}},f_{\mathrm{msr}}}$ factors for fields smaller than 4 mm.

6.2. Materials and Methods

6.2.1. Implementation of small field's dosimetry formalism for $k_{Q_{clin},Q_{msr}}^{f_{clin},f_{msr}}$ factor MC calculations and EBT3 film measurements.

Alfonso *et al* (2008), introduced dosimetry formalism for small and non-standard radiotherapy fields. A correction factor ($k_{Q_{\mathrm{clin}},Q_{\mathrm{msr}}}^{f_{\mathrm{clin}},f_{\mathrm{msr}}}$) was introduced to correct a detector response in small clinical fields (f_{clin}) relative to its response in the reference field (f_{ref}). For machines that cannot produce a 10×10 cm^2 reference field, a machine specific reference field (f_{msr}) is used instead. This output correction factor is defined as

$$k^{f_{\text{clin}},f_{\text{msr}}}_{Q_{\text{clin}},Q_{\text{msr}}} = \frac{D^{f_{\text{clin}}}_{\text{w},Q_{\text{clin}}} / M^{f_{\text{clin}}}_{Q_{\text{clin}}}}{D^{f_{\text{msr}}}_{\text{w},Q_{\text{msr}}} / M^{f_{\text{msr}}}_{Q_{\text{msr}}}} \quad (6.1)$$

where

$D^{f_{\text{clin}}}_{\text{w},Q_{\text{clin}}}$ is absorbed dose to water at reference depth in a phantom for clinical field f_{clin} of beam quality Q_{clin}.

$D^{f_{\text{msr}}}_{\text{w},Q_{\text{msr}}}$ is absorbed dose to water at reference depth in a phantom for machine specific reference field f_{msr} of beam quality Q_{msr}.

$M^{f_{\text{clin}}}_{Q_{\text{clin}}}$ is detector reading at reference depth in a phantom for clinical field f_{clin} of beam quality Q_{clin}.

$M^{f_{\text{msr}}}_{Q_{\text{msr}}}$ is detector reading at reference depth in a phantom for machine specific reference field f_{msr} of beam quality Q_{msr}.

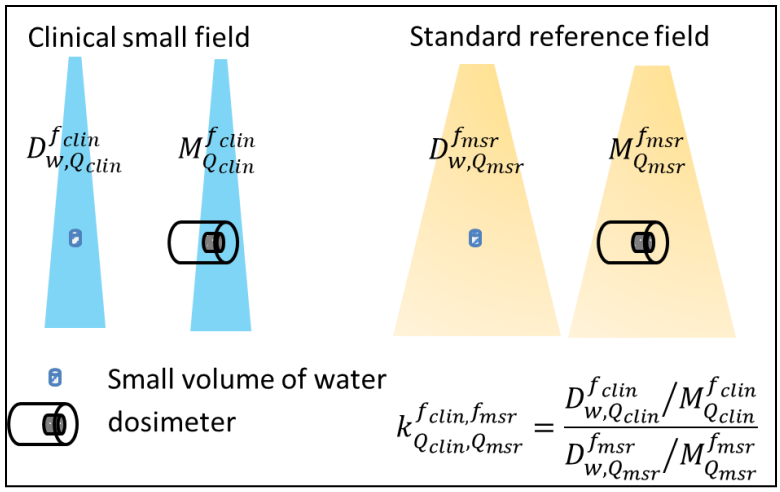

Figure 6.1: Schematic illustrating different components in the output correction factor ($k^{f_{clin},f_{msr}}_{Q_{clin},Q_{msr}}$) as defined by Alfonso *et.al*. The ratio $\frac{D^{f_{clin}}_{w,Q_{clin}}}{D^{f_{msr}}_{w,Q_{msr}}}$ converts absorbed dose to water in machine specific reference field (f_{msr}) to absorbed dose to water in a clinical field, and is used to correct the detectors response in clinical field relative to the machine specific field ($\frac{M^{f_{clin}}_{Q_{clin}}}{M^{f_{msr}}_{Q_{msr}}}$).

Figure 6.1 illustrates the different components in the $k_{Q_{clin},Q_{msr}}^{f_{clin},f_{msr}}$ factor definition. The ratio $\frac{M_{Q_{\text{clin}}}^{f_{\text{clin}}}}{M_{Q_{\text{msr}}}^{f_{\text{msr}}}}$ in Equation (6.1) corrects the detector response in the clinical field relative to the machine specific field and will be defined here as the detector output factor (OF_{det}).

$$OF_{\text{det}} = \frac{M_{Q_{\text{clin}}}^{f_{\text{clin}}}}{M_{Q_{\text{msr}}}^{f_{\text{msr}}}} \tag{6.2}$$

In MC calculations for non-water equivalent detectors this factor is derived by modeling the detector geometry (and construction materials) and scoring the dose in the sensitive volume of the detector placed in clinical as well as reference fields.

The other ratio $\frac{D_{w,Q_{\text{clin}}}^{f_{\text{clin}}}}{D_{w,Q_{\text{msr}}}^{f_{\text{msr}}}}$ in equation (6.1) converts absorbed dose to water in the machine specific reference field to absorbed dose to water in a clinical field. It is commonly known as field output factor $\Omega_{Q_{\text{clin}},Q_{\text{msr}}}^{f_{\text{clin}},f_{\text{msr}}}$ and can be obtained using perturbation-free dosimeter (with $k_{Q_{\text{clin}},Q_{\text{msr}}}^{f_{\text{clin}},f_{\text{msr}}} = 1,\ \Omega_{Q_{\text{clin}},Q_{\text{msr}}}^{f_{\text{clin}},f_{\text{msr}}} = \frac{D_{w,Q_{\text{clin}}}^{f_{\text{clin}}}}{D_{w,Q_{\text{msr}}}^{f_{\text{msr}}}} = \frac{M_{Q_{\text{clin}}}^{f_{\text{clin}}}}{M_{Q_{\text{msr}}}^{f_{\text{msr}}}}$). In measurements with perturbation-free dosimeter $\Omega_{Q_{\text{clin}},Q_{\text{msr}}}^{f_{\text{clin}},f_{\text{msr}}} = OF_{\text{det}}$. In MC calculations, that are also perturbation-free in water, $\Omega_{Q_{\text{clin}},Q_{\text{msr}}}^{f_{\text{clin}},f_{\text{msr}}}$ is derived as the ratio of the doses from clinical and reference fields scored in small volumes of water.

In general, from equation (6.1), the field output factor $\Omega_{Q_{\text{clin}},Q_{\text{msr}}}^{f_{\text{clin}},f_{\text{msr}}}$ can be described as the detector output factor (OF_{det}) multiplied by its correction factor ($k_{Q_{\text{clin}},Q_{\text{msr}}}^{f_{\text{clin}},f_{\text{msr}}}$) :

$$\Omega_{Q_{\text{clin}},Q_{\text{msr}}}^{f_{\text{clin}},f_{\text{msr}}} = OF_{\text{det}} \cdot k_{Q_{\text{clin}},Q_{\text{msr}}}^{f_{\text{clin}},f_{\text{msr}}} \tag{6.3}$$

Previous studies showed that EBT2/3 films do not require correction factors in small field dosimetry (Bassinet et al., 2013; José M. Lárraga-Gutiérrez, 2014; Novotny Josef et al., 2009). Thus, in this work, EBT3 film is assumed to be the perturbation-free dosimeter ($k_{Q_{\text{clin}},Q_{\text{msr}}}^{f_{\text{clin}},f_{\text{msr}}} = 1$), and therefore $\Omega_{Q_{\text{clin}},Q_{\text{msr}}}^{f_{\text{clin}},f_{\text{msr}}} = OF_{\text{EBT}}$ was used in equation (6.3) to experimentally derive the $k_{Q_{\text{clin}},Q_{\text{msr}}}^{f_{\text{clin}},f_{\text{msr}}}$ factors for microDiamond and EFD-3G detectors as follows

$$k_{Q_{\text{clin}},Q_{\text{msr}}}^{f_{\text{clin}},f_{\text{msr}}} = \frac{\Omega_{Q_{\text{clin}},Q_{\text{msr}}}^{f_{\text{clin}},f_{\text{msr}}}}{OF_{\text{det}}} = \frac{OF_{\text{EBT}}}{OF_{\text{det}}} \tag{6.4}$$

$k_{Q_{\mathrm{clin}},Q_{\mathrm{msr}}}^{f_{\mathrm{clin}},f_{\mathrm{msr}}}$ factor could also be looked at as a product of two independent corrections that arise from non-water equivalency and finite size of the detector sensitive volume:

$$k_{Q_{\mathrm{clin}},Q_{\mathrm{msr}}}^{f_{\mathrm{clin}},f_{\mathrm{msr}}} = k\left(_{Q_{\mathrm{clin}},Q_{\mathrm{msr}}}^{f_{\mathrm{clin}},f_{\mathrm{msr}}}\right)_{\mathrm{no\ vol}} \times P_{\mathrm{vol}}^{\mathrm{det}} \qquad (6.5)$$

Where, $k\left(_{Q_{\mathrm{clin}},Q_{\mathrm{msr}}}^{f_{\mathrm{clin}},f_{\mathrm{msr}}}\right)_{\mathrm{no\ vol}}$ is the correction factor for an imaginary detector with infinitely small sensitive volume but the same geometry and materials as the detector under study. Volume averaging correction factor for such an imaginary detector would be unity. Indeed, equation (6.5) includes an assumption that the difference in particle fluence through the real detector as compared to an imaginary one is negligible. Volume averaging correction factor $P_{\mathrm{vol}}^{\mathrm{det}}$ is well recognized as an essential correction in small field dosimetry, and has been described by Papaconstadopoulos *et al* (2014). $P_{\mathrm{vol}}^{\mathrm{det}}$ factor can be calculated using MC as the ratio of dose deposited in a very small volume of water (D_{w}) to the dose deposited in the volume of water ($D_{\mathrm{vol,w}}$) equal to the detector sensitive volume

$$P_{\mathrm{vol}}^{\mathrm{det}} = \frac{D_{\mathrm{w}}}{D_{\mathrm{vol,w}}} \qquad (6.6)$$

Inclusion of these two factors into our modeling allowed investigation of the balance between energy response and the volume averaging in microDiamond and EFD-3G detectors.

6.2.2. Small filed collimators

BrainLab SRS cones in conjunction with a Varian TrueBram linac were used to produce small circular fields of 10, 12.5, 15 and 40 mm in diameter. In addition, three in-house collimators were used to produce very small circular fields of 1.27, 2.46 and 3.77 mm in diameter. These customized collimators were built by Mr. Steve Gray at the Vancouver Island Centre (VIC). Figure 6.2, shows pictures of the BrainLab cones and two in-house collimators.

Figure 6.2**:** The BrainLab SRS collimators and two of the in-house collimators (1.27 and 3.77 mm) are shown.

The manufacturing quality of these collimators were checked and verified for their aperture alignment. The linac MV imager was used to capture MV images of the collimators from the lateral and axial directions and these are shown in Figure 6.3. These images were visually inspected to check the aperture alignment of collimators.

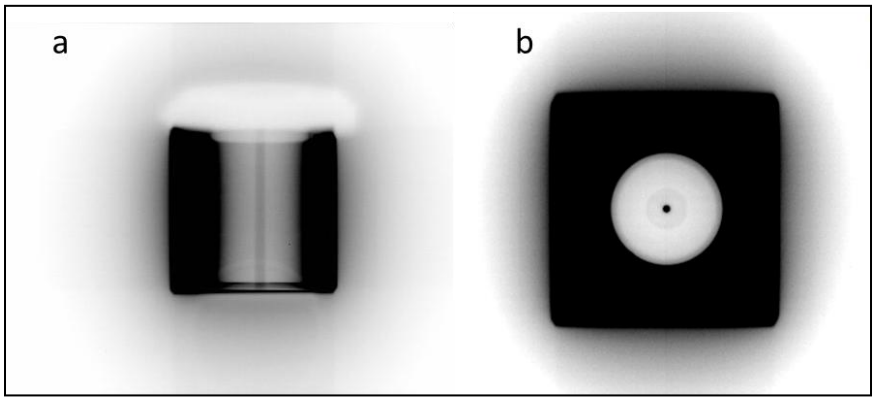

Figure 6.3**:** MV images of the 3.77 mm customized collimator was captured using the linac MV imager. Lateral (a) and axial (b) images of the collimator are shown.

To further check the aperture alignment, a pixel-intensity profile across the centre of aperture was captured as illustrated in Figure 6.4. The estimated width of these profiles (FWHM) were as expected from the known nominal openings of the collimators.

The quality check indicated that the collimators were accurately made with precise aperture alignment and therefore used in this study to produce small radiation fields.

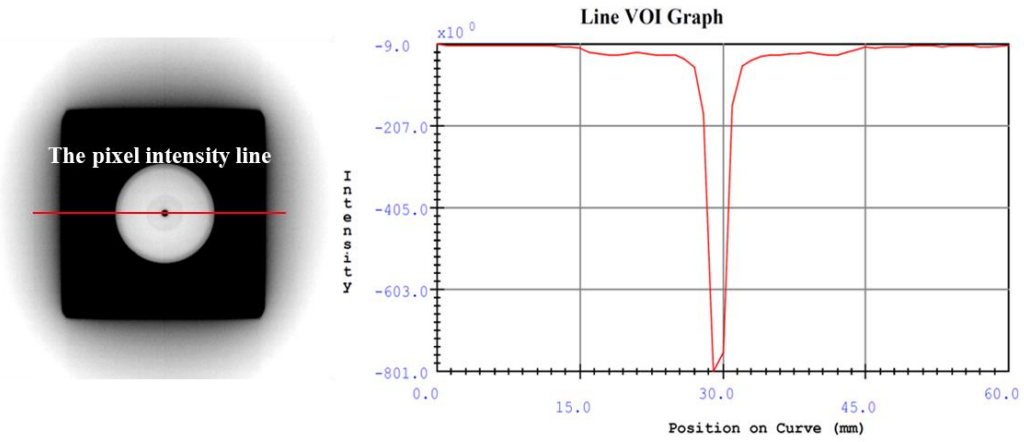

Figure 6.4**:** The pixel intensity profile captured across the aperture center from the MV image of the 3.77 mm customized collimator.

6.2.3. Experimental measurements

Varian TrueBeam (Varian Medical Systems, Palo Alto, California) linac with BrainLab SRS cones (BrainLAB AG, Feldkirchen, Germany) was used to generate 6 MV circular fields. The BrainLab circular collimators were 10, 12.5, 15 and 40 mm nominal fields. Three in-house customized collimators, described above, were used to produce very small circular fields of 1.27, 2.46 and 3.77 mm in diameter. Any small misalignment of these collimators relative to the beam axis would negatively impact the accuracy of the measurements. Therefore, careful alignment of the collimators was performed prior to measurements. A “machinist dial” indicator was used to ensure that the collimators were perfectly aligned relative to the beam axis while mounted on the linac head. In order to quantify the degree of tilt relative to the beam axis the dial was used on two different spots (at very top and bottom) of the collimators’ outer circumference. A full collimator rotation was performed while adjusting its alignment to minimize the tilt as much as possible, as shown in Figure 6.5.

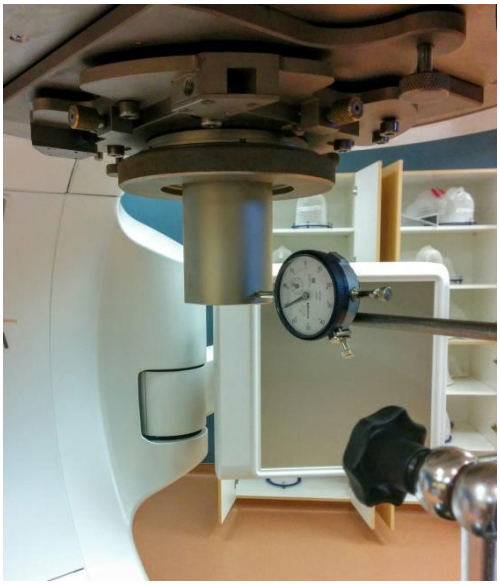

Figure 6.5**:** A picture showing the collimator alignment setup. A dial is used to gauge and minimize tilt while rotating the collimator around beam axis.

Measurements were taken with the detectors placed at the isocenter and 1.5 cm depth in Solid Water ("RMI-457", Gammex RMI, Middleton, WI) (Figure 6.6). The relative output factors were obtained as in Equation (6.2) from the ratio of the detector reading in clinical field to its reading in the reference field of 40 mm diameter.

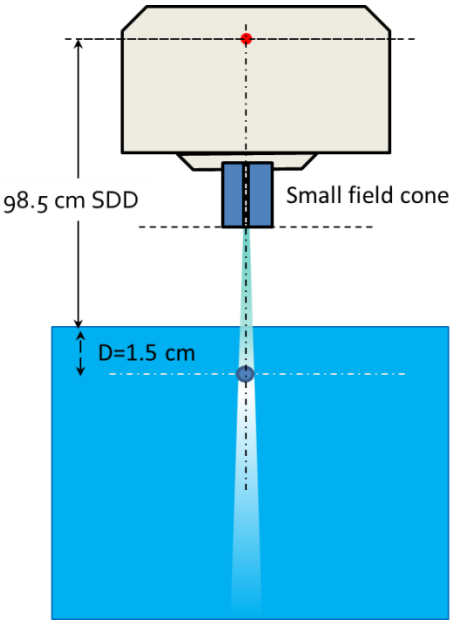

Figure 6.6**:** Diagram illustrating the beam configuration and the measurement setup.

PTW-60019 microDiamond (PTW-Freiburg, Germany) and IBA EFD-3G diode (IBA-Dosimetry, Germany) detectors were used to measure output factors. Both detectors were used with their stems perpendicular to the beam CAX. Thus, only $k_{Q_{\text{clin}},Q_{\text{msr}}}^{f_{\text{clin}},f_{\text{msr}}}$ factors for the perpendicular detector orientation were experimentally derived in this work. To make sure that the detectors were placed exactly at the center of the field, small shifts were introduced to the detectors until maximum signal was measured. The accuracy of the detector alignment in the beam was about 0.1 mm in these measurements. Three readings were recorded for each collimator and the results were averaged. At least two sets of measurements were performed at different times for each detector to evaluate the setup uncertainties.

GafChromic® EBT3 film (Ashland, Specialty Ingredients, NJ) pieces of 5×5 cm^2 were used to obtain the beam profiles and output factors. The exposed pieces of film were scanned at 200-500 dpi scanner resolution. Output factor readings were extracted from a 3×3 pixels size area (0.4×0.4 - 0.15×0.15 mm^2) at the center of the field. Film calibration, scanning and image processing were carried out as described previously in Chapter 3. Lateral dose profiles and *OF*s were then extracted from the films.

Dosimetric field sizes defined by the full width at half maximum (FWHM) were determined from dose profiles for all fields and these were used in OF_{det} comparisons with MC calculations as per (Gavin Cranmer-Sargison et al., 2013).

$k_{Q_{\text{clin}},Q_{\text{msr}}}^{f_{\text{clin}},f_{\text{msr}}}$ factors for microDiamond and EFD-3G detectors were obtained from equation (6.4) where field output factor was derived from EBT3 measurements: $\Omega_{Q_{\text{clin}},Q_{\text{msr}}}^{f_{\text{clin}},f_{\text{msr}}} = OF_{\text{EBT}}$.

6.2.4. Monte Carlo simulation

BEAMnrc/DOSXYZnrc Monte Carlo codes (Rogers et al., 2009; B. Walters et al., 2005) were used to calculate the field output factor $\Omega_{Q_{\text{clin}},Q_{\text{msr}}}^{f_{\text{clin}},f_{\text{msr}}}$ (ratio of absorbed doses) and dose profiles in a water phantom with 1×1×1 mm^3 voxels for the 10-40 mm cones and 0.1×0.1×0.25 mm^3 voxels for the smaller cones. The modeled parts of the linac, as shown in Figure 6.7, included monitor chamber and mirror above the Varian phase-space file (PSF) to account for the back-scatter factor in the absolute dose calculations as described by Zavgorodni *et al.* (2014). The *egs_chamber* code (Wulff et al., 2008a) was used to model the microDiamond and the EFD-3G diode detectors, and to calculate the dose $M_{Q_{\text{clin/msr}}}^{f_{\text{clin/msr}}}$ deposited in their active volumes.

Source simulation

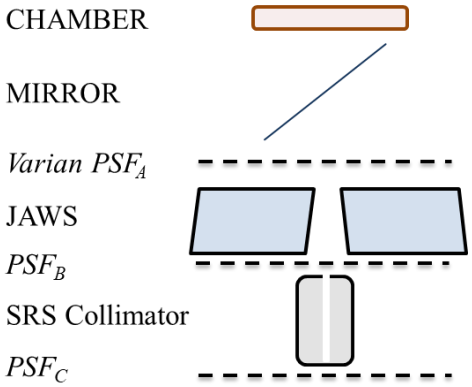

Figure 6.7**:** Schematic of the Monte Carlo model used in BEAMnrc calculations of the *OF*s. Shown are locations of Varian phase space (PSF_A) as well as the high-density particle phase-space (PSF_B) and small fields phase-space PSF_C scored during the different stages of simulation.

The simulation was carried in two stages. First, using the BEAMnrc code forty Varian 6 MV photon phase-space files (PSF_A) were transported through the jaws, set at 5×5 cm^2, and ancillary PSFs were scored straight under the jaws. These forty ancillary files were then summed up into a single phase-space file (PSF_B) beneath the jaws as illustrated in figure 6.7. The resultant PSF_B contained 200×10^9 particles. The large number of PSFs that was used to produce PSF_B was essential for reduction of the latent variance as reported in our recent work (Eyad Ali Alhakeem & Zavgorodni, 2017). In the second stage, particles from the PSF_B were propagated through a circular collimator and scored into another phase-space file (PSF_C) with a density of over 5 million particles per cm^2. Photon (PCUT) and electron (ECUT) cutoff energies were 0.01 MeV and 0.700 MeV, respectively.

These small fields' phase-space files (PSF_C), were used as a particle source for DOSXYZnrc and *egs_chamber* Monte Carlo codes to calculate lateral dose profiles, field output factors and $k_{Q_{\text{clin}},Q_{\text{msr}}}^{f_{\text{clin}},f_{\text{msr}}}$ factors.

Mc calculations to derive lateral profiles and field output factors

PSF_C files were used as a source in DOSXYZnrc to calculate lateral dose profiles as well as output factors from all cones in a water phantom. Photon and electron (PCUT, ECUT) cutoffs were 0.01 MeV and 0.521 MeV, respectively. The "Exact" boundary crossing algorithm was used along with condensed history electron step algorithm PRESTA-II. This provided sufficient

accuracy of the dose deposition even for the smallest 0.1×0.1×0.25 mm^3 voxels used in this work.

Lateral dose profiles were obtained at a depth of 1.5 cm with source to surface distance (SSD) 98.5 cm and were benchmarked against EBT3 film measurements described in section 2.2. Field output factors for each collimator were calculated as the ratio of the doses scored in water for these collimators to the dose from the 40 mm diameter cone at 1.5 cm depth and SSD=98.5 cm.

For the three smallest cones attempts were made to obtain exact match of MC calculated profiles with profiles measured using film by varying the inner diameter of the collimator. However, due to the very time consuming process of collection and summation of ancillary PSFs required for calculating these profiles, exact match of the profiles was not feasible. The FWHM differences between calculated and measured profiles were in the range of 0.05 – 0.18 mm (Table 6.2), and were deemed acceptable as we compare $\Omega^{f_{\mathrm{clin}},f_{\mathrm{msr}}}_{Q_{\mathrm{clin}},Q_{\mathrm{msr}}}$ and $k^{f_{\mathrm{clin}},f_{\mathrm{msr}}}_{Q_{\mathrm{clin}},Q_{\mathrm{msr}}}$ against dosimetric rather than "nominal" field sizes. In table presentation (Tables 6.3-6.5) the values of MC calculated dosimetric field sizes were interpolated for direct comparison with measurement, in graphs the actual calculated values of dosimetric field sizes were used.

Deriving $k^{f_{clin},f_{msr}}_{Q_{clin},Q_{msr}}$ factor with MC calculations

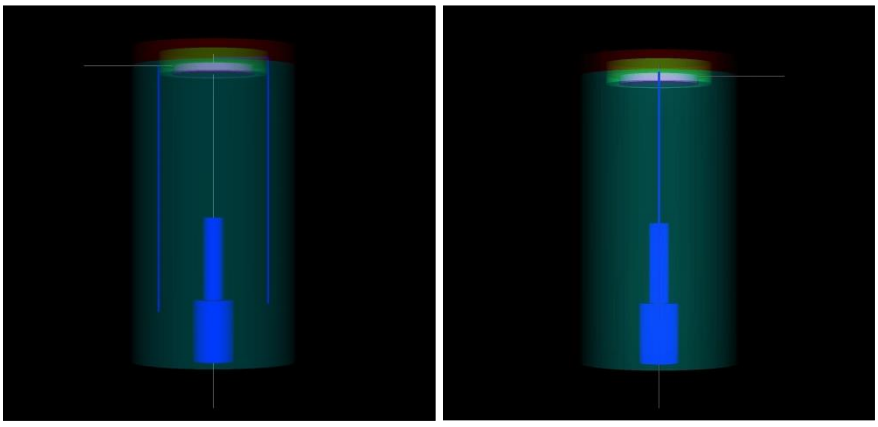

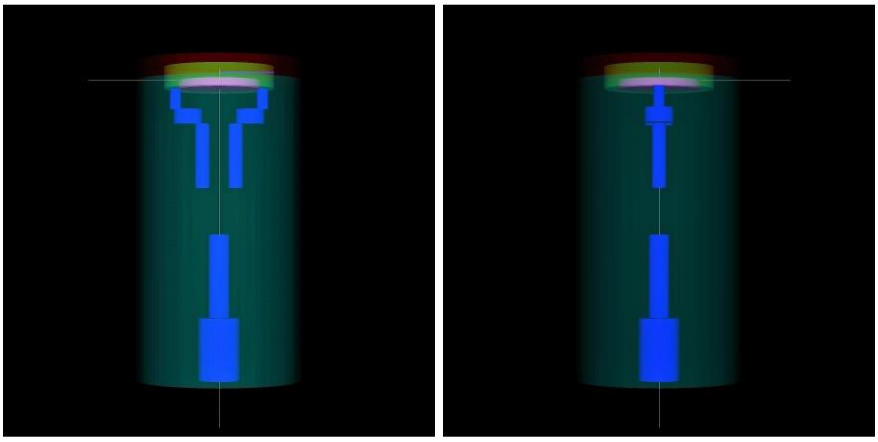

Figure 6.8**:** An *egs_view* (EGSnrc geometry viewing tool) image of two microDiamond detector models. On top, model (A) with no metallic connection pins, and bottom model (B) with metallic connection pins included.

Table 6.1: Detectors geometry and materials included in egs_chamber $k_{Q_{\text{clin}},Q_{\text{msr}}}^{f_{\text{clin}},f_{\text{msr}}}$ simulations.

Detector	**Active volume**				**Capsule materials**
	Material	**Z_{eff}**	**diameter mm**	**Thickness mm**	
microDiamond	Carbon	6	2.2	0.001	RW3, epoxy resin, PMMA Aluminum
EFD-3G diode	Silicon	14	2.0	0.06	Epoxy resin

MC code *egs_chamber* (Wulff et al., 2008a) was used to model two versions of the PTW-60019 microDiamond detector and EFD-3G detector.

Model A (Figure 6.8) of PTW-60019 microDiamond detector was based on available manufacturer specifications and reported geometrical details (Ciancaglioni et al., 2012; Mandapaka et al., 2013; Pimpinella et al., 2012). Model B includes extra metallic pins (Andreo *et al* (2016)) that were assumed to be made of aluminum. Other geometry and material specifications were exactly the same in these modeled versions. The material and geometry specifications for the microDiamond detector are summarized in Table 6.1. *egs_view* (EGSnrc 3D geometry viewing tool) images for both models are presented in Figure 6.8. $k_{Q_{\text{clin}},Q_{\text{msr}}}^{f_{\text{clin}},f_{\text{msr}}}$ factors were calculated for two detector orientations, parallel and perpendicular to the beam CAX as shown in Figure 6.9.

The impact of detector rotation relative to its stem axis while in perpendicular orientation was also investigated for model B where potential impact of this rotation is expected to be greater. Therefore, for model B $k_{Q_{\text{clin}},Q_{\text{msr}}}^{f_{\text{clin}},f_{\text{msr}}}$ factors were calculated for the detector electrodes lined up along the beam CAX, (Figure 6.9-a) and perpendicular to that (figure 6.9-b).

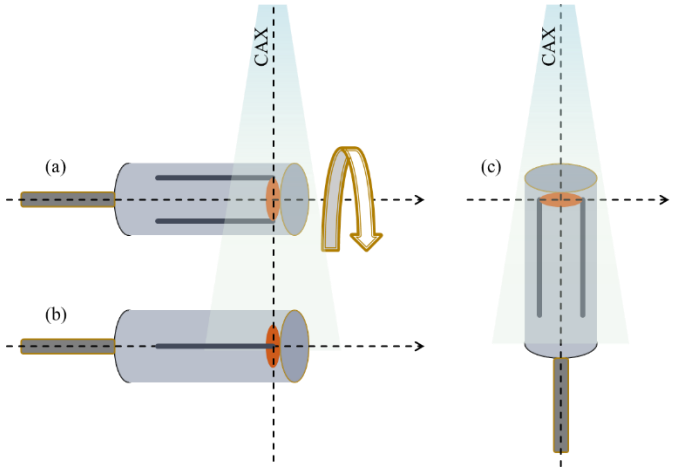

Figure 6.9**:** A diagram illustrating the three modeled orientations of the PTW microDiamond detector relative to the incident beam: a) detector's stem axis is perpendicular to beam CAX and electrodes are lined up along the beam axis, b) detector's stem axis is perpendicular to beam CAX, and electrodes are in a plane orthogonal to CAX, c) the detector's stem axis is aligned along the beam CAX.

For EFD-3G detector the model was simplified relative to its detailed geometry, and only included the silicon chip embedded in the epoxy housing as in Wang and Rogers (2007). Cranmer-Sargison et al (2012) showed that such a simplified model is still accurate; for fields as small as 5x5 mm^2 it produced OF_{det} s within 1% of those calculated by a complete model.

For each field size the $k_{Q_{\text{clin}},Q_{\text{msr}}}^{f_{\text{clin}},f_{\text{msr}}} = \frac{D_{w,Q_{\text{clin}}}^{f_{\text{clin}}} / M_{Q_{\text{clin}}}^{f_{\text{clin}}}}{D_{w,Q_{\text{msr}}}^{f_{\text{msr}}} / M_{Q_{\text{msr}}}^{f_{\text{msr}}}}$ factors were calculated for both microDiamond EFD-3G detectors. $D_{w,Q_{\text{clin}}}^{f_{\text{clin}}}$ and $D_{w,Q_{\text{msr}}}^{f_{\text{msr}}}$ were calculated in a very small cylindrical volume of water of 0.02 cm diameter and 0.03 cm thickness at 1.5 cm depth. $M_{Q_{\text{clin}}}^{f_{\text{clin}}}$ and $M_{Q_{\text{msr}}}^{f_{\text{msr}}}$ were the doses calculated in the detector active volume for the clinical and machine specific reference fields, respectively. Electron (ECUT) and photon (PCUT) cutoffs of 0.512 MeV and 0.01 MeV respectively, were applied. Cross-section enhancement (XCSE) factor of 128 was applied within the active volume and the surrounding layers.

MC calculation of detector volume averaging factor

Detector volume averaging factors $P_{\mathrm{vol}}^{\mathrm{det}}$ were calculated using equation (6.6). *egs_chamber* MC code was used to obtain the ratio of dose deposited in the detector sensitive volume replaced by water ($D_{\mathrm{vol,w}}$) to the dose deposited in a very small cylindrical volume of water (D_{w}) of 0.02 cm diameter $\times$ 0.03 cm height located in the same position within the detector as the sensitive volume. $P_{\mathrm{vol}}^{\mathrm{det}}$ factors were calculated for the 1.27—10 mm collimators with detectors in both parallel and perpendicular orientations.

6.3. Results

6.3.1. Benchmarking the Monte Carlo model

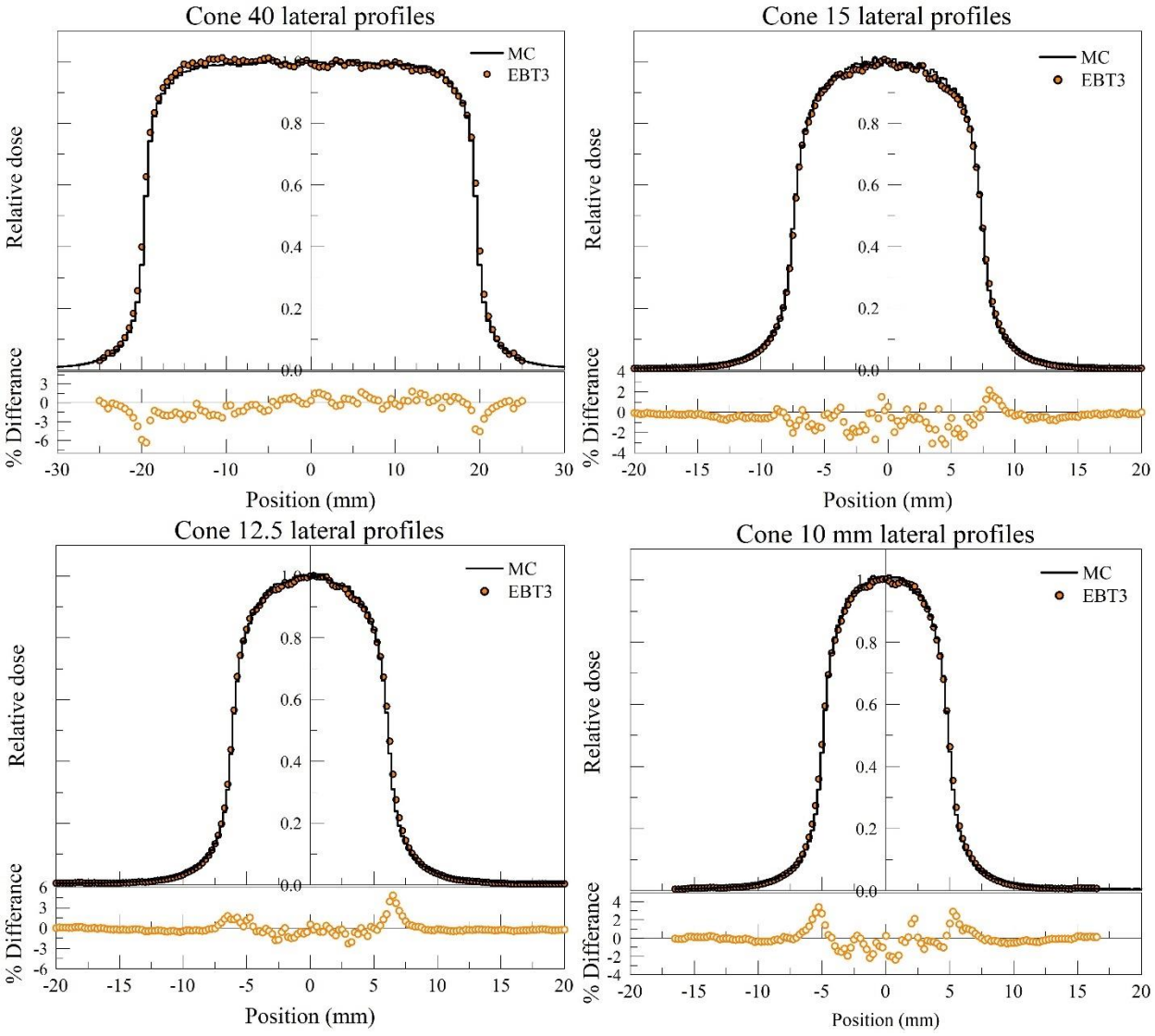
Cone 40 lateral profiles
Cone 15 lateral profiles
Cone 12.5 lateral profiles
Cone 10 mm lateral profiles
MC
EBT3
Relative dose
% Difference
Position (mm)

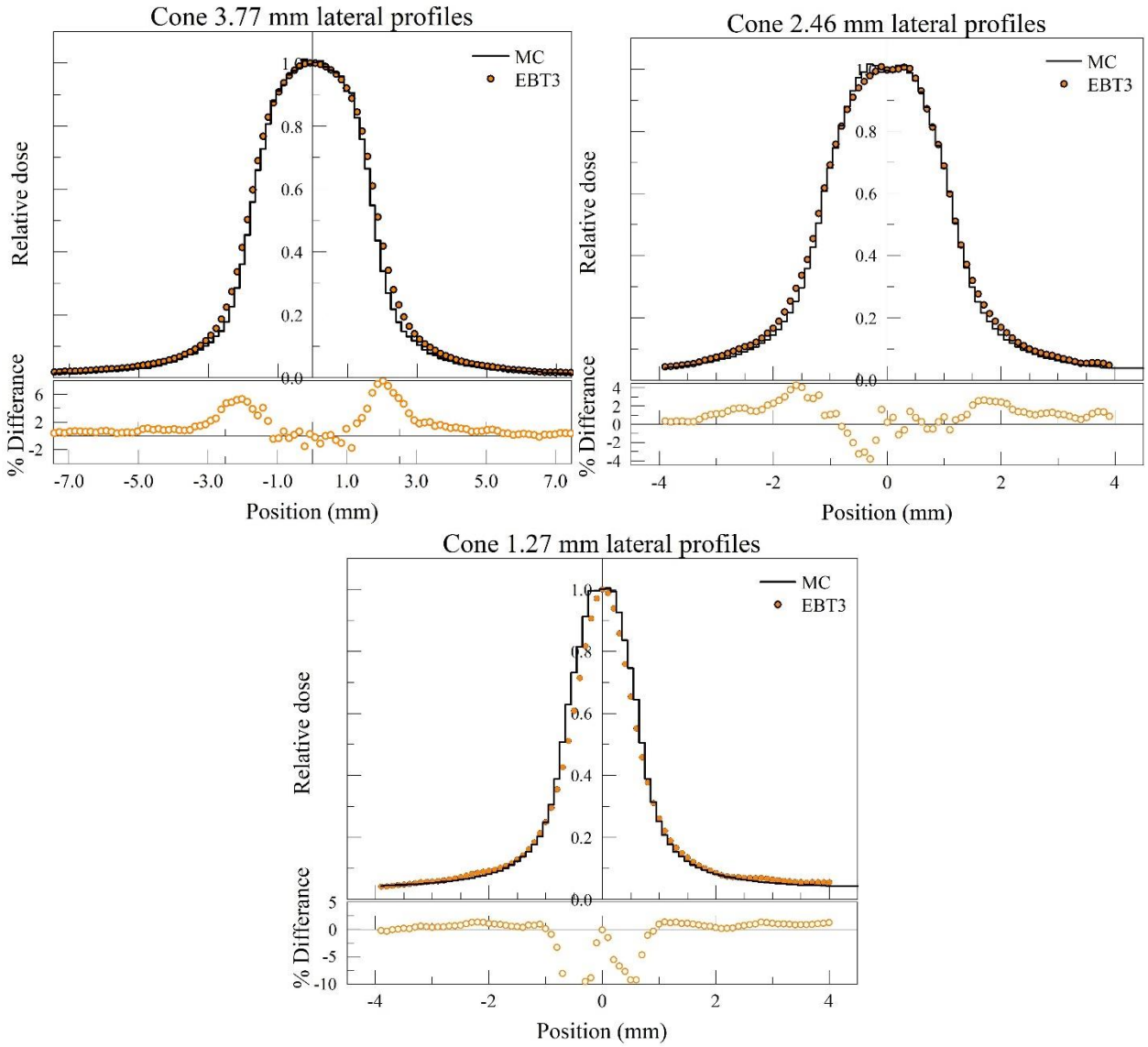

Figure 6.10**:** MC (DOSXYZnrc) calculated dose profiles for 1.27-40 mm collimators compared against EBT3 film measurements.

Figure 6.10 shows MC calculated profiles benchmarked against film measurements for 1.27 – 40 mm cones. Agreement inside the beam aperture between the two data sets is within 2.5% for all fields ≥10 mm. Mean distance-to-agreement (DTA) in the penumbra region (20-80%) for these cones was ≤ 0.2 mm. For the 1.27, 2.46 and 3.77 mm cones the mean DTA in the penumbra region was ≤ 0.15 mm.

6.3.2. Measured and calculated dosimetric fields

Table 6.2: Dosimetric field sizes (FWHM) for the in-house collimators determined from EBT3 and MC profiles.

$FWHM_{EBT3}$ $(\pm\sigma)$	$FWHM_{MC}$ $(\pm\sigma)$	*%Relative difference*
1.27 (±0.03)	1.41 (±0.01)	11%
2.46 (±0.05)	2.41 (±0.02)	-2.1%
3.77 (±0.08)	3.59 (±0.04)	-5%

Table 6.2 shows the dosimetric field sizes for the three smallest collimators obtained from EBT3 films ($FWHM_{EBT3}$) and MC ($FWHM_{MC}$) lateral dose profiles. EBT3 film measurement based dosimetric field sizes are used to present the OF_{det} s and $k_{Q_{clin},Q_{msr}}^{f_{clin},f_{msr}}$ factors in the following sections.

6.3.3. Detector output factors (OF_{det})

Table 6.3: Detector output factors (relative to the 40 mm cone) were experimentally measured for 1.27 – 15 mm circular cones. PTW-60019 microDiamond and IBA EFD-3G diode detectors were used with their stems perpendicular to the beam CAX. Cone size represents the dosimetric field size derived from lateral dose profiles measured with EBT3 film. The bottom line in the table shows the magnitude of largest relative difference (*% Diff*) between any of the measured OF_{det} and EBT3 measurement. The maximum or minimum OF_{det} measured by a detector is denoted as $OF_{det}^{max/min}$. Note that as MC calculations in water and EBT3 film measurement represent perturbation-free techniques their $k_{Q_{clin},Q_{msr}}^{f_{clin},f_{msr}} = 1$.

Cone field size (mm)	**1.27†**	**2.46†**	**3.77†**	**10**	**12.5**	**15**	**40**
microDiamond	0.126	0.509	0.682	0.904	0.935	0.959	1
EFD-3G	0.119	0.504	0.648	0.884	0.914	0.943	1
EBT3	0.145	0.500	0.626	0.883	0.927	0.944	1

MC ($D_{w,Q_{clin}}^{f_{clin}} / D_{w,Q_{msr}}^{f_{msr}}$)	0.148	0.489	0.616	0.873	0.928	0.945	1
$\%Diff = \frac{OF_{det}^{max/min} - OF_{EBT}}{OF_{EBT}} \times 100$	-17.9	1.8	9.0	*2.4*	*-1.4*	*1.6*	-

† In-house customized collimators

Table 6.3 shows the OF_{det} obtained for the 1.27–15 mm cones. MC calculated output factors (in water) for the three smallest cones were linearly interpolated to match measured dosimetric fields of 1.27, 2.46 and 3.77 mm.

For the smallest 1.27 mm collimator, a discrepancy of -17.9% was found between EFD-3G detector and EBT3 film measurements. Maximum differences of 2.4%, 1.4% and 1.6% amongst the dosimeters were found for cones 10, 12.5 and 15 mm, respectively. EBT3 film obtained OF_{EBT} agreed with the MC calculated output factors (dose to water ratio) within 1% for fields over 10 mm in diameter and within 2.2% for 3.77 mm and smaller fields.

6.3.4. $k_{Q_{clin},Q_{msr}}^{f_{clin},f_{msr}}$ correction factors for microDiamond and EFD-3G detectors

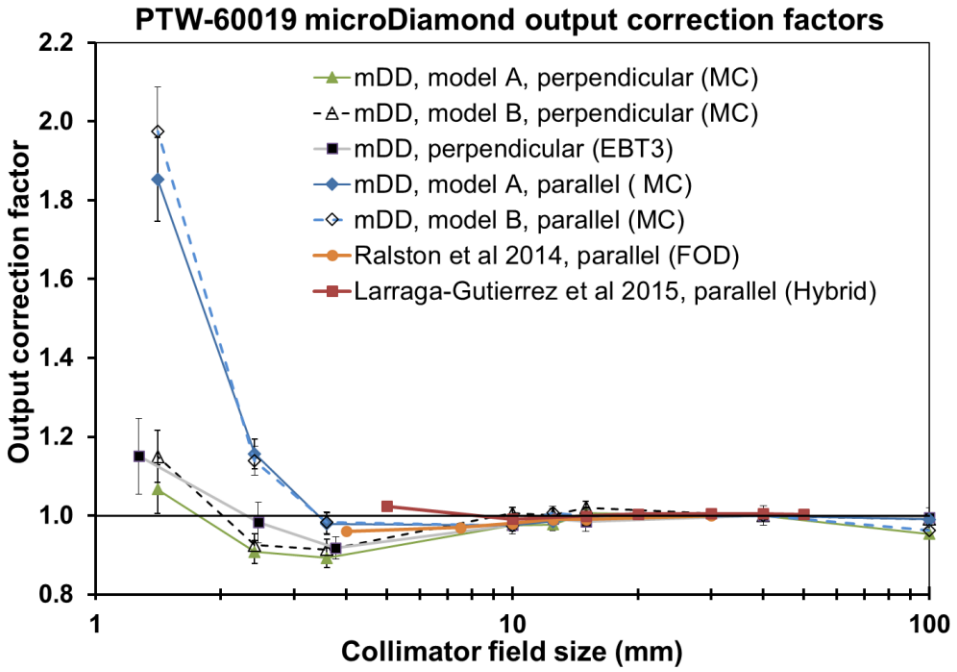

Figure 6.11: PTW-60019 microDiamond detector output correction factors $k_{Q_{clin},Q_{msr}}^{f_{clin},f_{msr}}$ for 1.27-40 mm cones were determined experimentally (using the EBT3 film as the reference detector) as

well as calculated with MC. MicroDiamond $k_{Q_{\mathrm{clin}},Q_{\mathrm{msr}}}^{f_{\mathrm{clin}},f_{\mathrm{msr}}}$ factors were calculated using two detector models, one with the absence (model A) and the other with the presence (model B) of metallic pins, and with two detector orientations. Previous studies by Ralston et al (2014) and Lárraga-Gutiérrez (2015) are added for comparison.

MC calculated and measured $k_{Q_{\mathrm{clin}},Q_{\mathrm{msr}}}^{f_{\mathrm{clin}},f_{\mathrm{msr}}}$ factors for the microDiamond detector are presented in Figure 6.11. Correction factors for microDiamond detector in field sizes of ≥10 mm were small and ranged within 0.989—1.020 and within 0.975—1.010 for perpendicular and parallel orientations respectively. For 1.27, 2.46 and 3.77 mm cones, calculated $k_{Q_{\mathrm{clin}},Q_{\mathrm{msr}}}^{f_{\mathrm{clin}},f_{\mathrm{msr}}}$ factors for the microDiamond detector (model B) in perpendicular orientation were smaller than those calculated for the detector (model B) in parallel orientation by 41.75%, 18.8%, and 7.0%, respectively. The extra metallic pins included in model B had little effect on calculated $k_{Q_{\mathrm{clin}},Q_{\mathrm{msr}}}^{f_{\mathrm{clin}},f_{\mathrm{msr}}}$ factors for all field sizes except the smallest one. For the 1.27 mm field $k_{Q_{clin},Q_{msr}}^{f_{clin},f_{msr}}$ factors for model B of microDiamond detector were ~7% higher than those for model A.

For all investigated fields the microDiamond detector, when setup in perpendicular orientation and rotated such that its electrodes lined up along the beam CAX, produced similar results to the setup with electrodes orthogonal to CAX. This indicates that any asymmetry of the detectors inner component relative to the incident fields had no significant impact on the results.

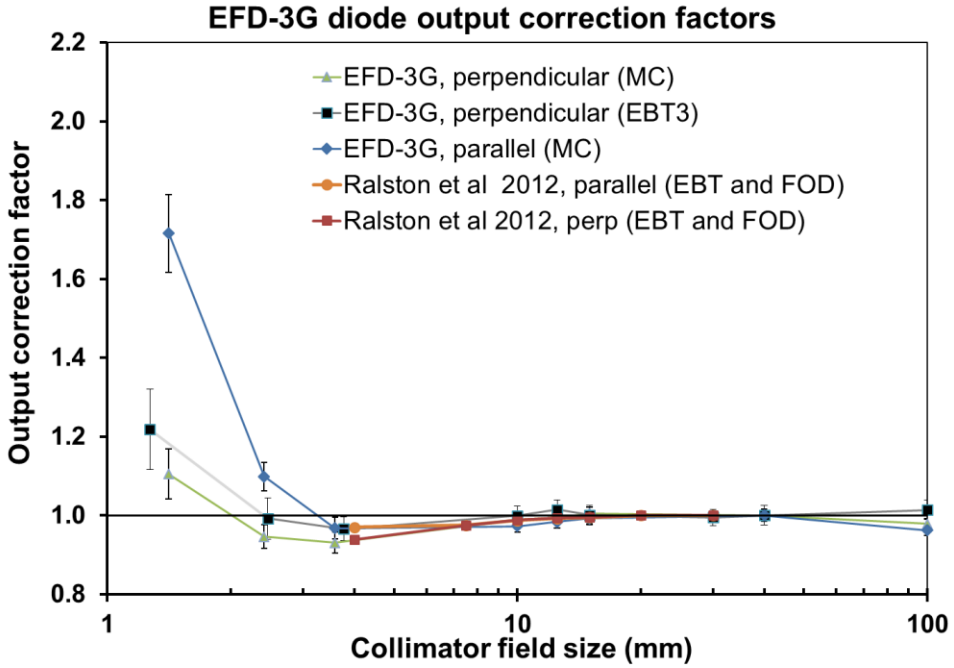

Figure 6.12**:** IBA EFD-3G unshielded diode detector output correction factors $k_{Q_{\text{clin}},Q_{\text{msr}}}^{f_{\text{clin}},f_{\text{msr}}}$ for 1.27- 40 mm cones were determined experimentally (using the EBT3 film as the reference detector) and calculated with MC. EFD-3G $k_{Q_{\text{clin}},Q_{\text{msr}}}^{f_{\text{clin}},f_{\text{msr}}}$ factors were calculated for two detector orientations and were measured using EBT3. Previous results by Ralston *et al* (2012) are added for comparison.

Figure 6.12 shows calculated and measured $k_{Q_{\text{clin}},Q_{\text{msr}}}^{f_{\text{clin}},f_{\text{msr}}}$ factors for the EFD-3G diode detector. The differences between parallel and perpendicular orientations in calculated $k_{Q_{\text{clin}},Q_{\text{msr}}}^{f_{\text{clin}},f_{\text{msr}}}$factors were 35.6%, 13.9%, 3.8%, -1.6%, -1.1% and -1.3% for the 1.27, 2.46, 3.77, 12.5, and 15 mm cones, respectively.

Summary of the measured and calculated $k_{Q_{\text{clin}},Q_{\text{msr}}}^{f_{\text{clin}},f_{\text{msr}}}$ factors is shown in Table 6.4. Agreement between EBT3 and MC derived $k_{Q_{\text{clin}},Q_{\text{msr}}}^{f_{\text{clin}},f_{\text{msr}}}$ factors for microDiamond detector with its stem in the perpendicular orientation was within 3.7% for 3.77 - 15 mm fields. Differences of 2.7% and 5.9% were found for the 1.27 and 2.46 mm fields, respectively. Agreement between EBT3 and MC derived $k_{Q_{\text{clin}},Q_{\text{msr}}}^{f_{\text{clin}},f_{\text{msr}}}$ factors for EFD-3G was less than 3.5% for the 3.77−15 mm fields. For the 1.27 and 2.46 mm fields, differences between measured and derived corrections were 7.5% and 4.7%, respectively.

Table 6.4: $k_{Q_{\mathrm{clin}},Q_{\mathrm{msr}}}^{f_{\mathrm{clin}},f_{\mathrm{msr}}}$ factors were measured and calculated for the PTW-60019 microDiamond and IBA EFD-3G unshielded diode detectors (both in perpendicular orientation) for a range of circular cones. Differences are shown between MC calculated and measured $k_{Q_{\mathrm{clin}},Q_{\mathrm{msr}}}^{f_{\mathrm{clin}},f_{\mathrm{msr}}}$ values for each detector.

Collimator Field Size (mm)	$k_{Q_{\mathrm{clin}},Q_{\mathrm{msr}}}^{f_{\mathrm{clin}},f_{\mathrm{msr}}}$				Relative Differences	
	MC mDD	Measurement mDD	MC EFD	Measurement EFD	*% Diff*$_{\mathrm{mDD}}$	*% Diff*$_{\mathrm{EFD}}$
1.27	1.182	1.151	1.127	1.219	2.7%	-7.5%
2.46	0.924	0.982	0.945	0.992	-5.9%	-4.7%
3.77	0.912	0.918	0.932	0.966	-0.7%	-3.5%
10	0.989	0.977	0.989	0.999	1.2%	-1.0%
12.5	1.001	0.991	0.995	1.014	1.0%	-1.9%
15	1.020	0.984	1.005	1.001	3.7%	0.4%
40	1.000	1.000	1.000	1.000	-	-

6.3.5. Volume averaging

Table 6.5: $P_{\mathrm{vol}}^{\mathrm{det}} = D_{\mathrm{w}}/D_{\mathrm{vol,w}}$ factors calculated for the PTW-60019 microDiamond and IBA EFD-3G unshielded diode detectors in perpendicular and parallel orientations for 1.41-10 mm circular cones. Total estimated uncertainties (type A and B) in the $P_{\mathrm{vol}}^{\mathrm{det}}$ factors are 5%, 2.5%, 2% and 0.8% for 1.41 mm, 2.41 mm, 3.59 mm and the 10 mm fields, respectively.

		Volume averaging correction factor ($P_{\mathrm{vol}}^{\mathrm{det}}$)	
	Collimator field size (mm)	microDiamond	EFD-3G
Perpendicular	**1.41**	1.390	1.316

stem orientation	**2.41**	1.094	1.074
	3.59	1.014	1.007
	10	1.002	1.002
Parallel stem orientation	**1.41**	2.018	1.821
	2.41	1.237	1.179
	3.59	1.041	1.028
	10	1.001	1.000

Table 6.5 shows that volume averaging correction factors are considerably larger for detectors in the parallel orientation and for very small cones (1.41 – 3.59 mm). For microDiamond detector in the parallel orientation irradiated using 1.41 mm, 2.41 mm and the 3.59 mm collimators, $P_{\mathrm{vol}}^{\mathrm{det}}$ factors were 45.2%, 13.1% and 2.7% respectively higher than those with the detector perpendicularly orientated. Similarly, differences in $P_{\mathrm{vol}}^{\mathrm{det}}$ values for EFD-3G in parallel and perpendicular orientations were 38.4%, 9.8% and 2.1% for 1.41 mm, 2.41 mm and the 3.59 mm cones, respectively. MicroDiamond detector $P_{\mathrm{vol}}^{\mathrm{det}}$ factors were found to be larger than those for EFD-3G detector. This is because the microDiamond sensitive volume diameter is larger than that of the EFD-3G detector.

6.3.6. Estimated uncertainties

Estimated uncertainty in measurements

The uncertainties reported in OF_{det} and the correction factors are a quadrature sum of type-A and type-B uncertainties using a one standard deviation confidence interval (1 σ) (BIPM et al., 2008).

Type-A uncertainties were estimated from the standard deviation of three repeated measurements by microDiamond and EFD-3G detectors for each collimator. Type-A uncertainty in microDiamond and EFD-3G detectors measured OF_{det} was estimated to be less than 0.6% for all fields. Type-B uncertainties due to setup and reproducibility were estimated for both detectors from the standard deviation of the results acquired from three setups assembled at different times. Type-B uncertainties were 1.27% for 10 – 40 mm collimators. For 1.27 – 3.77 mm fields, estimated type-B uncertainties were 5.4%–1.9%. Total uncertainty was derived through

summation in quadrature of type-A and type-B uncertainties. Total OF_{det} uncertainty for microDiamond and EFD-3G detectors was found to be in the range 5.5% – 2% for the 1.27 – 40 mm collimators.

Type-A uncertainties in OF_{EBT} were estimated as described in Devic *et al* (2005) and were less than 1.4% for all fields. Type-B uncertainty was estimated considering only the setup and machine output variations and found to be less than 1.5% for fields greater than 10 mm. For the 1.27 – 3.77 mm fields, the estimated type-B uncertainties were 6.2% – 2%. This increase in the type-B uncertainty for small collimators was mainly due to the imperfect alignment of these collimators along the beam axis. EBT3 OF_{EBT} combined uncertainty was 6.4% – 2% for the 1.27 – 40 mm fields.

Similarly, total uncertainty (type A and B) propagated into the $k_{Q_{\text{clin}},Q_{\text{msr}}}^{f_{\text{clin}},f_{\text{msr}}}$ estimate was 8% – 2.5% for the 1.27 – 40 mm fields.

Estimated uncertainty in Monte Carlo calculations

Latent variance (Sempau et al., 2001) originating from the phase spaces provided by Varian for MC calculations has been estimated in Chapter 5. This sets the lower limit on achievable statistical uncertainties (type-A) in MC calculations, that in our simulations ranged within 3.5%–1.5% for 1.27 –3.77 mm collimators. Type-B uncertainties in MC calculations were estimated based on results reported by Francescon *et al* (2011). The overall uncertainties in the calculated field output factors $\Omega_{Q_{\text{clin}},Q_{\text{msr}}}^{f_{\text{clin}},f_{\text{msr}}}$ were 4%, 2.3%, and 1.5% for the 1.27 mm, 2.46 mm and all the other fields respectively. Total estimated uncertainties in the $k_{Q_{\text{clin}},Q_{\text{msr}}}^{f_{\text{clin}},f_{\text{msr}}}$ factors were 5.8%, 3.2%, 2.8% and less than 2% for 1.27 mm, 2.46 mm, 3.77 mm and all the other fields, respectively.

6.4. Discussion

To the best of our knowledge, our study is the first to evaluate $k_{Q_{\text{clin}},Q_{\text{msr}}}^{f_{\text{clin}},f_{\text{msr}}}$ correction factors for microDiamond and EFD-3G (unshielded diode) detectors in very small fields of 1.27 – 3.77 mm diameter and demonstrates over and under-response of these detectors in such fields. In addition, we showed that the magnitude of correction is dependent on detector stem orientation with respect to the beam axis.

In this study $k_{Q_{\text{clin}},Q_{\text{msr}}}^{f_{\text{clin}},f_{\text{msr}}}$ factors were derived using MC for microDiamond detector in different orientations. Previous studies have only focused on investigating the detector response in parallel orientation, and many studies (Chalkley & Heyes, 2014; José Manuel Lárraga-Gutiérrez et al., 2015; Morales et al., 2014) showed that microDiamond detector $k_{Q_{\text{clin}},Q_{\text{msr}}}^{f_{\text{clin}},f_{\text{msr}}}$factors were almost equal to unity for fields of over 4 mm diameter. For 4 – 5 mm fields microDiamond detector over-response by 4% – 5% was measured by Ralston *et al* 2014, Azangwe *et al* 2014, and Underwood *et al* 2015. Barrett and Knill (2016) reported a MC obtained $k_{Q_{\text{clin}},Q_{\text{msr}}}^{f_{\text{clin}},f_{\text{msr}}}$ factor of 0.969 (over-response of 3.1%) for microDiamond in a 4 mm field. Our MC results for a 3.77 mm field with the detector in the same (parallel) orientation demonstrated a smaller over-response of 1.8% ($k_{Q_{\text{clin}},Q_{\text{msr}}}^{f_{\text{clin}},f_{\text{msr}}}$=0.982). Therefore our MC calculated $k_{Q_{\text{clin}},Q_{\text{msr}}}^{f_{\text{clin}},f_{\text{msr}}}$ factor for a similar (3.77 mm) field agreed with results by Ralston *et al* 2014, Azangwe *et al* 2014, Underwood *et al* 2015, Barrett and Knill 2016 to within 1.3% - 3.2%.

While the orientation dependence of correction factors changes insignificantly for the fields of over 5 mm, for smaller fields this dependence is much more pronounced. For the field of 3.77 mm the microDiamond detector in parallel orientation required a considerably smaller correction (0.982) than for the perpendicular orientation (0.915). This is due to a larger volume averaging factor off-setting the detector over-response. For the 1.27 mm cone, the volume averaging contribution dominates in both detector orientations as demonstrated by the $k_{Q_{\text{clin}},Q_{\text{msr}}}^{f_{\text{clin}},f_{\text{msr}}}$ factors being larger than unity.

Francescon *et al* (2017), Coste *et al* (2017) and Andreo *et al* (2016) reported MC calculated $k_{Q_{\text{clin}},Q_{\text{msr}}}^{f_{\text{clin}},f_{\text{msr}}}$ factors for microDiamond in parallel orientation. Reported corrections from these studies (0.987-1.000) agreed with our calculations to within -1.6% to 2% for field sizes of 10 mm and larger. The smallest field they investigated was 5 mm, and the calculated $k_{Q_{\text{clin}},Q_{\text{msr}}}^{f_{\text{clin}},f_{\text{msr}}}$ factor was ~0.995-1.007. For comparison with the above references, our interpolated $k_{Q_{\text{clin}},Q_{\text{msr}}}^{f_{\text{clin}},f_{\text{msr}}}$ factor is ~0.98 for a 5 mm diameter field. Therefore for this field our results agree with Francescon *et al* and Andreo *et al* within uncertainty of our calculations (~ ± 2%). Our calculated microDiamond correction factors compared to results by other studies are shown in Figure 6.13.

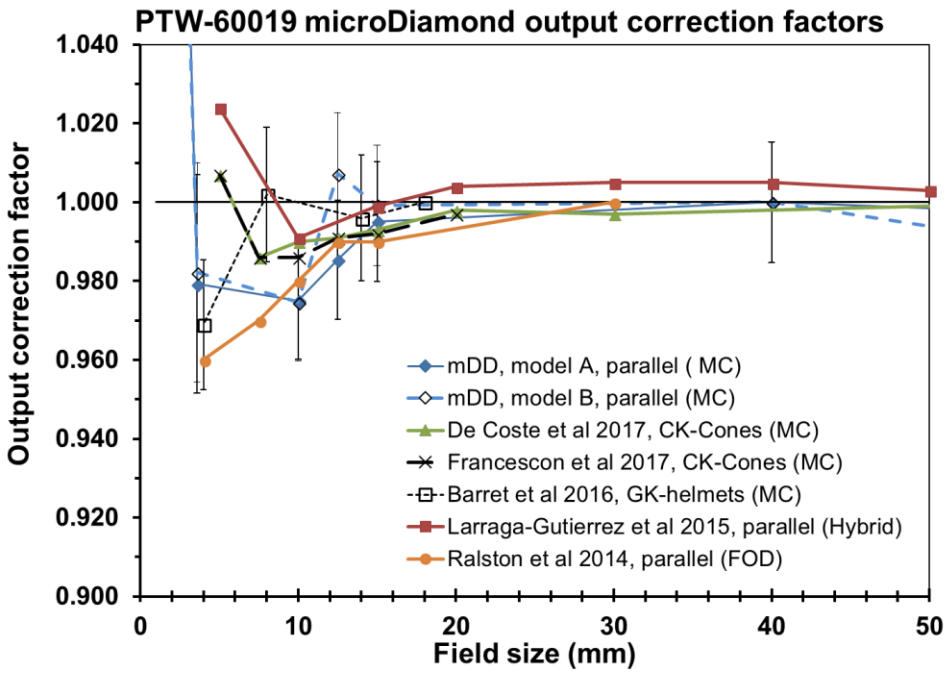

Figure 6.13**:** Comparison of MC obtained PTW-60019 microDiamond detector $k_{Q_{\mathrm{clin}},Q_{\mathrm{msr}}}^{f_{\mathrm{clin}},f_{\mathrm{msr}}}$ factors of figure 6.11 with results published by other studies.

Diode detector over-response has been previously investigated (Bassinet et al., 2013; Paolo Francescon et al., 2008; Lechner, Palmans, Sölkner, Grochowska, & Georg, 2013; Ralston et al., 2012; Scott et al., 2008) and attributed mainly to higher atomic number and density of the diode's sensitive volume (silicon) compared to water. An in-depth interpretation of diode behavior in such fields was provided by Andreo *et al*. (2017), who attributed the over-response to the larger mean excitation energy (*I*-values) of silicon compared to that of water. Scott *et al* (2008) reported over-response of unshielded diode detectors, though its magnitude was lower compared to shielded ones. They reported an over-response of 4.5% by unshielded diode types in 5×5 mm^2 field. Bassinet *et al* (2013) measured small (4–15 mm diameter) fields' *OF*s, using different diode detectors (EDGE diode, PTW 60016, PTW 60017). For 4 mm and 10 mm cones measured *OF*s were higher than the mean *OF* measured by the EBT2 and LiF microcube detectors by 3–6% and 3.3–4.5% respectively. Again, this is consistent with our study, where OF_{det} measured with EFD-3G diode detector for 3.77 mm filed size (in *perpendicular* orientation) was 3.5% and 5.0% higher than EBT3 film OF_{EBT} and MC obtained dose to water ratios, respectively.

The calculated volume correction factors ($P_{\mathrm{vol}}^{\mathrm{det}}$) for both detectors were almost unity for fields greater than 10 mm similarly to previous reports (Pavlos Papaconstadopoulos, Archambault, & Seuntjens, 2017; Ralston et al., 2012, 2014). Ralston et al (2012) found that for the 4-mm cone the volume averaging correction of EFD-3G diode detector used in the parallel orientation was 1.9% higher than when it was perpendicular. Our MC calculated $P_{\mathrm{vol}}^{\mathrm{det}}$ factor for the 3.77 and 2.46 mm fields for the EFD-3G oriented in parallel were 2% and 9.8%, respectively, higher than the detector $P_{\mathrm{vol}}^{\mathrm{det}}$ factor in for a perpendicular orientation. Our MC calculated $P_{\mathrm{vol}}^{\mathrm{det}}$ factor for the microDiamond detector (parallel orientation) was 1.041 for the 3.77 mm cone and is consistent with $P_{\mathrm{vol}}^{\mathrm{det}}$ factor equal to 1.040 as measured by Ralston *et al* (2014) for the 4-mm cone.

This study showed that there were no significant differences between model A and model B of the microDiamond detector for all fields ≥ 2.46 mm. This means that including extra metallic connection pins into the detector model had no effect on the calculated results. In case of 1.27 mm field, $k_{Q_{\mathrm{clin}},Q_{\mathrm{msr}}}^{f_{\mathrm{clin}},f_{\mathrm{msr}}}$ for model B factor was ~7% higher than that for model A. This applies for both parallel and perpendicular detector stem orientations. A possible explanation for this result is that metallic pins included in model B acted as a shield preventing some of the lower energy particles from reaching the active volume and causing a lower detected signal (larger $k_{Q_{\mathrm{clin}},Q_{\mathrm{msr}}}^{f_{\mathrm{clin}},f_{\mathrm{msr}}}$ factor). However, the calculated values of $k_{Q_{\mathrm{clin}},Q_{\mathrm{msr}}}^{f_{\mathrm{clin}},f_{\mathrm{msr}}}$ factors are within the error bars and therefore this result is not definitive.

It is practically convenient to use the microDiamond detector in the perpendicular orientation for obtaining beam OF_{det} in solid water phantoms, and this orientation also provides better spatial resolution. To our knowledge, this is the first paper to report experimental and MC obtained small field (1.27-15 mm diameter) $k_{Q_{\mathrm{clin}},Q_{\mathrm{msr}}}^{f_{\mathrm{clin}},f_{\mathrm{msr}}}$ correction factors for the microDiamond detector in a perpendicular orientation. For the three smallest fields (1.27 mm- 3.77 mm diameter) our MC and experimentally obtained $k_{Q_{\mathrm{clin}},Q_{\mathrm{msr}}}^{f_{\mathrm{clin}},f_{\mathrm{msr}}}$ factors were in agreement with each other to within 5.9% and 7.5% for the microDiamond and the EFD-3G diode detectors, respectively. For other field sizes, the MC calculated and EBT3 film measured $k_{Q_{\mathrm{clin}},Q_{\mathrm{msr}}}^{f_{\mathrm{clin}},f_{\mathrm{msr}}}$ factors were in agreement with each other to within 3.7% and 1.9% for the microDiamond and the EFD diode detectors respectively (Table 6.4).

We can see three main possible reasons for the differences between experimental and MC derived correction factors. Firstly, the MC phase-space used in the calculations may not accurately represent the actual particle fluence for small fields. Secondly, geometry and materials of the sensitive volumes in MC calculations may not accurately represent those in the real

detectors and finally, collimator-detector misalignment could have artificially reduced measured signals resulting in higher correction factors.

The first reason is unlikely to be valid because the agreement, within uncertainty, between EBT3 and MC obtained OF_{det} (both measured and calculated in perturbation-free setting) indicates that the electron source parameters in Varian linac head model, that produced phase-spaces used in this work, were tuned with sufficient accuracy to represent small beams. This agreement also supports MC modeling as well as alignment of the collimators along the beam axis.

In regards to modeling of detector geometries, our results showed that possible difference in the geometry of connection pins in microDiamond detector did not produce a measurable impact on output factors. Andreo *et al* (2016) indicated that the effective measurement volume in microDiamond detector could have been considerably smaller (0.6 mm) than the 2.2 mm diameter stated by the manufacturer in the specifications. Our data do not support such a considerable change in the effective detector size. We evaluated that a reduction of the detector diameter to 0.6 mm would have decreased volume averaging factors by 30% and 8% for 1.27 mm and 2.46 mm diameter collimators respectively and consequently would increase the measured output by the same magnitude. Such OF_{det} change is outside of our estimated measurement uncertainties.

Our EFD-3G detector model did not include any high-density metallic components (as per Cranmer-Sargison *et al* (2012)). According to the findings by Benmakhlouf *et al.* (2016) the particle fluence spectra is mostly perturbed by the high atomic number "extra-cameral" EFD-3G detector components. Based on his findings our calculated factors for the approximate model (with no metallic parts) are expected to be somewhat larger compared to those measured for a real detector. Our MC calculated $k_{Q_{\text{clin}},Q_{\text{msr}}}^{f_{\text{clin}},f_{\text{msr}}}$ factors for the approximate EFD-3G detector model agreed with EBT3 film measured $k_{Q_{\text{clin}},Q_{\text{msr}}}^{f_{\text{clin}},f_{\text{msr}}}$ factors within experimental uncertainty, although they were 7.5% - 3.5% smaller in 1.27 - 3.77 mm fields. Note also that our data were produced for the detector in the perpendicular orientation as compared to the parallel orientation in the study by Benmakhlouf *et al.* We expect that in perpendicular orientation the relative effect of extra-cameral components would be reduced.

The differences between MC and experimentally derived correction factors can probably be attributed to a possible small detector mis-alignment along CAX. The accuracy of the detector alignment in the beam was about 0.1 mm in our measurements, and the possible shift of effective measurement point off-axis by such distance could produce a signal reduction of the magnitude comparable to the observed differences between calculated and measured OF_{det}.

There is also a possibility that MC model derived from the manufacturer's specifications still contains inaccuracies contributing to the difference between measured and calculated $k_{Q_{\text{clin}},Q_{\text{msr}}}^{f_{\text{clin}},f_{\text{msr}}}$ factors. Further investigations with more accurate beam–detector alignment and MC model should be able to reduce uncertainties and improve agreement of the calculated versus measured results.

6.5. Conclusions

PTW-60019 microDiamond and IBA EFD-3G detectors performed well for the fields ≥10 mm. The OF_{det} measured by these detectors agreed to within ~3.5% with field output factors values obtained using MC and EBT3 films. This indicates that required corrections are small for *OF* measured by both detectors in fields ≥10 mm.

In 3.8 mm field the PTW-60019 microDiamond detector over-responded compared to MC calculations and EBT3 measurement. The magnitude of the detector over-response in the perpendicular orientation was greater than for a parallel orientation.

In the smallest (1.27 mm) field the microDiamond detector under-responded compared to MC calculations and EBT3 measurement due to the dominant role of volume averaging effect.

We found that including the metallic connection pins in the microDiamond detector model is not necessary and does not alter the values of $k_{Q_{\text{clin}},Q_{\text{msr}}}^{f_{\text{clin}},f_{\text{msr}}}$ factor in fields larger than 2.46 mm diameter.

There was no difference found in the calculated $k_{Q_{\text{clin}},Q_{\text{msr}}}^{f_{\text{clin}},f_{\text{msr}}}$ factors when the microDiamond detector was rotated around stem axis. This indicates that such detector rotation should have no impact on the OF_{det} measurements in small fields.

This study showed that microDiamond and EFD-3G detectors can be used in very small (1.27-3.77 mm) fields once determined $k_{Q_{\text{clin}},Q_{\text{msr}}}^{f_{\text{clin}},f_{\text{msr}}}$corrections are applied. Expected uncertainty of such measurements will be in the range of 8%-2.5%.

7. Chapter 7
Conclusions

The motivation behind the dissertation was driven by the difficult, yet crucial, dosimetry at non-charge particle equilibrium (CPE) regions. Inaccurate dose assessment in such regions may significantly impact the outcomes of radiotherapy treatments. Standard dosimetry methods, such as ionization chambers, suffer at non-CPE regions. Therefore, advanced methods tailored specifically to suit the investigated non-CPE conditions must be used. The dissertation investigated two non-CPE cases that pose dosimetric challenges: regions near interfaces of different media and dosimetry in small photon fields. Firstly, doses were evaluated using five dosimetric techniques: Monte Carlo (MC), Acuros XB, anisotropic analytical algorithm (AAA), film and MO*Skin* detectors. Film and MO*Skin* detectors are well known for their advantages in such regions (Bilge et al., 2009; I.S. Kwan et al., 2008). Secondly, the detector correction factors were obtained to provide accurate dose measurements in small radiotherapy fields. Along the quest for achieving these objectives, the dissertation also covered different topics that were essential to reach the dissertation goals. These topics included an enhancement to the film dosimetry protocol, as well as the investigation on the latent variances of the Varian TrueBeam phase-spaces.

The dissertation provided a comparative performance evaluation of several advanced dosimeters in heterogeneous phantoms. In this part of the dissertation, two commercial TPS dose calculation algorithms, AcurosXB and AAA, were benchmarked. In the second part, a set of detector specific correction factors for two widely used dosimeters (EFD-3G diode and PTW-60019 microDiamond detectors) were measured using EBT3 films and were calculated using MC method. These correction factors allow accurate dose measurements in small photon fields using these detectors.

7.1. Thesis summary

To achieve the main dissertation objectives, an enhanced film dosimetry protocol was implemented as presented in Chapter 3. GafChromic® EBT2 or EBT3 films were used extensively throughout this research. The film dosimetry process is tedious and time-consuming by itself, not to mention the extra steps implemented to reduce measurement uncertainties. This has motivated the development of a new film calibration approach. In this protocol, the new film dose calibration method was based on PDD tables. The PDD film calibration approach was validated against the traditional calibration approach for its accuracy and efficiency. Film

measurements of known radiation doses (25-400 cGy) were determined using the PDD and the traditional calibration curves. The average relative difference between the known and measured radiation doses predicted by the PDD calibration approach and the traditional calibration one were 1.1% and 1.7%, respectively. Results showed that PDD calibration approach made the dosimetry process more efficient and produced more accurate measurements than the traditional method. Hence, the new developed PDD calibration approach was implemented for our film measurements throughout.

The limitations of using PSFs as a source in the small field dose calculations were investigated in Chapter 5. It is well known that some MC applications are likely to require summing up more PSFs than others depending on the beam energy, field size, and grid resolution of the dose scoring volume. In Chapter 6, the dose calculations had to be performed for very small fields and scoring volumes. The MC statistical uncertainty in these types of calculations is limited by the number of particles (i.e. latent variance) in the used PSFs. There are, however, no guidelines on how many particles are needed in order to achieve acceptable uncertainty in such calculations. This has motivated the work on the quantification of the number of PSFs that are needed for the dose calculations carried out in Chapter 6.

In Chapter 5, the latent variance (LV) of Varian TrueBeam photon phase-space files (PSF) were evaluated, as per Sempau *et al*., for open 10 × 10 cm^2 and small stereotactic fields (down to 1.27 mm diameter). LVs were calculated at different depths in a phantom for various beam energies and phantom grid resolutions. In addition, the number of phase spaces required to be summed up in order to maintain sub-percent LV in MC dose calculations was estimated. For the open 10 × 10 cm^2 fields calculated LVs were greatest at the phantom surface and decreased with depth, until they reached a plateau at a depth of 5 cm. LVs were found to be 0.54%, 0.96%, 0.35%, 0.69% and 0.47% for the 6 MV-FFF, 6 MV, 10 MV-FFF, 10 MV and 15 MV energies, respectively at the depth of 10 cm. For the 6 MV phase-space collimated with cones of 1.27, 2.46, 3.77, 10 mm diameter, the LVs calculated at 1.5 cm depth were 75.6%, 25.4%, 17.6% and 8.0% respectively. Calculated LV for the 2.46 mm cone collimated 6 MV beam were 61.2%, 40.7%, 22.5% in 0.02 × 0.02 × 0.5 cm^3, 0.05 × 0.05 × 0.5 cm^3 and 0.1 × 0.1 × 0.5 cm^3 voxels respectively. Thus, in order to achieve sub-percent LV in open 10 × 10 cm^2 field MC simulations, a single PSF can be used, whereas for small SRS fields (1.27–10 mm) more PSFs (66–8 PSFs) would have to be summed.

In Chapter 4, The performance of five dosimetric methods was compared in heterogeneous phantoms irradiated by 6 and 18 MV beams. MC method was used, along with two versions of AcurosXB, anisotropic analytical algorithm (AAA), EBT2 film, and MOS*kin* dosimeters. Percent depth doses (PDD) were calculated and measured in three heterogeneous phantoms. The first two phantoms were a 30 × 30 × 30 cm^3 solid-water slab that had an air-gap of 20 × 2.5 × 2.35 cm^3. The third phantom consisted of 30 × 30 × 5 cm^3 solid water slabs, two 30

× 30 × 5 cm^3 slabs of lung, and one 30 × 30 × 1 cm^3 solid water slab. AcurosXB, AAA, and MC calculations were within 1% in the regions with particle equilibrium. However, at media interfaces and buildup regions, differences between AcurosXB and MC were in the range of +4.4% to -12.8%. Measurements by MOS*kin* and EBT2 detectors agreed to MC calculations within ~ 2.5%, except for the first centimeter of the buildup region where differences of 4.5% were observed. AAA did not accurately predict the backscatter dose from the high-density heterogeneity. For the third, multilayer lung phantom, 6 MV beam PDDs calculated by all TPS algorithms were within 2% of MC. 18 MV PDDs calculated by two versions of AcurosXB and AAA differed from MC by up to 2.8%, 3.2%, and 6.8%, respectively. MOS*kin* and EBT2 detectors each differed from MC calculations by up to 2.9% and 2.5% for the 6 MV, and by -3.1% and ~ 2% for the 18 MV beams. All dosimetric techniques, except AAA, agreed within 3% in the regions with particle equilibrium. Differences between the dosimetric techniques were larger for the 18 MV than the 6 MV beam. MOS*kin* and EBT2 measurements were in a better agreement with MC than AcurosXB calculations at the interfaces, and they were in a better agreement to each other than to MC. We assume that agreement between MOS*kin* and EBT2 measurements was better than agreement with MC due to thinner detection layers in these detectors compared to MC voxel sizes.

In chapter 6, dose was calculated and measured in small fields using different detectors. The field output factors were calculated and measured using two of the most accurate dose assessment methods (MC and films) in such field sizes. In this study, $k_{Q_{\mathrm{clin}},Q_{\mathrm{msr}}}^{f_{\mathrm{clin}},f_{\mathrm{msr}}}$ factors were obtained for microDiamond and EFD-3G detectors in very small (less than 5 mm) circular fields. Output factors (*OF*'s) of 6 MV beams from TrueBeam linac collimated with 1.27-40 mm diameter cones were measured with EBT3 films, microDiamond and EFD-3G detectors as well as calculated (in water) using Monte Carlo (MC) methods. Based on EBT3 measurements and MC calculations $k_{Q_{\mathrm{clin}},Q_{\mathrm{msr}}}^{f_{\mathrm{clin}},f_{\mathrm{msr}}}$ factors were derived for these detectors. MC calculations were performed for microDiamond detector in parallel and perpendicular orientations relative to the beam axis. Furthermore, $k_{Q_{\mathrm{clin}},Q_{\mathrm{msr}}}^{f_{\mathrm{clin}},f_{\mathrm{msr}}}$ factors were calculated for two microDiamond detector models, differing by the presence or absence of metallic pins. The measured *OF*s agreed within 2.4% for fields ≥10 mm. For the cones of 1.27, 2.46, and 3.77 mm maximum differences were 17.9%, 1.8% and 9.0%, respectively. MC calculated output factors in water agreed with those obtained using EBT3 film within 2.2% for all fields. MC calculated $k_{Q_{\mathrm{clin}},Q_{\mathrm{msr}}}^{f_{\mathrm{clin}},f_{\mathrm{msr}}}$ factors for microDiamond detector in fields ≥10 mm ranged within 0.975-1.020 for perpendicular and parallel orientations. MicroDiamond detector $k_{Q_{\mathrm{clin}},Q_{\mathrm{msr}}}^{f_{\mathrm{clin}},f_{\mathrm{msr}}}$ factors calculated for the 1.27, 2.46 and 3.77 mm fields were 1.974, 1.139 and 0.982 with detector in parallel orientation, and these factors were 1.150, 0.925 and 0.914 in perpendicular orientation. Including metallic pins in the

microDiamond model had little effect on calculated $k_{Q_{\mathrm{clin}},Q_{\mathrm{msr}}}^{f_{\mathrm{clin}},f_{\mathrm{msr}}}$ factors. EBT3 and MC obtained $k_{Q_{\mathrm{clin}},Q_{\mathrm{msr}}}^{f_{\mathrm{clin}},f_{\mathrm{msr}}}$ factors agreed within 3.7% for fields of ≥3.77 mm and within 5.9% for smaller cones. To conclude, microDiamond and EFD-3G detectors can be used in very small (1.27-3.77 mm) fields once $k_{Q_{\mathrm{clin}},Q_{\mathrm{msr}}}^{f_{\mathrm{clin}},f_{\mathrm{msr}}}$ corrections determined in this work are applied. Expected uncertainty of such measurements will be in the range of 8%-2.5%.

Bibliography

Aarup, L. R., Nahum, A. E., Zacharatou, C., Juhler-Nøttrup, T., Knöös, T., Nyström, H., … Korreman, S. S. (2009). The effect of different lung densities on the accuracy of various radiotherapy dose calculation methods: Implications for tumour coverage. *Radiotherapy and Oncology*, *91*(3), 405–414. https://doi.org/10.1016/j.radonc.2009.01.008

Alfonso, R., Andreo, P., Capote, R., Huq, M. S., Kilby, W., Kjäll, P., … Vatnitsky, S. (2008). A new formalism for reference dosimetry of small and nonstandard fields. *Medical Physics*, *35*(11), 5179. https://doi.org/10.1118/1.3005481

Alhakeem, E., & Zavgorodni, S. (2018). Output and $k_{Q_{clin},Q_{msr}}^{f_{clin},f_{msr}}$ correction factors measured and calculated in very small circular fields for microDiamond and EFD-3G detectors. *Physics in Medicine & Biology*, *63*(15), 155002. https://doi.org/10.1088/1361-6560/aacfb2

Alhakeem, Eyad A., AlShaikh, S., Rosenfeld, A. B., & Zavgorodni, S. F. (2015). Comparative evaluation of modern dosimetry techniques near low- and high-density heterogeneities. *Journal of Applied Clinical Medical Physics*, *16*(5), 142–158. https://doi.org/10.1120/jacmp.v16i5.5589

Alhakeem, Eyad Ali, & Zavgorodni, S. F. (2017). Evaluation of latent variances in Monte Carlo dose calculations with varian TrueBeam photon phase-spaces used as a particle source. *Physics in Medicine and Biology*. https://doi.org/10.1088/1361-6560/aa9f39

Almaviva, S., Marinelli, M., Milani, E., Tucciarone, A., Verona-Rinati, G., Consorti, R., … Ciancaglioni, I. (2008). Synthetic single crystal diamond diodes for radiotherapy dosimetry. *Nuclear Instruments and Methods in Physics Research Section A: Accelerators, Spectrometers, Detectors and Associated Equipment*, *594*(2), 273–277. https://doi.org/10.1016/j.nima.2008.06.028

Almond, P. R., Biggs, P. J., Coursey, B. M., Hanson, W. F., Huq, M. S., Nath, R., & Rogers, D. W. O. (1999). AAPM's TG-51 protocol for clinical reference dosimetry of high-energy photon and electron beams. *Medical Physics*, *26*(9), 1847–1870. https://doi.org/10.1118/1.598691

Alshaikh, S., Carolan, M., Petasecca, M., Lerch, M., Metcalfe, P., & Rosenfeld, A. (2014). Direct and pulsed current annealing of p-MOSFET based dosimeter: the "MOSkin." *Australasian Physical & Engineering Sciences in Medicine*, 1–9.

Andreo, P, & Fransson, A. (1989). Stopping-power ratios and their uncertainties for clinical electron beam dosimetry. *Physics in Medicine and Biology*, *34*(12), 1847–1861. https://doi.org/10.1088/0031-9155/34/12/008

Andreo, Pedro, & Benmakhlouf, H. (2017). Role of the density, density effect and mean excitation energy in solid-state detectors for small photon fields. *Physics in Medicine & Biology*, *62*(4), 1518. https://doi.org/10.1088/1361-6560/aa562e

Andreo, Pedro, Medin, J., & Bielajew, A. F. (1998). Constraints of the multiple-scattering theory of Molière in Monte Carlo simulations of the transport of charged particles. *Medical Physics*, *20*(5), 1315–1325. https://doi.org/10.1118/1.596982

Andreo, Pedro, & Palmans, H. (2016). Comment on "Experimental determination of the PTW 60019 microDiamond dosimeter active area and volume" [Med. Phys. 43, 5205–5212 (2016)]. *Medical Physics*, *43*(12), 6667–6667. https://doi.org/10.1118/1.4966023

Andreo, Pedro, Palmans, H., Marteinsdóttir, M., Benmakhlouf, H., & Carlsson-Tedgren, Å. (2016). On the Monte Carlo simulation of small-field micro-diamond detectors for megavoltage photon dosimetry. *Physics in Medicine and Biology*, *61*(1), L1–L10. https://doi.org/10.1088/0031-9155/61/1/L1

Arjomandy, B., Tailor, R., Anand, A., Sahoo, N., Gillin, M., Prado, K., & Vicic, M. (2010). Energy dependence and dose response of Gafchromic EBT2 film over a wide range of photon, electron, and proton beam energies. *Medical Physics*, *37*, 1942. https://doi.org/10.1118/1.3373523

Attix, F. H. (1976). *Introduction to radiological physics and radiation dosimetry*. New York [etc.]: Wiley & Sons.

Azangwe, G., Grochowska, P., Georg, D., Izewska, J., Hopfgartner, J., Lechner, W., … Palmans, H. (2014). Detector to detector corrections: A comprehensive experimental study of detector specific correction factors for beam output measurements for small radiotherapy beams: Detector specific correction factors for small radiotherapy beams. *Medical Physics*, *41*(7), 072103. https://doi.org/10.1118/1.4883795

Barrett, J. C., & Knill, C. (2016). Monte Carlo calculated correction factors for the PTW microDiamond detector in the Gamma Knife-Model C. *Medical Physics*, *43*(3), 1035–1044. https://doi.org/10.1118/1.4940790

Bassinet, C., Huet, C., Derreumaux, S., Brunet, G., Chéa, M., Baumann, M., … Clairand, I. (2013). Small fields output factors measurements and correction factors determination for several detectors for a CyberKnife® and linear accelerators equipped with microMLC and circular cones. *Medical Physics*, *40*(7), 071725. https://doi.org/10.1118/1.4811139

Benmakhlouf, H, Johansson, J., Paddick, I., & Andreo, P. (2015). Monte Carlo calculated and experimentally determined output correction factors for small field detectors in Leksell Gamma Knife Perfexion beams. *Physics in Medicine and Biology*, *60*(10), 3959–3973. https://doi.org/10.1088/0031-9155/60/10/3959

Benmakhlouf, Hamza, & Andreo, P. (2016). Spectral distribution of particle fluence in small field detectors and its implication on small field dosimetry. *Medical Physics*. https://doi.org/10.1002/mp.12042

Benmakhlouf, Hamza, Sempau, J., & Andreo, P. (2014a). Output correction factors for nine small field detectors in 6 MV radiation therapy photon beams: A PENELOPE Monte Carlo study. *Medical Physics*, *41*(4), 041711. https://doi.org/10.1118/1.4868695

Benmakhlouf, Hamza, Sempau, J., & Andreo, P. (2014b). Output correction factors for nine small field detectors in 6 MV radiation therapy photon beams: A PENELOPE Monte Carlo study. *Medical Physics*, *41*(4), 041711. https://doi.org/10.1118/1.4868695

Bielajew, A. F., & Rogers, D. W. O. (1986). Presta: The parameter reduced electron-step transport algorithm for electron monte carlo transport. *Nuclear Instruments and Methods in Physics Research Section B: Beam Interactions with Materials and Atoms*, *18*(1), 165–181. https://doi.org/10.1016/S0168-583X(86)80027-1

Bilge, H., Cakir, A., Okutan, M., & Acar, H. (2009). Surface dose measurements with GafChromic EBT film for 6 and 18MV photon beams. *Physica Medica*, *25*(2), 101–104. https://doi.org/10.1016/j.ejmp.2008.05.001

BIPM, I., IFCC, I., ISO, I., & IUPAP, O. (2008). *Evaluation of measurement data—Guide to the expression of uncertainty in measurement. Joint Committee for Guides in Metrology, JCGM 100: 2008*.

Brualla, L., & Sauerwein, W. (2010). On the efficiency of azimuthal and rotational splitting for Monte Carlo simulation of clinical linear accelerators. *Radiation Physics and Chemistry*, *79*(9), 929–932. https://doi.org/10.1016/j.radphyschem.2010.03.020

Bush, K., Gagne, I. M., Zavgorodni, S., Ansbacher, W., & Beckham, W. (2011). Dosimetric validation of Acuros® XB with Monte Carlo methods for photon dose calculations. *Medical Physics*, *38*(4), 2208. https://doi.org/10.1118/1.3567146

Bush, K, Zavgorodni, S. F., & Beckham, W. A. (2007). Azimuthal particle redistribution for the reduction of latent phase-space variance in Monte Carlo simulations. *Physics in Medicine and Biology*, *52*(14), 4345–4360. https://doi.org/10.1088/0031-9155/52/14/021

Bush, Karl, Zavgorodni, S., & Beckham, W. (2009). Inference of the optimal pretarget electron beam parameters in a Monte Carlo virtual linac model through simulated annealing. *Medical Physics*, *36*(6), 2309–2319.

Butson, M. J., Rozenfeld, A., Mathur, J. N., Carolan, M., Wong, T. P. Y., & Metcalfe, P. E. (1996). A new radiotherapy surface dose detector: The MOSFET. *Medical Physics*, *23*(5), 655–658. https://doi.org/10.1118/1.597702

Carrasco, P., Jornet, N., Duch, M. A., Panettieri, V., Weber, L., Eudaldo, T., … Ribas, M. (2007). Comparison of dose calculation algorithms in slab phantoms with cortical bone equivalent heterogeneities. *Medical Physics*, *34*(8), 3323. https://doi.org/10.1118/1.2750972

Chalkley, A., & Heyes, G. (2014). Evaluation of a synthetic single-crystal diamond detector for relative dosimetry measurements on a CyberKnife™. *The British Journal of Radiology*, *87*(1035), 20130768. https://doi.org/10.1259/bjr.20130768

Chang, D. S., Lasley, F. D., Das, I. J., Mendonca, M. S., & Dynlacht, J. R. (2014). *Basic Radiotherapy Physics and Biology*. Cham: Springer International Publishing. https://doi.org/10.1007/978-3-319-06841-1

Chetty, I. J., Curran, B., Cygler, J. E., DeMarco, J. J., Ezzell, G., Faddegon, B. A., … Siebers, J. V. (2007). Report of the AAPM Task Group No. 105: Issues associated with clinical implementation of Monte Carlo-based photon and electron external beam treatment planning. *Medical Physics*, *34*(12), 4818. https://doi.org/10.1118/1.2795842

Cheung, T., Butson, M. J., & Yu, P. K. N. (2006). Measurement of high energy x-ray beam penumbra with Gafchromic™ EBT radiochromic film. *Medical Physics*, *33*(8), 2912. https://doi.org/10.1118/1.2218318

Chow, J. C. L., Jiang, R., & Leung, M. K. K. (2011). Dosimetry of oblique tangential photon beams calculated by superposition/convolution algorithms: a Monte Carlo evaluation. *Journal of Applied Clinical Medical Physics / American College of Medical Physics*, *12*(1), 3424.

Ciancaglioni, I., Marinelli, M., Milani, E., Prestopino, G., Verona, C., Verona-Rinati, G., … De Notaristefani, F. (2012). Dosimetric characterization of a synthetic single crystal diamond detector in clinical radiation therapy small photon beams. *Medical Physics*, *39*(7), 4493. https://doi.org/10.1118/1.4729739

Coste, V. D., Francescon, P., Marinelli, M., Masi, L., Paganini, L., Maria Pimpinella, … Gianluca Verona-Rinati. (2017). Is the PTW 60019 microDiamond a suitable candidate for small field reference dosimetry? *Physics in Medicine & Biology*, *62*(17), 7036. https://doi.org/10.1088/1361-6560/aa7e59

Cranmer-Sargison, G, Weston, S., Evans, J. A., Sidhu, N. P., & Thwaites, D. I. (2012). Monte Carlo modelling of diode detectors for small field MV photon dosimetry: detector model simplification and the sensitivity of correction factors to source parameterization. *Physics*

in Medicine and Biology, *57*(16), 5141–5153. https://doi.org/10.1088/0031-9155/57/16/5141

Cranmer-Sargison, Gavin, Charles, P. H., Trapp, J. V., & Thwaites, D. I. (2013). A methodological approach to reporting corrected small field relative outputs. *Radiotherapy and Oncology*, *109*(3), 350–355. https://doi.org/10.1016/j.radonc.2013.10.002

Cronholm, R. O., & Behrens, C. F. (2013). OC-0436: On the latent variance of the vendor supplied TrueBeam phase space files. *Radiotherapy and Oncology*, *106*, S168.

Das, I. J., Ding, G. X., & Ahnesjö, A. (2008). Small fields: Nonequilibrium radiation dosimetry. *Medical Physics*, *35*(1), 206. https://doi.org/10.1118/1.2815356

Devic, S., Seuntjens, J., Abdel-Rahman, W., Evans, M., Olivares, M., Podgorsak, E. B., … Soares, C. G. (2006). Accurate skin dose measurements using radiochromic film in clinical applications. *Medical Physics*, *33*, 1116. https://doi.org/10.1118/1.2179169

Devic, Slobodan, Aldelaijan, S., Mohammed, H., Tomic, N., Liang, L.-H., DeBlois, F., & Seuntjens, J. (2010). Absorption spectra time evolution of EBT-2 model GAFCHROMIC^{TM} film. *Medical Physics*, *37*(5), 2207. https://doi.org/10.1118/1.3378675

Devic, Slobodan, Seuntjens, J., Hegyi, G., Podgorsak, E. B., Soares, C. G., Kirov, A. S., … Elizondo, A. (2004). Dosimetric properties of improved GafChromic films for seven different digitizers. *Medical Physics*, *31*(9), 2392. https://doi.org/10.1118/1.1776691

Devic, Slobodan, Seuntjens, J., Sham, E., Podgorsak, E. B., Schmidtlein, C. R., Kirov, A. S., & Soares, C. G. (2005). Precise radiochromic film dosimetry using a flat-bed document scanner. *Medical Physics*, *32*(7), 2245. https://doi.org/10.1118/1.1929253

Dieterich, S., & Sherouse, G. W. (2011). Experimental comparison of seven commercial dosimetry diodes for measurement of stereotactic radiosurgery cone factors. *Medical Physics*, *38*(7), 4166. https://doi.org/10.1118/1.3592647

Ding, G. X., Duggan, D. M., Lu, B., Hallahan, D. E., Cmelak, A., Malcolm, A., … Coffey, C. W. (2007). Impact of inhomogeneity corrections on dose coverage in the treatment of lung cancer using stereotactic body radiation therapy. *Medical Physics*, *34*(7), 2985. https://doi.org/10.1118/1.2745923

Failla, G. A., Wareing, T., Archambault, Y., & Thompson, S. (2010). Acuros XB advanced dose calculation for the Eclipse treatment planning system. *Varian Medical Systems*.

Ferreira, B. C., Lopes, M. C., & Capela, M. (2009). Evaluation of an Epson flatbed scanner to read Gafchromic EBT films for radiation dosimetry. *Physics in Medicine and Biology*, *54*(4), 1073–1085. https://doi.org/10.1088/0031-9155/54/4/017

Fix, M. K., Keall, P. J., Dawson, K., & Siebers, J. V. (2004). Monte Carlo source model for photon beam radiotherapy: photon source characteristics. *Medical Physics*, *31*(11), 3106. https://doi.org/10.1118/1.1803431

Fogliata, A., Nicolini, G., Clivio, A., Vanetti, E., & Cozzi, L. (2011). Accuracy of Acuros XB and AAA dose calculation for small fields with reference to RapidArc® stereotactic treatments. *Medical Physics*, *38*, 6228. https://doi.org/10.1118/1.3654739

Fogliata, A., Nicolini, G., Clivio, A., Vanetti, E., Mancosu, P., & Cozzi, L. (2011). Dosimetric validation of the Acuros XB Advanced Dose Calculation algorithm: fundamental characterization in water. *Physics in Medicine and Biology*, *56*(6), 1879–1904. https://doi.org/10.1088/0031-9155/56/6/022

Francescon, P., Cora, S., & Satariano, N. (2011). Calculation of k[sub Q[sub clin],Q[sub msr]][sup f[sub clin],f[sub msr]] for several small detectors and for two linear accelerators using Monte Carlo simulations. *Medical Physics*, *38*(12), 6513. https://doi.org/10.1118/1.3660770

Francescon, P., Kilby, W., Noll, J. M., Masi, L., Satariano, N., & Russo, S. (2017). Monte Carlo simulated corrections for beam commissioning measurements with circular and MLC shaped fields on the CyberKnife M6 System: a study including diode, microchamber, point scintillator, and synthetic microdiamond detectors. *Physics in Medicine & Biology*, *62*(3), 1076. https://doi.org/10.1088/1361-6560/aa5610

Francescon, Paolo, Cora, S., & Cavedon, C. (2008). Total scatter factors of small beams: A multidetector and Monte Carlo study. *Medical Physics*, *35*(2), 504. https://doi.org/10.1118/1.2828195

Gagné, I. M., & Zavgorodni, S. (2007). Evaluation of the analytical anisotropic algorithm in an extreme water-lung interface phantom using Monte Carlo dose calculations. *Journal of Applied Clinical Medical Physics / American College of Medical Physics*, *8*(1), 33–46.

Gete, E., Duzenli, C., Milette, M.-P., Mestrovic, A., Hyde, D., Bergman, A. M., & Teke, T. (2013). A Monte Carlo approach to validation of FFF VMAT treatment plans for the TrueBeam linac. *Medical Physics*, *40*(2), 021707. https://doi.org/10.1118/1.4773883

Han, T., Followill, D., Mikell, J., Repchak, R., Molineu, A., Howell, R., … Mourtada, F. (2013). Dosimetric impact of Acuros XB deterministic radiation transport algorithm for heterogeneous dose calculation in lung cancer. *Medical Physics*, *40*(5), 051710. https://doi.org/10.1118/1.4802216

Han, T., Mikell, J. K., Salehpour, M., & Mourtada, F. (2011). Dosimetric comparison of Acuros XB deterministic radiation transport method with Monte Carlo and model-based convolution methods in heterogeneous media. *Medical Physics*, *38*(5), 2651. https://doi.org/10.1118/1.3582690

Han, T., Mourtada, F., Kisling, K., Mikell, J., Followill, D., & Howell, R. (2012). Experimental validation of deterministic Acuros XB algorithm for IMRT and VMAT dose calculations with the Radiological Physics Center's head and neck phantom. *Medical Physics*, *39*(4), 2193. https://doi.org/10.1118/1.3692180

Hardcastle, N., Cutajar, D. L., Metcalfe, P. E., Lerch, M. L., Perevertaylo, V. L., Tomé, W. A., & Rosenfeld, A. B. (2010). In vivo real-time rectal wall dosimetry for prostate radiotherapy. *Physics in Medicine and Biology*, *55*(13), 3859.

Hardcastle, N., Soisson, E., Metcalfe, P., Rosenfeld, A. B., & Tomé, W. A. (2008). Dosimetric verification of helical tomotherapy for total scalp irradiation. *Medical Physics*, *35*(11), 5061. https://doi.org/10.1118/1.2996288

Heydarian, M., Hoban, P. W., Beckham, W. A., Borchardt, I. M., & Beddoe, A. H. (1993). Evaluation of a PTW diamond detector for electron beam measurements. *Physics in Medicine & Biology*, *38*(8), 1035. https://doi.org/10.1088/0031-9155/38/8/002

Hoban, P. W., Heydarian, M., Beckham, W. A., & Beddoe, A. H. (1994). Dose rate dependence of a PTW diamond detector in the dosimetry of a 6 MV photon beam. *Physics in Medicine & Biology*, *39*(8), 1219. https://doi.org/10.1088/0031-9155/39/8/003

Hoffmann, L., Jørgensen, M.-B. K., Muren, L. P., & Petersen, J. B. B. (2012). Clinical validation of the Acuros XB photon dose calculation algorithm, a grid-based Boltzmann equation solver. *Acta Oncologica*, *51*(3), 376–385. https://doi.org/10.3109/0284186X.2011.629209

Kairn, T., Hardcastle, N., Kenny, J., Meldrum, R., Tomé, W. A., & Aland, T. (2011). EBT2 radiochromic film for quality assurance of complex IMRT treatments of the prostate: micro-collimated IMRT, RapidArc, and TomoTherapy. *Australasian Physical & Engineering Sciences in Medicine*, *34*(3), 333–343. https://doi.org/10.1007/s13246-011-0087-z

Kan, M. W. K., Leung, L. H. T., So, R. W. K., & Yu, P. K. N. (2013). Experimental verification of the Acuros XB and AAA dose calculation adjacent to heterogeneous media for IMRT and RapidArc of nasopharygeal carcinoma. *Medical Physics*, *40*(3), 031714. https://doi.org/10.1118/1.4792308

Kan, M. W. K., Leung, L. H. T., & Yu, P. K. N. (2012). Verification and dosimetric impact of Acuros XB algorithm on intensity modulated stereotactic radiotherapy for locally persistent nasopharyngeal carcinoma. *Medical Physics*, *39*(8), 4705. https://doi.org/10.1118/1.4736819

Kan, M. W. K., Yu, P. K. N., & Leung, L. H. T. (2013). A Review on the Use of Grid-Based Boltzmann Equation Solvers for Dose Calculation in External Photon Beam Treatment

Planning. *BioMed Research International*, *2013*, 1–10. https://doi.org/10.1155/2013/692874

Kawrakow, I. (2000). Accurate condensed history Monte Carlo simulation of electron transport. I. EGSnrc, the new EGS4 version. *Medical Physics*, *27*(3), 485–498. https://doi.org/10.1118/1.598917

Kawrakow, Iwan. (2001). The EGSnrc code system, Monte Carlo simulation of electron and photon transport. *NRCC Report Pirs-701*.

Kelly, A., Hardcastle, N., Metcalfe, P., Cutajar, D., Quinn, A., Foo, K., … Rosenfeld, A. (2011). Surface dosimetry for breast radiotherapy in the presence of immobilization cast material. *Physics in Medicine and Biology*, *56*(4), 1001–1013. https://doi.org/10.1088/0031-9155/56/4/008

Khan, F. M. (2003). *The Physics of radiation therapy*. Baltimore: Williams & Wilkins.

Koch, H. W., & Motz, J. W. (1959). Bremsstrahlung Cross-Section Formulas and Related Data. *Reviews of Modern Physics*, *31*(4), 920–955. https://doi.org/10.1103/RevModPhys.31.920

Kroon, P. S., Hol, S., & Essers, M. (2013). Dosimetric accuracy and clinical quality of Acuros XB and AAA dose calculation algorithm for stereotactic and conventional lung volumetric modulated arc therapy plans. *Radiation Oncology*, *8*(1), 149. https://doi.org/10.1186/1748-717X-8-149

Kwan, Ian S. (2009). Characterization of the performance of the new MOSkin dosimeter as a quality assurance tool for pulsed dose-rate (PDR) prostate brachytherapy, and the effect of rectal heterogeneity on the dose delivered to the rectal wall.

Kwan, I.S., Rosenfeld, A. B., Qi, Z. Y., Wilkinson, D., Lerch, M. L. F., Cutajar, D. L., … Perevertaylo, V. L. (2008). Skin dosimetry with new MOSFET detectors. *Proceedings of the 15th Solid State Dosimetry (SSD15)*, *43*(2–6), 929–932. https://doi.org/10.1016/j.radmeas.2007.12.052

Lárraga-Gutiérrez, José M. (2014). Calculation of beam quality correction factors for EBT3 radiochromic film. *Physica Medica: European Journal of Medical Physics*, *30*, e62. https://doi.org/10.1016/j.ejmp.2014.07.186

Lárraga-Gutiérrez, José Manuel, Ballesteros-Zebadúa, P., Rodríguez-Ponce, M., García-Garduño, O. A., & de la Cruz, O. O. G. (2015). Properties of a commercial PTW-60019 synthetic diamond detector for the dosimetry of small radiotherapy beams. *Physics in Medicine and Biology*, *60*(2), 905–924. https://doi.org/10.1088/0031-9155/60/2/905

Laub, W. U., & Crilly, R. (2014). Clinical radiation therapy measurements with a new commercial synthetic single crystal diamond detector. *Journal of Applied Clinical Medical Physics*, *15*(6), 92–102. https://doi.org/10.1120/jacmp.v15i6.4890

Lechner, W., Palmans, H., Sölkner, L., Grochowska, P., & Georg, D. (2013). Detector comparison for small field output factor measurements in flattening filter free photon beams. *Radiotherapy and Oncology*, *109*(3), 356–360. https://doi.org/10.1016/j.radonc.2013.10.022

Lettmaier, S. (2014). Radiosurgery in trigeminal neuralgia. *Physica Medica*, *30*(5), 592–595. https://doi.org/10.1016/j.ejmp.2014.05.006

Lloyd, S. A. M., & Ansbacher, W. (2013). Evaluation of an analytic linear Boltzmann transport equation solver for high-density inhomogeneities. *Medical Physics*, *40*(1), 011707. https://doi.org/10.1118/1.4769419

Luo, G.-W., Qi, Z.-Y., Deng, X.-W., & Rosenfeld, A. (2014). Investigation of a pulsed current annealing method in reusing MOSFET dosimeters for in vivo IMRT dosimetry. *Medical Physics*, *41*(5), 051710.

Lynch, B. D., Kozelka, J., Ranade, M. K., Li, J. G., Simon, W. E., & Dempsey, J. F. (2006). Important considerations for radiochromic film dosimetry with flatbed CCD scanners and EBT GAFCHROMIC[sup ®] film. *Medical Physics*, *33*(12), 4551. https://doi.org/10.1118/1.2370505

Mandapaka, A. K., Ghebremedhin, A., Patyal, B., Marinelli, M., Prestopino, G., Verona, C., & Verona-Rinati, G. (2013). Evaluation of the dosimetric properties of a synthetic single crystal diamond detector in high energy clinical proton beams. *Medical Physics*, *40*(12), n/a-n/a. https://doi.org/10.1118/1.4828777

Marinelli, M., Prestopino, G., Verona, C., & Verona-Rinati, G. (2016a). Experimental determination of the PTW 60019 microDiamond dosimeter active area and volume. *Medical Physics*, *43*(9), 5205–5212. https://doi.org/10.1118/1.4961402

Marinelli, M., Prestopino, G., Verona, C., & Verona-Rinati, G. (2016b). Response to "Comment on 'Experimental determination of the PTW 60019 microDiamond dosimeter active area and volume' " [Med. Phys. 43, 6667 (2016)]. *Medical Physics*, *43*(12), 6668–6668. https://doi.org/10.1118/1.4966024

Marsolat, F., Tromson, D., Tranchant, N., Pomorski, M., Le Roy, M., Donois, M., … Bergonzo, P. (2013). A new single crystal diamond dosimeter for small beam: comparison with different commercial active detectors. *Physics in Medicine and Biology*, *58*(21), 7647–7660. https://doi.org/10.1088/0031-9155/58/21/7647

Martišíková, M., Ackermann, B., & Jäkel, O. (2008). Analysis of uncertainties in Gafchromic® EBT film dosimetry of photon beams. *Physics in Medicine and Biology*, *53*(24), 7013–7027. https://doi.org/10.1088/0031-9155/53/24/001

Morales, J. E., Crowe, S. B., Hill, R., Freeman, N., & Trapp, J. V. (2014). Dosimetry of cone-defined stereotactic radiosurgery fields with a commercial synthetic diamond detector: Dosimetry of SRS field using synthetic diamond detector. *Medical Physics*, *41*(11), 111702. https://doi.org/10.1118/1.4895827

Motz, J. W., Olsen, H. A., & Koch, H. W. (1969). Pair Production by Photons. *Reviews of Modern Physics*, *41*(4), 581–639. https://doi.org/10.1103/RevModPhys.41.581

Nelson, W. R., Hirayama, H., & Rogers, D. W. (1985). *EGS4 code system*. Stanford Linear Accelerator Center, Menlo Park, CA (USA).

Novotny Josef, Bhatnagar Jagdish P., Quader Mubina A., Bednarz Greg, Lunsford L. Dade, & Huq M. Saiful. (2009). Measurement of relative output factors for the 8 and 4 mm collimators of Leksell Gamma Knife Perfexion by film dosimetry. *Medical Physics*, *36*(5), 1768–1774. https://doi.org/10.1118/1.3113904

Ojala, J., Kapanen, M., Sipilä, P., Hyödynmaa, S., & Pitkänen, M. (2014). The accuracy of Acuros XB algorithm for radiation beams traversing a metallic hip implant — comparison with measurements and Monte Carlo calculations. *Journal of Applied Clinical Medical Physics; Vol 15, No 5 (2014)*. Retrieved from http://www.jacmp.org/index.php/jacmp/article/view/4912

Palmans, H., Andreo, P., Christaki, K., Huq, M. S., & Seuntjens, J. (2017). Dosimetry of small static fields used in external beam radiotherapy: an IAEA-AAPM international code of practice for reference and relative dose determination. *International Atomic Energy Agency, Vienna*.

Papaconstadopoulos, P, Tessier, F., & Seuntjens, J. (2014). On the correction, perturbation and modification of small field detectors in relative dosimetry. *Physics in Medicine and Biology*, *59*(19), 5937–5952. https://doi.org/10.1088/0031-9155/59/19/5937

Papaconstadopoulos, Pavlos, Archambault, L., & Seuntjens, J. (2017). Experimental investigation on the accuracy of plastic scintillators and of the spectrum discrimination method in small photon fields. *Medical Physics*, *44*(2), 654–664. https://doi.org/10.1002/mp.12064

Pimpinella, M., Ciancaglioni, I., Consorti, R., Venanzio, C. D., Guerra, A. S., Petrucci, A., … Verona-Rinati, G. (2012). A synthetic diamond detector as transfer dosimeter for D_w measurements in photon beams with small field sizes. *Metrologia*, *49*(5), S207–S210. https://doi.org/10.1088/0026-1394/49/5/S207

Qi, Z.-Y., Deng, X.-W., Cao, X., Huang, S.-M., Lerch, M., & Rosenfeld, A. (2012). A real-time in vivo dosimetric verification method for high-dose rate intracavitary brachytherapy of nasopharyngeal carcinoma. *Medical Physics*, *39*(11), 6757–6763.

Qi, Z.-Y., Deng, X.-W., Huang, S.-M., Shiu, A., Lerch, M., Metcalfe, P., … Kron, T. (2011). Real-Time< i> In Vivo</i> Dosimetry With MOSFET Detectors in Serial Tomotherapy for Head and Neck Cancer Patients. *International Journal of Radiation Oncology* Biology* Physics*, *80*(5), 1581–1588.

Qi, Z.-Y., Deng, X.-W., Huang, S.-M., Zhang, L., He, Z.-C., Allen Li, X., … Rosenfeld, A. (2009). In vivo verification of superficial dose for head and neck treatments using intensity-modulated techniques. *Medical Physics*, *36*(1), 59. https://doi.org/10.1118/1.3030951

Quinn, A., Holloway, L., Cutajar, D., Hardcastle, N., Rosenfeld, A., & Metcalfe, P. (2011). Megavoltage cone beam CT near surface dose measurements: potential implications for breast radiotherapy. *Medical Physics*, *38*(11), 6222–6227.

Ralston, A., Liu, P., Warrener, K., McKenzie, D., & Suchowerska, N. (2012). Small field diode correction factors derived using an air core fibre optic scintillation dosimeter and EBT2 film. *Physics in Medicine and Biology*, *57*(9), 2587–2602. https://doi.org/10.1088/0031-9155/57/9/2587

Ralston, A., Tyler, M., Liu, P., McKenzie, D., & Suchowerska, N. (2014). Over-response of synthetic microDiamond detectors in small radiation fields. *Physics in Medicine and Biology*, *59*(19), 5873–5881. https://doi.org/10.1088/0031-9155/59/19/5873

Ramani, R., Russell, S., & O'Brien, P. (1997). Clinical dosimetry using mosfets. *International Journal of Radiation Oncology*Biology*Physics*, *37*(4), 959–964. https://doi.org/10.1016/S0360-3016(96)00600-1

Rana, S. (2014). Clinical dosimetric impact of Acuros XB and analytical anisotropic algorithm (AAA) on real lung cancer treatment plans : review. *International Journal of Cancer Therapy and Oncology*, *2*(1), 02019. https://doi.org/10.14319/ijcto.0201.9

Rana, S., & Rogers, K. (2013). Dosimetric evaluation of Acuros XB dose calculation algorithm with measurements in predicting doses beyond different air gap thickness for smaller and larger field sizes. *Journal of Medical Physics*, *38*(1), 9. https://doi.org/10.4103/0971-6203.106600

Richley, L., John, A. C., Coomber, H., & Fletcher, S. (2010). Evaluation and optimization of the new EBT2 radiochromic film dosimetry system for patient dose verification in radiotherapy. *Physics in Medicine and Biology*, *55*(9), 2601–2617. https://doi.org/10.1088/0031-9155/55/9/012

Rogers, D. W. O. (2006). Fifty years of Monte Carlo simulations for medical physics. *Physics in Medicine and Biology*, *51*(13), R287–R301. https://doi.org/10.1088/0031-9155/51/13/R17

Rogers, D. W. O., Walters, B., & Kawrakow, I. (2009). BEAMnrc users manual. *NRC Report PIRS*, *509*, 12.

Saur, S., & Frengen, J. (2008). GafChromic EBT film dosimetry with flatbed CCD scanner: A novel background correction method and full dose uncertainty analysis. *Medical Physics*, *35*(7), 3094. https://doi.org/10.1118/1.2938522

Scott, A. J. D., Nahum, A. E., & Fenwick, J. D. (2008). Using a Monte Carlo model to predict dosimetric properties of small radiotherapy photon fields. *Medical Physics*, *35*(10), 4671. https://doi.org/10.1118/1.2975223

Seco, J., & Verhaegen, F. (2013). *Monte Carlo techniques in radiation therapy*. CRC press.

Sempau, J., Sánchez-Reyes, A., Salvat, F., Tahar, H. O. ben, Jiang, S. B., & Fernández-Varea, J. M. (2001). Monte Carlo simulation of electron beams from an accelerator head using PENELOPE. *Physics in Medicine and Biology*, *46*(4), 1163–1186. https://doi.org/10.1088/0031-9155/46/4/318

Siebers, J. V., Keall, P. J., Nahum, A. E., & Mohan, R. (2000). Converting absorbed dose to medium to absorbed dose to water for Monte Carlo based photon beam dose calculations. *Physics in Medicine and Biology*, *45*(4), 983–995.

Sievinen, J., Ulmer, W., & Kaissl, W. (2005). AAA photon dose calculation in Eclipse. *Varian Documentation RAD B*, *7170*, 2005.

Stathakis, S. (2012). Accuracy of the Small Field Dosimetry Using the Acuros XB Dose Calculation Algorithm within and beyond Heterogeneous Media for 6 MV Photon Beams. *International Journal of Medical Physics,Clinical Engineering and Radiation Oncology*, *01*(03), 78–87. https://doi.org/10.4236/ijmpcero.2012.13011

Suplee, C. (2009, September 17). XCOM: Photon Cross Sections Database. Retrieved October 10, 2017, from https://www.nist.gov/pml/xcom-photon-cross-sections-database

Teke, T., Duzenli, C., Bergman, A., Viel, F., Atwal, P., & Gete, E. (2015). Monte Carlo validation of the TrueBeam 10XFFF phase–space files for applications in lung SABR. *Medical Physics*, *42*(12), 6863–6874. https://doi.org/10.1118/1.4935144

Tillikainen, L., Siljamäki, S., Helminen, H., Alakuijala, J., & Pyyry, J. (2007). Determination of parameters for a multiple-source model of megavoltage photon beams using optimization methods. *Physics in Medicine and Biology*, *52*(5), 1441–1467. https://doi.org/10.1088/0031-9155/52/5/015

Tyler, M., Liu, P. Z. Y., Chan, K. W., Ralston, A., McKenzie, D. R., Downes, S., & Suchowerska, N. (2013). Characterization of small-field stereotactic radiosurgery beams with modern detectors. *Physics in Medicine and Biology*, *58*(21), 7595–7608. https://doi.org/10.1088/0031-9155/58/21/7595

Ulmer, W., & Kaissl, W. (2003). The inverse problem of a Gaussian convolution and its application to the finite size of the measurement chambers/detectors in photon and proton dosimetry. *Physics in Medicine and Biology*, *48*(6), 707–727. https://doi.org/10.1088/0031-9155/48/6/302

Ulmer, W., Pyyry, J., & Kaissl, W. (2005). A 3D photon superposition/convolution algorithm and its foundation on results of Monte Carlo calculations. *Physics in Medicine and Biology*, *50*(8), 1767–1790. https://doi.org/10.1088/0031-9155/50/8/010

Underwood, T. S. A., Rowland, B. C., Ferrand, R., & Vieillevigne, L. (2015). Application of the Exradin W1 scintillator to determine Ediode 60017 and microDiamond 60019 correction factors for relative dosimetry within small MV and FFF fields. *Physics in Medicine and Biology*, *60*(17), 6669–6683. https://doi.org/10.1088/0031-9155/60/17/6669

Van Esch, A., Tillikainen, L., Pyykkonen, J., Tenhunen, M., Helminen, H., Siljamäki, S., … Huyskens, D. P. (2006). Testing of the analytical anisotropic algorithm for photon dose calculation. *Medical Physics*, *33*(11), 4130. https://doi.org/10.1118/1.2358333

Vassiliev, O. N., Wareing, T. A., McGhee, J., Failla, G., Salehpour, M. R., & Mourtada, F. (2010). Validation of a new grid-based Boltzmann equation solver for dose calculation in radiotherapy with photon beams. *Physics in Medicine and Biology*, *55*(3), 581–598. https://doi.org/10.1088/0031-9155/55/3/002

Verhaegen, F., & Seuntjens, J. (2003). Monte Carlo modelling of external radiotherapy photon beams. *Physics in Medicine and Biology*, *48*(21), R107–R164. https://doi.org/10.1088/0031-9155/48/21/R01

Walters, B., Kawrakow, I., & Rogers, D. W. O. (2005). DOSXYZnrc users manual. *NRC Report PIRS*, *794*.

Walters, B. R. B., Kawrakow, I., & Rogers, D. W. O. (2002). History by history statistical estimators in the BEAM code system. *Medical Physics*, *29*(12), 2745–2752.

Wang, L. L. W., & Rogers, D. W. O. (2007). Monte Carlo study of Si diode response in electron beams. *Medical Physics*, *34*(5), 1734. https://doi.org/10.1118/1.2722720

Wilcox, E. E., & Daskalov, G. M. (2007). Evaluation of GAFCHROMIC® EBT film for CyberKnife® dosimetry. *Medical Physics*, *34*(6), 1967. https://doi.org/10.1118/1.2734384

Wulff, J., Zink, K., & Kawrakow, I. (2008a). Efficiency improvements for ion chamber calculations in high energy photon beams. *Medical Physics*, *35*(4), 1328. https://doi.org/10.1118/1.2874554

Wulff, J., Zink, K., & Kawrakow, I. (2008b). Efficiency improvements for ion chamber calculations in high energy photon beams. *Medical Physics*, *35*(4), 1328–1336. https://doi.org/10.1118/1.2874554

Zavgorodni, S., Bush, K., Locke, C., & Beckham, W. (2008). Vancouver Island Monte Carlo (VIMC) system for accurate radiotherapy dose calculations. In *Proceedings of 16th International Conference on Med. Phys., April 13* (Vol. 16, p. 78).

Zavgorodni, S., Bushz, K., Locke, C., & Beckham, W. (2007). Vancouver Island Monte Carlo (VIMC) system for radiotherapy treatment planning dosimetry and research. In *RADIOTHERAPY AND ONCOLOGY* (Vol. 84, pp. S49–S49). ELSEVIER IRELAND LTD ELSEVIER HOUSE, BROOKVALE PLAZA, EAST PARK SHANNON, CO, CLARE, 00000, IRELAND.

Zavgorodni, S., Locke, C., Bush, K., & Beckham, W. (2005). Correcting the BEAMNRC Phase-space to Match Monte Carlo and Measured Dose Distributions. *Australasian Physical & Engineering Sciences in Medicine*, *28*(4), 285.

Zavgorodni, Sergei. (2013). Monte Carlo investigation into feasibility and dosimetry of flat flattening filter free beams. *Physics in Medicine and Biology*, *58*(21), 7699.

Zavgorodni, Sergei, Alhakeem, E., & Townson, R. (2014). Monitor backscatter factors for the Varian 21EX and TrueBeam linear accelerators: measurements and Monte Carlo modelling. *Physics in Medicine and Biology*, *59*(4), 911–924. https://doi.org/10.1088/0031-9155/59/4/911